
Patched-Grid Calculations with the Euler and Navier-Stokes Equations: Theory and Application

M.M. Rai

February 1986

LIBRARY COPY

MAR 4 1986

LANGLEY RESEARCH CENTER
LIBRARY, NASA
HAMPTON, VIRGINIA



National Aeronautics and
Space Administration



NF00942

Patched-Grid Calculations with the Euler and Navier-Stokes Equations: Theory and Application

M. M. Rai, Informatics General Corp., Palo Alto, California

February 1986



National Aeronautics and
Space Administration

Ames Research Center
Moffett Field, California 94035

N86-28062#

PATCHED-GRID CALCULATIONS WITH THE EULER AND NAVIER-STOKES

EQUATIONS: THEORY AND APPLICATION

Man Mohan Rai*

NASA Ames Research Center, Moffett Field, California, U.S.A.

INTRODUCTION

A major problem in computational fluid dynamics is the generation of grids for realistic three-dimensional bodies such as complete aircraft configurations. The generation of a single grid that discretizes the entire flow region associated with a complex configuration is extremely difficult and, for some problems, it is impractical. Often, an attempt to generate a single grid for a complicated flow region results in highly skewed grids which, in turn, result in inaccurate calculations; also, such an attempt usually requires an inordinate amount of the aerodynamicist's time to "tune" existing grid generation schemes to yield acceptable grids. A second factor that contributes to the complexity of grid generation is the necessity to cluster grid points in regions where the dependent variables and their gradients change rapidly (selective grid refinement).

The problems mentioned above can be overcome, to a limited extent, by developing very sophisticated grid generation schemes. However, an alternative approach is to divide the given region into simpler subregions such that each subregion (or zone) is a geometrically simple figure, e.g., every two-dimensional region can be divided into simple four-sided zones, and every three-dimensional region into six-sided zones. Grids can then be independently generated for each zone using existing grid-generation schemes. The "zonal" approach has the following advantages:

1. The grid for any arbitrary region can be generated in a simple, straightforward manner (since the zones are geometrically simple).
2. Flow regions requiring grid refinement can be isolated in separate zones, and the required number of grid points can be introduced in these zones (if necessary, this can be done adaptively as the solution progresses in time).
3. The zonal approach facilitates the use of different equation sets in different zones; hence, simpler equation sets can be used in certain regions of the flow. This may result in a saving of computer time.
4. The zonal approach also facilitates a block-processing scheme wherein only the data corresponding to certain regions of the flow field are required to reside in the main memory of the computer; the remaining data can be stored on disc or tape. Theoretically, the block processing technique permits the use of unlimited global grid sizes (computing speeds become a limiting factor in this case).

*Informatics General Corp.

The subregions that result from the zoning process may be patched together (patched-grids) as in figure 1(a) or overlap one another (overlaid grids) as in figure 1(b). Both approaches have their relative advantages and disadvantages. Some disadvantages of overlaid grids are: a) A problem in n spatial dimensions requires interpolation in n dimensions (in order to transfer information from one grid onto another) while patched grids require only an $(n - 1)$ dimensional interpolation (the details are given in a later section). b) Maintaining global conservation seems to be more difficult with overlaid grids. c) The accuracy and convergence speed of the calculation seems to depend on the degree of overlap of the zones and the relative size of each zone, thus introducing a certain amount of undesirable empiricism in the formulation. However, the fact that zones can (and should) overlap, may result in a certain amount of flexibility in generating grids in three dimensions. A second advantage of overlaid grids may lie in the ease with which grids can be moved relative to each other (for calculations involving bodies that move relative to each other). This set of lecture notes will deal primarily with patched-grids.

The following examples serve to illustrate some of the advantages of the patched-grid approach. Figure 2 shows the flow region associated with a combination of three airfoils. The region is multiply connected and hence difficult to discretize with a single grid system. The division of the flow field into thirteen patches as in figure 2 results in simple four-sided regions which can be discretized easily. Figure 3(a) shows a six-finned projectile and figure 3(b) the grid used to discretize the flow region at the aft end of the projectile (ref. 1). Immediately after this axial station, an entirely new type of grid (fig. 3(c)) is required because of the sudden termination of the body. This transition can be achieved by treating the plane corresponding to the aft end of the projectile as a two-dimensional (surface) patch-boundary separating two three-dimensional patches. It should be noted that the grid in figure 3(c) is itself composed of four two-dimensional grids separated by one-dimensional (line) patch-boundaries. The grids in figure 3(c) alleviate the geometric singularity problem associated with a simple polar grid, and also facilitate the addition of grid points to the central portion of the flow region (to accurately model the wake).

The division of a given region into patches introduces new boundaries in the calculation: the patch boundaries. Since the grid for each region is generated independently, the grid lines of two adjoining regions may align (continuous grids) or may not align (discontinuous grids) with each other. Even in the case of continuous grids, a sudden change in grid spacing or grid line orientation across the zonal boundary may give rise to discontinuities in the transformation metrics (metric-discontinuous grids). Figure 4 shows the different types of grids mentioned above.

In order that information be transferred from one patch to another accurately, it is important to treat grid points on the patch boundaries with care. The nonlinear nature of the Euler and Navier-Stokes equations permits solutions with discontinuities, such as shocks. It is imperative that the finite-difference scheme used for the calculation be conservative so that these discontinuities, when captured,

assume the right strength and physical location. In a patched-grid calculation, it is important that the patch boundaries are also treated in a conservative manner so that the discontinuities can move freely across these boundaries. Results demonstrating the importance of maintaining conservation at patch boundaries can be found in references 2 and 3.

Earlier work in the area of patched-grid calculations includes that of Cambier et al. (ref. 4). The authors analyze the patch-boundary problem for a system of hyperbolic equations and use the compatibility equations to develop a patch-boundary scheme. They present encouraging results for transonic channel flow. The use of the compatibility equations at the patch-boundary, however, results in a patch-boundary scheme that is not conservative; and hence, such a procedure is unsuitable for problems in which flow discontinuities move from one patch to another. Hennesius and Pulliam (ref. 2) present a conservative patch-boundary scheme for implicit integration methods like the Beam-Warming method (ref. 5). Their results stress the need for a conservative patch-boundary scheme. However, the authors do not address the problem of discontinuous metrics or discontinuous grids across patch-boundaries. Rai, Chakravarthy and Hennesius (ref. 3) present results obtained on metric-discontinuous grids. The integration scheme used is the Osher upwind scheme. The proper choice of transformation metrics in the calculation of the fluxes makes the scheme fully conservative at both interior and patch-boundary points.

A fully conservative patch-boundary scheme, that permits the movement of discontinuities across patch boundaries with minimal distortion of the solution, is developed in reference 6. The scheme is designed for both discontinuous and metric-discontinuous grids and can be used in conjunction with first-order accurate, explicit integration schemes. The scheme is stable, accurate and is formulated in generalized coordinates. Results demonstrating these characteristics of the scheme are also presented in reference 6. The demonstration calculations include supersonic flow over a cylinder, blast wave diffraction by a ramp and the one-dimensional shock tube problem solved on a two-dimensional grid.

The patched-grid scheme as developed in reference 6 can be used with first-order accurate, explicit integration schemes. However, first-order accurate integration schemes are insufficient to produce accurate results for a general class of problems. In reference 7 the patched-grid scheme of reference 6 is extended so that it can be used in conjunction with second-order accurate, implicit, integration schemes such as the Beam-Warming scheme (ref. 5) and an implicit form of the Osher scheme (ref. 8). Both these integration schemes use approximate factorization to retain the block tridiagonal nature of the implicit equations in two and three spatial dimensions. The implicit patch-boundary condition, however, is developed so that it can be used with both factored and unfactored schemes. In reference 9, the explicit patched-grid scheme is extended to work with the implicit relaxation schemes of reference 10. Reference 11 presents two new conservative, patch-boundary schemes for finite-volume methods and demonstrates linear stability of these schemes. In reference 12 the schemes developed in reference 11 are applied in two and three dimensions to provide local grid refinement for airfoil and wing

computations. Reference 13 presents a finite-volume, patched-grid scheme for the Euler equations and some local grid refinement studies. Reference 14 also presents grid refinement studies with patched and overlaid meshes using the CSCM method (ref. 15).

Reference 16 presents a conservative zonal boundary condition for problems in one spatial dimension. The primary emphasis of this study is the refinement of the mesh in regions of large solution error. In addition to refinement of the grid in space, the problem of using different time steps in different regions is addressed. A general procedure to derive consistent, conservative, patched, and overlaid boundary conditions is developed in reference 17.

While the multiple-grid publications referenced above present schemes and results for the Euler and Navier-stokes equations, related work has also been done using the transonic full potential equation. Typical of this effort is the work of Atta (ref. 18) and Atta and Vadyak (ref. 19). The overlaid-grid approach is used in references 18 and 19. Reference 20 gives results obtained on overlaid grids in conjunction with the stream function approach. References 21 and 22 give patched grid results for the potential and full potential equations; the problem of conservation of fluxes is not addressed.

In this set of lecture notes, the patch-boundary scheme of references 6, 7, and 9 are described in detail. The integration methods used to update the interior grid points are also discussed. A brief mention is made of the work on stability of patch-boundary schemes and the use of these schemes in Navier-Stokes calculations. Results are presented for inviscid, supersonic flow over a cylinder, blast wave diffraction by ramp, and the motion of a vortex in a freestream. These test cases demonstrate the quality of solutions possible with the patch-boundary scheme under study.

One of the most important applications of the patched-grid approach is the treatment of flow regions associated with bodies which have some parts moving relative to others, e.g., the helicopter rotor-fuselage combination, or the rotor-stator configurations found in turbines and compressors. It is impractical to have a single grid that envelops both the moving and stationary parts of the system. This problem can be overcome simply by containing the stationary parts in one patch (or set of patches) and the moving parts in another patch (or set of patches). The patches that contain the moving parts can be made to be stationary relative to the moving parts. This approach gives rise to patch boundaries (where the moving and stationary patches meet) at which one set of grid points move relative to others. The patch-boundary treatment in this case has to be time accurate (in addition to the usual requirement of spatial accuracy) in order to yield reasonable results. The time accuracy that is possible in such patched-grid calculations is demonstrated in reference 7. The test calculation of this reference has been included in this set of notes to demonstrate the feasibility of performing calculations on patches that move relative to each other. An application of this technology is also presented. The application consists of two parabolic-arc airfoils that move relative to each other much like the blades in a rotor-stator combination. Results in the form of surface pressure histories and time varying pressure contours are included.

As a final demonstration of the applicability of the moving-patch technique to realistic rotor-stator problems, it has been used to simulate the flow in a rotor-stator configuration of an axial turbine (ref. 23). The numerically obtained results are compared with experimental data. A good agreement is obtained for both time-averaged surface pressure data and surface pressure amplitudes.

INTEGRATION SCHEMES

The patch-boundary scheme is developed for explicit first-order accurate integration schemes and for implicit, relaxation schemes that are both first- and second-order accurate in a later section. In this section, the explicit and implicit versions of the Osher scheme (refs. 8, 10, and 24) are presented. Although the flux-linearizations that are required for the implicit technique are developed with the Osher scheme in mind, they can be used equally effectively with the split-flux scheme and Roe's scheme (ref. 25). The implicit scheme that is presented is iterative in nature, but reverts to a conventional noniterative implicit scheme when the number of iterations is restricted to one. The iterative procedure considerably simplifies the extension of explicit patch-boundary schemes to implicit patch-boundary schemes (details of which are given in the next section).

Consider the unsteady Euler equations in two dimensions

$$Q_t + E_x + F_y = 0 \quad (1)$$

where the vectors Q , E , and F are given by

$$Q = \begin{pmatrix} \rho \\ \rho u \\ \rho v \\ e \end{pmatrix} \quad E = \begin{pmatrix} \rho u \\ p + \rho u^2 \\ \rho uv \\ (e + p)u \end{pmatrix} \quad F = \begin{pmatrix} \rho v \\ \rho uv \\ p + \rho v^2 \\ (e + p)v \end{pmatrix} \quad (2)$$

where ρ is the density, p is the pressure, u and v are the velocities in the x and y directions respectively, and e is the total energy per unit volume

$$e = \frac{p}{(\gamma - 1)} + \frac{\rho}{2} (u^2 + v^2) \quad (3)$$

Establishing the independent variable transformation

$$\begin{aligned} \tau &= t \\ \xi &= \xi(x, y, t) \\ \eta &= \eta(x, y, t) \end{aligned} \quad (4)$$

and applying this transformation to equation (1), the following is obtained

$$\tilde{Q}_\tau + \tilde{E}_\xi + \tilde{F}_\eta = 0 \quad (5)$$

where

$$\left. \begin{aligned} \tilde{Q} &= Q/J \\ \tilde{E}(Q, \xi) &= (\xi_t Q + \xi_x E + \xi_y F)/J \\ \tilde{F}(Q, \eta) &= (\eta_t Q + \eta_x E + \eta_y F)/J \\ J &= \xi_x \eta_y - \eta_x \xi_y \end{aligned} \right\} \quad (6)$$

The notation $\tilde{E}(Q, \xi)$ and $\tilde{F}(Q, \eta)$ is used to show the dependence of these quantities on the metrics of the transformation.

A conservative finite-difference scheme for equation (5) is given by

$$\frac{\Delta \tilde{Q}_{j,k}^n}{\Delta \tau} + \frac{\hat{E}_{j+1/2,k}^m - \hat{E}_{j-1/2,k}^m}{\Delta \xi} + \frac{\hat{F}_{j,k+1/2}^m - \hat{F}_{j,k-1/2}^m}{\Delta \eta} = 0 \quad (7)$$

where $\hat{E}_{j+1/2,k}$ and $\hat{F}_{j,k+1/2}$ are numerical fluxes consistent with the transformed physical fluxes \tilde{E} and \tilde{F} . The difference scheme (eq. (7)) is explicit when $m = n$ and fully implicit when $m = n + 1$.

The First-Order Accurate Osher Scheme

The numerical flux for the first-order Osher scheme is given by (ref. 24)

$$\begin{aligned} \hat{E}_{j+1/2,k} &= \frac{1}{2} [\tilde{E}(Q_{j,k}, \xi_{j+1/2,k}) + E(Q_{j+1,k}, \xi_{j+1/2,k}) \\ &\quad - \Delta E^+(Q_{j,k}, Q_{j+1,k}, \xi_{j+1/2,k}) + \Delta E^-(Q_{j,k}, Q_{j+1,k}, \xi_{j+1/2,k})] \end{aligned} \quad (8)$$

where

$$\Delta E^\pm(Q_{j,k}, Q_{j+1,k}, \xi_{j+1/2,k}) = \int_{Q_{j,k}}^{Q_{j+1,k}} \left[\frac{\partial \tilde{E}}{\partial Q}(Q, \xi_{j+1/2,k}) \right]^\pm dQ \quad (9)$$

The numerical flux $\hat{F}_{j,k+1/2}$ can be obtained in a similar manner. The evaluation of the line integral can be found in reference 24.

An evaluation of the numerical flux in equation (8) using the dependent variables at the n th level results in an explicit scheme and difference equations that are linear. However, an evaluation of these fluxes at the $(n+1)$ th time level results in an implicit scheme and difference equations that are nonlinear and need to be solved in an iterative manner. The usual strategy that is employed at this stage is the linearization of the numerical fluxes with respect to the time like variable τ . The resulting system of linear equations is then solved in order to update the dependent variables. The linearization process depends on the scheme used to determine the numerical fluxes. The linearization of the Osher fluxes is discussed below.

The time linearization of the numerical flux $\hat{E}_{j+1/2,k}^{n+1}$ requires the linearization of the integral given in equation (9). The linearization of this integral is a cumbersome process that is computationally expensive. Hence, the following approximation (ref. 8) is made to simplify the linearization process:

$$\left[\frac{\partial \tilde{E}}{\partial Q} (Q, \xi_{j+1/2,k}) \right]^{\pm} = \frac{\partial}{\partial Q} [\tilde{E}^{\pm}(Q, \xi_{j+1/2,k})] \quad (10)$$

where

$$\tilde{E}^{\pm}(Q, \xi_{j+1/2,k}) = \left[\frac{\partial \tilde{E}}{\partial Q} (Q, \xi_{j+1/2,k}) \right]^{\pm} Q \quad (11)$$

Substituting equation (10) into equation (9) yields

$$[\Delta E^{\pm}(Q_{j,k}, Q_{j+1,k}, \xi_{j+1/2,k})]^{n+1} = (\tilde{E}_{j+1,k}^{\pm} - \tilde{E}_{j,k}^{\pm})^{n+1} \quad (12)$$

Equations (8) and (12) together yield

$$(\hat{E}_{j+1/2,k}^{n+1})_{\text{approx}} = [\tilde{E}^{+}(Q_{j,k}, \xi_{j+1/2,k}) + \tilde{E}^{-}(Q_{j+1,k}, \xi_{j+1/2,k})]^{n+1} \quad (13)$$

Linearizing equation (13) with respect to τ and making use of equation (10) once again, it can be shown that

$$(\hat{E}_{j+1/2,k}^{n+1})_{\text{approx}} = (\hat{E}_{j+1/2,k}^n)_{\text{approx}} + (\tilde{A}_{j,k}^{+})^n \Delta \tilde{Q}_{j,k} + (\tilde{A}_{j+1,k}^{-})^n \Delta \tilde{Q}_{j+1,k} \quad (14)$$

where

$$\tilde{A}_{j,k}^{\pm} = \left[\frac{\partial \tilde{E}}{\partial \tilde{Q}} (Q_{j,k}, \xi_{j+1/2,k}) \right]^{\pm} \quad (15)$$

The numerical flux for the first-order accurate Osher scheme using this approximate linearization can now be written as

$$\begin{aligned} (\hat{E}_{j+1/2,k}^{n+1})_{\text{linearized}} &= \hat{E}_{j+1/2,k}^n + [\tilde{A}^+(Q_{j,k}, \xi_{j+1/2,k}) \Delta \tilde{Q}_{j,k} \\ &\quad + \tilde{A}^-(Q_{j+1,k}, \xi_{j+1/2,k}) \Delta \tilde{Q}_{j+1,k}]^n \end{aligned} \quad (16)$$

where $\hat{E}_{j+1/2,k}^n$ is evaluated using equation (8). It should be noted that the use of the approximate linearization does not result in any loss of the conservative properties of the scheme.

The iterative implicit technique of reference 8 as applied to the first-order accurate Osher scheme now takes the form

$$\begin{aligned} &\left[I + \frac{\Delta \tau}{\Delta \xi} (\nabla_{\xi} \tilde{A}_{j,k}^+ + \Delta_{\xi} \tilde{A}_{j,k}^-) + \frac{\Delta \tau}{\Delta \eta} (\nabla_{\eta} \tilde{B}_{j,k}^+ + \Delta_{\eta} \tilde{B}_{j,k}^-) \right]^p (\tilde{Q}_{j,k}^{p+1} - \tilde{Q}_{j,k}^p) \\ &= -\Delta \tau \left(\frac{\tilde{Q}_{j,k}^p - \tilde{Q}_{j,k}^n}{\Delta \tau} + \frac{\hat{E}_{j+1/2,k}^p - \hat{E}_{j-1/2,k}^p}{\Delta \xi} + \frac{\hat{F}_{j,k+1/2}^p - \hat{F}_{j,k-1/2}^p}{\Delta \eta} \right) \end{aligned} \quad (17)$$

where \tilde{Q}^p is an approximation to \tilde{Q}^{n+1} . When $p = 0$, $\tilde{Q}^p = \tilde{Q}^n$ and when equation (17) is iterated to convergence at a given time-step, $\tilde{Q}^p = \tilde{Q}^{n+1}$. It should be noted that, because the left-hand side of this equation can be made equal to zero at each time step (by iterating to convergence), linearization errors can be driven to zero during the iterative process. For problems where only the asymptotic steady-state is of interest, the iteration process need not be carried to convergence at each time-step. In fact, when the number of iterations is restricted to one, the scheme reverts to a conventional noniterative scheme of the type in reference 5 (but unfactored).

Unfortunately, equation (17) is extremely time consuming to solve in a direct fashion because of the large bandwidth of the matrix on the left-hand side. At this point, two options are available to the user; the first option is to use approximate factorization as in references 5 and 8, the second option is to use a relaxation strategy as in references 9 and 10. The approximately factored form of equation (17) is given below

$$\left[I + \frac{\Delta\tau}{\Delta\xi} (\nabla_{\xi} \tilde{A}_{j,k}^{+} + \Delta_{\xi} \tilde{A}_{j,k}^{-}) \right]^p \left[I + \frac{\Delta\tau}{\Delta\eta} (\nabla_{\eta} \tilde{B}_{j,k}^{+} + \Delta_{\eta} \tilde{B}_{j,k}^{-}) \right]^p (\tilde{Q}_{j,k}^{p+1} - \tilde{Q}_{j,k}^p) \\ = \text{RHS of equation (17)} \quad (18)$$

Clearly, approximate factorization reduces the bandwidth (the single large bandwidth matrix is converted into two block-tridiagonal matrices). If the iteration process is carried to convergence, the factorization error is driven to zero. However, at very large time steps, factorization error may cause the iteration process to diverge or enter a limit cycle.

Relaxation schemes on the other hand do not require factorization and hence, typically, permit the use of much larger time steps. The iterative form of equation (17) is ideally suited to relaxation schemes. Although there are a host of different relaxation schemes available, the ones that have been chosen for this study are schemes that are most amenable to vectorization; in particular, pointwise and line relaxation schemes of the non-Gauss-Seidel type. The pointwise relaxation scheme is obtained by discarding all the nondiagonal terms on the left-hand side of equation (17). This yields

$$\left[I + \frac{\Delta\tau}{\Delta\xi} (\tilde{A}_{j,k}^{+} - \tilde{A}_{j,k}^{-}) + \frac{\Delta\tau}{\Delta\eta} (\tilde{B}_{j,k}^{+} - \tilde{B}_{j,k}^{-}) \right]^p (\tilde{Q}_{j,k}^{p+1} - \tilde{Q}_{j,k}^p) = \text{RHS of equation (17)} \\ (19)$$

The line relaxation scheme is obtained by retaining all the diagonal terms and terms corresponding to points on a given line, for example, a constant η line. This yields

$$\left[I + \frac{\Delta\tau}{\Delta\xi} (\nabla_{\xi} \tilde{A}_{j,k}^{+} + \Delta_{\xi} \tilde{A}_{j,k}^{-}) + \frac{\Delta\tau}{\Delta\eta} (\tilde{B}_{j,k}^{+} - \tilde{B}_{j,k}^{-}) \right]^p (\tilde{Q}_{j,k}^{p+1} - \tilde{Q}_{j,k}^p) \\ = \text{RHS of equation (17)} \quad (20)$$

If the constant ξ lines had been chosen instead, the resulting equations would be

$$\left[I + \frac{\Delta\tau}{\Delta\xi} (\tilde{A}_{j,k}^{+} - \tilde{A}_{j,k}^{-}) + \frac{\Delta\tau}{\Delta\eta} (\nabla_{\eta} \tilde{B}_{j,k}^{+} + \Delta_{\eta} \tilde{B}_{j,k}^{-}) \right]^p (\tilde{Q}_{j,k}^{p+1} - \tilde{Q}_{j,k}^p) \\ = \text{RHS of equation (17)} \quad (21)$$

Variants of the line and pointwise relaxation schemes (such as the zebra and check-board schemes) are also discussed in reference 10.

Although equation (17) is fully conservative (in spite of the approximate linearization), equations (19)-(21) are not conservative in time unless they are iterated to convergence at each time step (this would be necessary for time dependent problems where the transients are of interest). However, for problems where only the time asymptotic solutions are required, equations (18)-(20) yield solutions that satisfy the conservation laws at steady-state without requiring iteration to convergence at each time step. This is because the right-hand side of these equations is fully conservative.

The Second-Order-Accurate Osher Scheme

The numerical flux for the second-order accurate Osher scheme is given by (ref. 24)

$$\begin{aligned} \bar{E}_{j+1/2,k} = & \hat{E}_{j+1/2,k} \text{ (first order Osher scheme)} \\ & + [\Delta E^+(Q_{j-1,k}, Q_{j,k}, \xi_{j+1/2,k}) - \Delta E^-(Q_{j+1,k}, Q_{j+2,k}, \xi_{j+1/2,k})] \end{aligned} \quad (22)$$

where ΔE^\pm are evaluated as before. Note that the numerical flux for the second-order scheme is denoted by $\bar{E}_{j+1/2,k}$ to distinguish it from the numerical flux for the first-order Osher scheme. Linearization of all the terms in equation (22) would result in block-pentadiagonal matrices for line-relaxation schemes. Hence, only the terms corresponding to the first-order scheme and those second-order terms that contribute to the diagonal elements of the matrix are linearized (private communication, S. R. Chakravarthy, Rockwell International Science Center). The resulting iterative, implicit scheme takes the form

$$\begin{aligned}
& \left\{ I + \frac{\Delta\tau}{\Delta\xi} \left[\frac{1}{2} (\tilde{A}_{j,k}^+ - \tilde{A}_{j,k}^-) + \nabla_{\xi} \tilde{A}_{j,k}^+ + \Delta_{\xi} \tilde{A}_{j,k}^- \right] + \frac{\Delta\tau}{\Delta\eta} \left[\frac{1}{2} (\tilde{B}_{j,k}^+ - \tilde{B}_{j,k}^-) + \nabla_{\eta} \tilde{B}_{j,k}^+ \right. \right. \\
& \left. \left. + \Delta_{\eta} \tilde{B}_{j,k}^- \right] \right\}^p (\tilde{Q}_{j,k}^{p+1} - \tilde{Q}_{j,k}^p) = -\Delta\tau \left(\frac{\tilde{Q}_{j,k}^p - \tilde{Q}_{j,k}^n}{\Delta\tau} + \frac{\hat{E}_{j+1/2,k}^p - \hat{E}_{j-1/2,k}^p}{\Delta\xi} \right. \\
& \left. + \frac{\hat{F}_{j,k+1/2}^p - \hat{F}_{j,k-1/2}^p}{\Delta\eta} \right) \\
& - \frac{\Delta\tau}{2\Delta\xi} [\overline{\Delta E^+}(Q_{j-1,k}, Q_{j,k}, \xi_{j+1/2,k}) - \overline{\Delta E^+}(Q_{j-2,k}, Q_{j-1,k}, \xi_{j-1/2,k})]^p \\
& + \frac{\Delta\tau}{2\Delta\xi} [\overline{\Delta E^-}(Q_{j+1,k}, Q_{j+2,k}, \xi_{j+1/2,k}) - \overline{\Delta E^-}(Q_{j,k}, Q_{j+1,k}, \xi_{j-1/2,k})]^p \\
& - \frac{\Delta\tau}{2\Delta\eta} [\overline{\Delta F^+}(Q_{j,k-1}, Q_{j,k}, \eta_{j,k+1/2}) - \overline{\Delta F^+}(Q_{j,k-2}, Q_{j,k-1}, \eta_{j,k-1/2})]^p \\
& + \frac{\Delta\tau}{2\Delta\eta} [\overline{\Delta F^-}(Q_{j,k+1}, Q_{j,k+2}, \eta_{j,k+1/2}) - \overline{\Delta F^-}(Q_{j,k}, Q_{j,k+1}, \eta_{j,k-1/2})]^p \quad (23)
\end{aligned}$$

The terms that result in second-order spatial accuracy (on the right-hand side of eq. (23)) have been modified, that is, these flux differences are obtained from a flux-limiting process. Details of flux-limiting for the Osher scheme can be found in reference 24. Flux-limiting is essential to provide the diagonal dominance required for relaxation schemes (ref. 10).

The pointwise relaxation scheme is now obtained by discarding all nondiagonal terms, that is,

$$\begin{aligned}
& \left[I + \frac{3\Delta\tau}{2\Delta\xi} (\tilde{A}_{j,k}^+ - \tilde{A}_{j,k}^-) + \frac{3\Delta\tau}{2\Delta\eta} (\tilde{B}_{j,k}^+ - \tilde{B}_{j,k}^-) \right]^p (\tilde{Q}_{j,k}^{p+1} - \tilde{Q}_{j,k}^p) \\
& = \text{RHS of equation (23)} \quad (24)
\end{aligned}$$

and the line relaxation scheme corresponding to equation (20) takes the form

$$\begin{aligned}
& \left\{ I + \frac{\Delta\tau}{\Delta\xi} \left[\frac{1}{2} (\tilde{A}_{j,k}^+ - \tilde{A}_{j,k}^-) + \nabla_{\xi} \tilde{A}_{j,k}^+ + \Delta_{\xi} \tilde{A}_{j,k}^- \right] + \frac{3\Delta\tau}{2\Delta\eta} (\tilde{B}_{j,k}^+ - \tilde{B}_{j,k}^-) \right\}^p (\tilde{Q}_{j,k}^{p+1} - \tilde{Q}_{j,k}^p) \\
& = \text{RHS of equation (23)} \quad (25)
\end{aligned}$$

The comments regarding the conservative properties of the first-order schemes apply to the second-order schemes as well. As stated earlier, although equations (17)-(25) have been developed for the Osher scheme, they are equally

applicable to the split-flux scheme and Roe's scheme; only the evaluation of the fluxes on the right hand side of these equations changes according to the particular integration scheme chosen.

THE PATCH BOUNDARY SCHEME

In order that information is transferred accurately and easily from patch to patch, a patch-boundary condition must satisfy several requirements. Some of these are listed below. The patch-boundary condition must be:

1. Numerically stable
2. Spatially and temporally accurate
3. Conservative so that flow discontinuities can move from one grid to another without any distortion
4. Easily applicable in generalized coordinates.

A patch-boundary condition that satisfies these requirements and that can be used with explicit and implicit schemes is presented in this section.

The Explicit Patch-Boundary Scheme

In order to develop the explicit patch-boundary condition, we consider the unsteady Euler equations in two spatial dimensions (eq. (1)). Equation (7) presents a conservative-difference scheme for the unsteady Euler equations. For the simple transformation of coordinates $\xi = x$, $\eta = y$, and $\tau = t$, this set of equations (eq. (7)) can be written as

$$\frac{\Delta Q_{j,k}}{\Delta t} + \frac{\hat{E}_{j+1/2,k} - \hat{E}_{j-1/2,k}}{\Delta x} + \frac{\hat{F}_{j,k+1/2} - \hat{F}_{j,k-1/2}}{\Delta y} = 0 \quad (26)$$

where \hat{E} and \hat{F} are evaluated at the n th time step. Equation (26) can be alternatively written as

$$\frac{\Delta x \Delta y}{\Delta t} (Q_{j,k}^{n+1} - Q_{j,k}^n) + \Delta y (\hat{E}_{j+1/2,k} - \hat{E}_{j-1/2,k}) + \Delta x (\hat{F}_{j,k+1/2} - \hat{F}_{j,k-1/2}) = 0 \quad (27)$$

In this form the various terms in the equation can be easily interpreted; for example, the first term

$$\frac{\Delta x \Delta y}{\Delta t} (Q_{j,k}^{n+1} - Q_{j,k}^n)$$

represents the rate of increase of the variable $Q_{j,k}$ in the cell ABCD (fig. 5). The term

$$-\Delta y (\hat{E}_{j+1/2,k} - \hat{E}_{j-1/2,k})$$

represents the net influx of mass, momentum, and energy into the cell through the sides AB and CD, and the term

$$-\Delta x (\hat{F}_{j,k+1/2} - \hat{F}_{j,k-1/2})$$

represents the net influx of the same quantities through the sides AC and BD.

A summation of the term

$$\frac{\Delta x \Delta y}{\Delta t} (Q_{j,k}^{n+1} - Q_{j,k}^n)$$

over all the grid points yields (using eq. (27))

$$\begin{aligned} S &= \sum_{j=1}^{j_{\max}} \sum_{k=1}^{k_{\max}} \frac{\Delta x \Delta y}{\Delta t} (Q_{j,k}^{n+1} - Q_{j,k}^n) \\ &= \Delta x \sum_{j=1}^{j_{\max}} (\hat{F}_{j,1/2} - \hat{F}_{j,k_{\max}+1/2}) + \Delta y \sum_{k=1}^{k_{\max}} (\hat{E}_{1/2,k} - \hat{E}_{j_{\max}+1/2,k}) \end{aligned} \quad (28)$$

that is, S is only a sum of the boundary fluxes; the interior fluxes cancel each other out because the difference scheme (eq. (26)) is conservative. Equation (28) represents the global conservation property of any scheme that can be represented as in equation (26).

Consider the grid shown in figure 6. The line AB represents the patch boundary that separates the two grids that are used to discretize the given region. Let ℓ and m be the indices used in the x and y directions, respectively, in patch 1 and let j and k be the corresponding indices for patch 2. Let n represent the time step for both patches. A superscript within parentheses will denote the patch to

which a given quantity belongs, e.g., $\Delta x^{(1)}$ denotes the mesh spacing in the x direction in patch 1.

One condition that must be satisfied across the patch boundary is the continuity of the dependent variables. This condition can be easily satisfied by integrating the equations of motion to update Q on one side of the patch boundary and interpolating these variables to obtain the updated variables on the other side of the patch boundary. This interpolation results in the dependent variables being continuous (across the patch boundary) to the order of accuracy of the interpolation scheme. A linear interpolation scheme was used to obtain the results presented in this set of notes.

Assume that the patch-boundary points of patch 2 are to be updated using the finite-difference scheme of equation (26). This calculation requires the fluxes $\hat{F}_{j,1/2}^{(2)}$. The question of how to calculate these fluxes introduces the second condition that is to be satisfied at the patch boundary in a natural way; that is, these fluxes have to be calculated such that global conservation is maintained. In other words, a summation of $(\Delta x^{(1)} \Delta y^{(1)} / \Delta t) \Delta Q_{\ell,m}^{(1)}$ and $(\Delta x^{(2)} \Delta y^{(2)} / \Delta t) \Delta Q_{j,k}^{(2)}$ over all the cells in the region of interest (as was done in eq. (28)) should once again result in only the boundary fluxes. The sum should not contain any residual fluxes near the patch boundary. Note that cells corresponding to the patch-boundary points of patch 1 are not to be included in this summation. This is because the area that these cells represent has already been accounted for with the inclusion of the cells corresponding to the patch-boundary points of patch 2 (a sum of the cell areas included in the above summation should result in the total area covered by the two patches). A typical cell (RSTU) of a patch boundary point $(j,1)$ is shown in figure 6. The points R and S are midpoints of the cells they lie in while the points T and U are obtained as follows: The constant j lines of patch 2 are extrapolated into patch 1 to intersect the line CD (CD corresponds to $m = m_{\max} - 1/2$ in patch 1 and to $k = 1/2$ in patch 2). The intersection points have the indices $(j,1/2)$. Point T is midway between the points $(j+1,1/2)$ and $(j,1/2)$ while point U is midway between points $(j,1/2)$ and $(j-1,1/2)$.

The global conservation property can be shown to be satisfied if the following relationship is satisfied

$$\begin{aligned}
 & \frac{\Delta x^{(2)}}{2} (\hat{F}_{1,1/2}^{(2)} + \hat{F}_{j_{\max},1/2}^{(2)}) + \Delta x^{(2)} \sum_{j=2}^{j_{\max}-1} \hat{F}_{j,1/2}^{(2)} \\
 & = \frac{\Delta x^{(1)}}{2} (\hat{F}_{1,m_{\max}-1/2}^{(1)} + \hat{F}_{\ell_{\max},m_{\max}-1/2}^{(1)}) + \Delta x^{(1)} \sum_{\ell=2}^{\ell_{\max}-1} \hat{F}_{\ell,m_{\max}-1/2}^{(1)} \quad (29)
 \end{aligned}$$

A close examination of equation (29) shows that each side of this equation is nothing but a discrete form of the line integral of the numerical flux \hat{F} along the line CD in figure 6 while the equation itself represents flux conservation across the patch boundary. Equation (29) is only a necessary condition and is not sufficient to define the fluxes $\hat{F}_{j,1/2}^{(2)}$ in a physically meaningful fashion (the $\hat{F}_{j,1/2}^{(2)}$ cannot be obtained from eq. (29) alone since eq. (29) does not uniquely specify the $\hat{F}_{j,1/2}^{(2)}$).

Assume that the $\hat{F}_{j,1/2}^{(2)}$ are obtained by interpolating the $\hat{F}_{\ell,mmax-1/2}^{(1)}$, i.e.,

$$\hat{F}_{j,1/2}^{(2)} = \sum_{\ell=p}^q N_{j,\ell} \hat{F}_{\ell,mmax-1/2}^{(1)} \quad (30)$$

where the $N_{j,\ell}$ are interpolation coefficients and p and q define the set of fluxes of patch 1 that will be used in the interpolation. We now describe a very simple way of obtaining the interpolation coefficients $N_{j,\ell}$ such that equation (29) is automatically satisfied. Let the line CD in figure 7 correspond to the line CD in figure 6. The dots represent the grid points of patch 1 and the crosses represent those of patch 2. Representative numerical values of $\hat{F}_{\ell,mmax-1/2}^{(1)}$ are plotted on the positive y axis. Assume a piece-wise constant variation of $\hat{F}_{\ell,mmax-1/2}^{(1)}$, that is, $\hat{F}_{\ell,mmax-1/2}^{(1)}$ is constant between $x_{\ell-1/2,mmax-1/2}^{(1)}$ and $x_{\ell+1/2,mmax-1/2}^{(1)}$. Consider a patch-boundary point of patch 2, $(j,1)$. Let E be midway between $(j-1,1/2)$ and $(j,1/2)$ and F be midway between $(j,1/2)$ and $(j+1,1/2)$. The $\hat{F}_{j,1/2}^{(2)}$ are now calculated from

$$\Delta x^{(2)} \hat{F}_{j,1/2}^{(2)} = \int_E^F \hat{F}_{\ell,mmax-1/2}^{(1)} dx$$

or

$$\begin{aligned} \hat{F}_{j,1/2}^{(2)} &= \frac{1}{\Delta x^{(2)}} \int_E^F \hat{F}_{\ell,mmax-1/2}^{(1)} dx \\ &= \sum_{\ell=p}^q N_{j,\ell} \hat{F}_{\ell,mmax-1/2}^{(1)} \end{aligned} \quad (31)$$

where the values of $N_{j,l}$ are given by

$$N_{j,l} = \begin{cases} 0 & \text{if } x_{l+1/2}^{(1)}, x_{l-1/2}^{(1)} \leq x_{j-1/2}^{(2)} \\ 0 & \text{if } x_{l+1/2}^{(1)}, x_{l-1/2}^{(1)} \geq x_{j+1/2}^{(2)} \\ (x_r - x_l) / (x_{j+1/2}^{(2)} - x_{j-1/2}^{(2)}) & \text{otherwise} \end{cases} \quad (32)$$

and

$$x_r = \min(x_{j+1/2}^{(2)}, x_{l+1/2}^{(1)})$$

$$x_l = \max(x_{j-1/2}^{(2)}, x_{l-1/2}^{(1)})$$

The simple expressions for $N_{j,l}$ given in equation (32) are valid only for a piecewise constant variation of the numerical fluxes. A piecewise linear or any other variation would result in different formulae for the $N_{j,l}$. Equation (32), in an indirect manner, also yields the end points in the interpolation, p and q (p and q only include that set of fluxes of patch 1 that are multiplied by nonzero interpolation coefficients for a given flux of patch 2). The end fluxes $\hat{F}_{1,1/2}^{(2)}$ and $\hat{F}_{jmax,1/2}^{(2)}$ are calculated as

$$\begin{aligned} \hat{F}_{1,1/2}^{(2)} &= \frac{2}{\Delta x^{(2)}} \int_C^G \hat{F}_{l,mmax-1/2}^{(1)} dx \\ &= \sum_{l=1}^t N_{1,l} \hat{F}_{l,mmax-1/2}^{(1)} \end{aligned} \quad (33)$$

and

$$\begin{aligned} \hat{F}_{jmax,1/2}^{(2)} &= \frac{2}{\Delta x^{(2)}} \int_H^D \hat{F}_{l,mmax-1/2}^{(1)} dx \\ &= \sum_{l=u}^{lmax} N_{jmax,l} \hat{F}_{l,mmax-1/2}^{(1)} \end{aligned} \quad (34)$$

The fluxes thus obtained satisfy equation (29) automatically. The shaded areas in figure 7 represent the values of the integrals in equations (31), (33), and (34).

Summarizing, the explicit patched-grid scheme consists of the following three steps:

1. Integrate the dependent variables at grid points (of both of the grids) that do not belong to the patch boundary.
2. Integrate the dependent variables at the patch-boundary points of one of the patches (for instance, patch 2 of fig. 6) using a scheme that conserves fluxes across the patch boundary.
3. Obtain the dependent variables at the patch-boundary points of the other patch (for instance, patch 1 of fig. 6) such that the dependent variables are continuous along the patch boundary.

The foregoing discussion pertained to simple rectangular grids. The extension of the method to arbitrary curvilinear grid systems is straightforward and is outlined below. Consider the curvilinear grids used to discretize the region shown in figure 8. Establishing two independent variable transformations

$$\begin{aligned}\tau^{(i)} &= t \\ \xi^{(i)} &= \xi^{(i)}(x, y, t) \\ \eta^{(i)} &= \eta^{(i)}(x, y, t)\end{aligned}\tag{35}$$

and applying these transformations to equation (1) we obtain

$$\tilde{Q}_{\tau}^{(i)} + \tilde{E}_{\xi}^{(i)} + \tilde{F}_{\eta}^{(i)} = 0\tag{36}$$

where

$$\begin{aligned}\tilde{Q}^{(i)} &= Q/J^{(i)} \\ \tilde{E}^{(i)}(Q, \xi^{(i)}) &= (\xi_t^{(i)} Q + \xi_x^{(i)} E + \xi_y^{(i)} F)/J^{(i)} \\ \tilde{F}^{(i)}(Q, \eta^{(i)}) &= (\eta_t^{(i)} Q + \eta_x^{(i)} E + \eta_y^{(i)} F)/J^{(i)} \\ J^{(i)} &= \xi_x^{(i)} \eta_y^{(i)} - \eta_x^{(i)} \xi_y^{(i)}\end{aligned}\tag{37}$$

The notation $\hat{E}^{(i)}(Q, \xi^{(i)})$ and $\hat{F}^{(i)}(Q, \eta^{(i)})$ is used to show the dependence of these quantities on the metrics of the transformation. Let the conservative difference schemes used to integrate equation (36) be given by

$$\frac{\Delta \tilde{Q}_{l,m}^{(1)}}{\Delta \tau^{(1)}} + \frac{\hat{E}_{l+1/2,m}^{(1)} - \hat{E}_{l-1/2,m}^{(1)}}{\Delta \xi^{(1)}} + \frac{\hat{F}_{l,m+1/2}^{(1)} - \hat{F}_{l,m-1/2}^{(1)}}{\Delta \eta^{(1)}} = 0 \quad (38)$$

and

$$\frac{\Delta \tilde{Q}_{j,k}^{(2)}}{\Delta \tau^{(2)}} + \frac{\hat{E}_{j+1/2,k}^{(2)} - \hat{E}_{j-1/2,k}^{(2)}}{\Delta \xi^{(2)}} + \frac{\hat{F}_{j,k+1/2}^{(2)} - \hat{F}_{j,k-1/2}^{(2)}}{\Delta \eta^{(2)}} = 0 \quad (39)$$

The interior points of each patch are updated using the appropriate metrics and dependent variables. At the patch boundary, once again, the grid points of one patch are updated by integrating the equations of motion (for instance patch 2) and those in the other patch (for instance patch 1) are updated by interpolating the dependent variables of the first patch.

A typical cell RSTU associated with the patch-boundary point $(j,1)$ of patch 2 is shown in figure 8. The points R, S, T, and U are defined as in the previous case. The metrics of the transformation at the point $(j,1)$ are defined in a manner consistent with the shape and size of the cell RSTU, that is,

$$\left. \begin{aligned} (x_{\eta}^{(2)})_{j,1} &= x_{j,3/2}^{(2)} - x_{j,1/2}^{(2)} \\ (y_{\eta}^{(2)})_{j,1} &= y_{j,3/2}^{(2)} - y_{j,1/2}^{(2)} \\ (x_{\xi}^{(2)})_{j,1} &= \frac{1}{2} (x_{j+1,1}^{(2)} - x_{j-1,1}^{(2)}) \\ (y_{\xi}^{(2)})_{j,1} &= \frac{1}{2} (y_{j+1,1}^{(2)} - y_{j-1,1}^{(2)}) \\ x_{j,3/2}^{(2)} &= \frac{1}{2} (x_{j,2}^{(2)} + x_{j,1}^{(2)}) \\ y_{j,3/2}^{(2)} &= \frac{1}{2} (y_{j,2}^{(2)} + y_{j,1}^{(2)}) \end{aligned} \right\} \quad (40)$$

Flux conservation across the line CD (as in the previous case) requires that the following condition be satisfied:

$$\begin{aligned}
& \frac{1}{2} (\hat{F}_{1,1/2}^{(2)} + \hat{F}_{j_{\max},1/2}^{(2)}) + \sum_{j=2}^{j_{\max}-1} \hat{F}_{j,1/2}^{(2)} \\
& = \frac{1}{2} (\hat{F}_{1,m_{\max}-1/2}^{(1)} + \hat{F}_{\ell_{\max},m_{\max}-1/2}^{(1)}) + \sum_{\ell=2}^{\ell_{\max}-1} \hat{F}_{\ell,m_{\max}-1/2}^{(1)} \quad (41)
\end{aligned}$$

Equation (41) assumes that $\Delta \xi^i = 1$ and $\Delta \eta^i = 1$. In order to satisfy equation (41), a running parameter s is established along the line CD. The quantity s represents the distance of a point from the point C along the curve CD. Figure 7 shows the line CD stretched into a straight line along the s axis. Representative numerical values of $\hat{F}_{\ell,m_{\max}-1/2}^{(1)}$ are plotted on the positive y axis and a piecewise constant variation of $\hat{F}_{\ell,m_{\max}-1/2}^{(1)}$ is assumed between grid points as before. Defining the points E and F as before, equation (41) can be satisfied exactly by evaluating $\hat{F}_{j,1/2}^{(2)}$ from

$$\begin{aligned}
\hat{F}_{j,1/2}^{(2)}(Q, \eta_{j,1/2}^{(2)}) &= \int_U^T \frac{\hat{F}_{\ell,m_{\max}-1/2}^{(1)}(Q, \eta_{\ell,m_{\max}-1/2}^{(1)}) ds}{s_{\ell+1/2}^{(1)} - s_{\ell-1/2}^{(1)}} \\
&= \sum_{\ell=p}^q N_{j,\ell} \hat{F}_{\ell,m_{\max}-1/2}^{(1)}(Q, \eta_{\ell,m_{\max}-1/2}^{(1)}) \quad (42)
\end{aligned}$$

where the values of $N_{j,\ell}$ are given by

$$N_{j,\ell} = \begin{cases} 0 & \text{if } s_{\ell+1/2}^{(1)}, s_{\ell-1/2}^{(1)} \leq s_{j-1/2}^{(2)} \\ 0 & \text{if } s_{\ell+1/2}^{(1)}, s_{\ell-1/2}^{(1)} \geq s_{j+1/2}^{(2)} \\ (s_r - s_\ell) / (s_{\ell+1/2}^{(1)} - s_{\ell-1/2}^{(1)}) & \text{otherwise} \end{cases} \quad (43)$$

and

$$s_r = \min(s_{j+1/2}^{(2)}, s_{l+1/2}^{(1)})$$

$$s_l = \max(s_{j-1/2}^{(2)}, s_{l-1/2}^{(1)})$$

The term $(s_{l+1/2}^{(1)} - s_{l-1/2}^{(1)})$ in the denominator of the integral in equation (42) serves to convert the numerical flux $\hat{F}_{l, mmax-1/2}^{(1)}$ into a flux per unit length (the metrics contained within the numerical flux take the length of the side of the cell into account). The integration process reintroduces the length parameter.

The preceding method of obtaining the $\hat{F}_{j, 1/2}^{(2)}$ (eq. (42)) is not freestream preserving. However, a repeated integration of the governing equations with freestream conditions everywhere (as initial conditions), and without boundary conditions on a grid of the type shown in figure 8, resulted in only a 0.1% drift in the density in the vicinity of the patch boundary. It can be shown (ref. 6) that the drift in freestream conditions near the patch boundary is proportional to the curvature of the patch boundary, and is caused by terms that are second order in magnitude. Hence, it behooves the user to use patch boundaries with moderate curvature.

The patch-boundary technique has thus far been developed for a region divided into two adjacent patches. The technique, however, is not restricted to two-patch calculations, but can be generalized to an arbitrary number of patches positioned arbitrarily with respect to each other. As an example of using multiple patches, the region shown in figure 9 is divided into four patches with the use of three patch boundaries. The lines along which a flux balance is carried out are AC, FG, DC, and EB. The shaded areas depict typical cell areas for points situated on the patch boundaries. Grid points that belong to only one patch-boundary usually have four-sided cell areas. However, patch-boundary grid points that are close to the intersection of two or more patch boundaries may sometimes be required to have cell areas that are bounded by more than four sides (point I in fig. 9). These nonstandard cell shapes are required to cover the entire region by cell areas corresponding to grid points which are updated by integrating the equations of motion. The cell areas corresponding to patch-boundary points can be easily determined once the lines along which a flux balance is carried out are established. The evaluation of the fluxes necessary to integrate the nonstandard cells is very similar to the procedure used for standard four-sided cells. Details regarding the treatment of nonstandard cells can be found in reference 6.

The foregoing discussion assumed that the numerical fluxes $\hat{F}_{l, mmax-1/2}^{(1)}$ were readily available. For the first-order scheme an examination of equation (8) will show that only the quantities $Q_{l, mmax-1}^{(1)}$, $Q_{l, mmax}^{(1)}$, and $\eta_{l, mmax-1/2}^{(1)}$ are sufficient to define $\hat{F}_{l, mmax-1/2}^{(1)}$. Since these quantities are easily available, calculation

of $\hat{F}_{\ell, mmax-1/2}^{(1)}$ is a simple matter. However, for the second-order accurate scheme, equation (22) shows that the flux difference

$$\Delta F^-(Q_{\ell, mmax}^{(1)}, Q_{\ell, mmax+1}^{(1)}, \eta_{\ell, mmax-1/2}^{(1)})$$

is required to calculate $\hat{F}_{\ell, mmax-1/2}^{(1)}$. The calculation of this flux difference, in turn, requires the vector $Q_{\ell, mmax+1}^{(1)}$ (the line $mmax+1$ in patch 1 corresponds to the line $k = 2$ in patch 2). The vector $Q_{\ell, mmax+1}^{(1)}$ is determined simply by extrapolating the constant ℓ lines into patch 2 to intersect the line $k = 2$ in patch 2. The values of $Q_{\ell, mmax+1}^{(1)}$ are then interpolated from the values of $Q_{j, 2}^{(2)}$. A simple linear interpolation was used to obtain the results presented later in these notes. An alternative to this procedure, and one that avoids the interpolation procedure described above, is to calculate the flux differences $\Delta F^-(Q_{j, 1}^{(2)}, Q_{j, 2}^{(2)}, \eta_{j, 1/2}^{(2)})$ and to perform a flux balance as follows:

$$\Delta F^-(Q_{\ell, mmax}^{(1)}, Q_{\ell, mmax+1}^{(1)}, \eta_{\ell, mmax-1/2}^{(1)}) = \sum_{j=p}^q N_{\ell, j} \Delta F^-(Q_{j, 1}^{(2)}, Q_{j, 2}^{(2)}, \eta_{j, 1/2}^{(2)}) \quad (44)$$

Notice that in equation (44) the flux balance is being performed in the opposite direction (compared to the flux balance described earlier). Similar procedures, that is, interpolation or an additional flux balance, are required to calculate the numerical flux $\hat{F}_{j, 3/2}^{(2)}$ also. Both the methods, which are described above, do not in any way affect the conservative property of the patch-boundary scheme. The additional flux difference terms that are required to make the scheme second-order accurate are once again perfectly balanced across the patch boundary.

The Implicit, Relaxation Patch-Boundary Scheme

Now that the calculation of the boundary fluxes has been described, all that remains to be seen is how these ideas fit into the implicit, relaxation schemes given by equations (19)-(21) and (24)-(25). The right-hand side of all these equations can be calculated at all grid points in the interior and at the patch boundary, using either the usual definition of numerical fluxes or in the special manner described in the previous subsection.

The pointwise relaxation schemes given by equations (19) and (24) remain completely unchanged except for the right-hand side at patch boundaries. This is

because spatial derivatives of the matrices \tilde{A}^{\pm} and \tilde{B}^{\pm} do not appear on the left-hand side of these equations. For time-asymptotic problems, the number of iterations per time step can be restricted to just one. If for reasons of computational efficiency (increased convergence rates) it becomes necessary to use more than one iteration per time step, then the most reasonable approach seems to be to perform each iteration in all the patches before performing the next iteration.

For the example shown in figure 8, where the constant ξ lines are discontinuous at the patch boundary, the line relaxation schemes given by equations (20) and 25 also remain unchanged as in the case of the pointwise relaxation schemes. This is because the η derivatives of the matrices \tilde{B}^+ and \tilde{B}^- do not appear on the left-hand side of these equations. However, the line relaxation scheme given by equation (21) needs to be modified at the patch boundary of patch 2 because the backward difference $\nabla_{\eta} \tilde{B}_{j,k}^+$ is not defined. Several options are available to overcome this difficulty. The simplest solution would be to revert to the pointwise relaxation scheme at the patch-boundary points, that is,

$$\left[I + \frac{\Delta\tau}{\Delta\xi} (\tilde{A}_{j,k}^+ - \tilde{A}_{j,k}^-) + \frac{\Delta\tau}{\Delta\eta} (\tilde{B}_{j,k}^+ - \tilde{B}_{j,k}^-) \right]^p (\tilde{Q}_{j,k}^{p+1} - \tilde{Q}_{j,k}^p) = \text{RHS of equation (17)} \quad (45)$$

when $k = 1$, and

$$\left[I + \frac{\Delta\tau}{\Delta\xi} (\tilde{A}_{j,k}^+ - \tilde{A}_{j,k}^-) + \frac{\Delta\tau}{\Delta\eta} (\nabla_{\eta} \tilde{B}_{j,k}^+ + \Delta_{\eta} \tilde{B}_{j,k}^-) \right]^p (\tilde{Q}_{j,k}^{p+1} - \tilde{Q}_{j,k}^p) = \text{RHS of equation (17)} \quad (46)$$

when $k \neq 1$. A second approach would be to retain only the diagonal terms from the derivative $\nabla_{\eta} \tilde{B}_{j,k}^+$ which then yields

$$\left[I + \frac{\Delta\tau}{\Delta\xi} (\tilde{A}_{j,k}^+ - \tilde{A}_{j,k}^-) + \frac{\Delta\tau}{\Delta\eta} (\tilde{B}_{j,k}^+ + \Delta_{\eta} \tilde{B}_{j,k}^-) \right]^p (\tilde{Q}_{j,k}^{p+1} - \tilde{Q}_{j,k}^p) = \text{RHS of equation (17)} \quad (47)$$

when $k = 1$, and

$$\left[I + \frac{\Delta\tau}{\Delta\xi} (\tilde{A}_{j,k}^+ - \tilde{A}_{j,k}^-) + \frac{\Delta\tau}{\Delta\eta} (\nabla_{\eta} \tilde{B}_{j,k}^+ + \Delta_{\eta} \tilde{B}_{j,k}^-) \right]^p (\tilde{Q}_{j,k}^{p+1} - \tilde{Q}_{j,k}^p) = \text{RHS of equation (17)} \quad (48)$$

when $k \neq 1$. The results presented in this study (and obtained with the line relaxation schemes) were calculated using equations (47) and (48). The comments made

earlier regarding the number of iterations per time step (for the pointwise relaxation schemes) are valid for the line relaxation schemes also.

The implicit, relaxation, patch-boundary scheme can be summarized in the following steps:

1. Integrate the dependent variables at all the grid points of patch 2 using the pointwise or line relaxation schemes with their special forms at the patch boundary (only one iteration).

2. Interpolate the newly obtained values of $[(Q_{j,1}^{(2)})^{p+1} - (Q_{j,1}^{(2)})^p]$ along the patch boundary to yield a new set of values of $[(Q_{l,mmax}^{(1)})^{p+1} - (Q_{l,mmax}^{(1)})^p]$.

3. Integrate the dependent variables at the grid points of patch 1 using the pointwise or line relaxation schemes (only one iteration) and the most recent values of $[(\tilde{Q}_{l,mmax}^{(1)})^{p+1} - (\tilde{Q}_{l,mmax}^{(1)})^p]$ (a Dirichlet-type boundary condition).

4. Interpolate the values of $(Q_{j,1}^{(2)})^{p+1}$ to obtain the values of $(Q_{l,mmax}^{(1)})^{p+1}$ (discard the ones obtained as a result of the integration).

5. If the maximum value of the magnitudes of all $[(Q^{(i)})^{p+1} - (Q^{(i)})^p]$ is less than the prescribed tolerance limit, go to the next integration step; if not, go back to step 1 and reiterate.

Step 2 and the implementation of the Dirichlet boundary condition in step 3 are not required for pointwise relaxation schemes and line relaxation schemes where the lines are chosen to be of the same family as the patch-boundary line. In the case of implicit, relaxation, patch-boundary schemes one iteration per time step has been found to be sufficient to maintain stability, multiple iterations being required to obtain time accuracy.

The Factored, Implicit Patch-Boundary Scheme

A linearized, implicit scheme requires the linearization of the numerical fluxes. The scheme then entails the solution of a system of linear equations where the unknowns are the incremental changes in the dependent variables at the grid points. The matrix associated with this system of linear equations is sparse, but may have a large bandwidth and is, hence, computationally expensive to solve. The strategies used to overcome this problem are approximate factorization and relaxation procedures. In relaxation procedures, inter-grid point connections are altered using certain approximations which are then accounted for in the iteration process that goes hand-in-hand with relaxation procedures. The new grid point connectivities are chosen such that the associated matrix is much simpler to solve (for example, the matrix is diagonal for pointwise relaxation schemes). In factored, implicit schemes the connectivities between various grid points is retained, but additional connections are brought into play (the factorization error term) so that

the original matrix can be expressed as the product of two or more matrices that are easier to solve (for example, two tridiagonal matrices in eq. (18)).

A linearization of the numerical fluxes in the vicinity of the patch-boundaries results in the incremental changes in the dependent variables on the two sides of the patch boundary becoming coupled. The factored, implicit scheme cannot be factored at the patch boundary. Hence, we resort to the kind of approximations made in the relaxation approach (only at the patch-boundary) and use the iterative technique to correct for the approximations made. Details regarding the factored, implicit scheme can be found in reference 7.

ADDITIONAL TOPICS

In this section, we briefly touch upon various topics that are directly related to patched-grid simulations. While these topics are no less important than the patched-boundary method itself, the scope of the current study does not permit an exhaustive development of each one of them.

Stability of Patched-Grid Schemes

The numerical stability of the patched-grid scheme developed in the previous section is demonstrated in a practical manner in the next section by applying it to several example problems. The examples include the motion of strong shocks and other flow discontinuities through patch boundaries (both moving and stationary patches) and, therefore, they amply test the patch-boundary scheme. However, a more formal analysis of stability (even if it is only for the patched-grid scheme applied to a linear differential equation) is a necessity. Reference 11 presents such an analysis for the patch-boundary condition presented here and also for some new ones developed for the finite-volume technique.

Stability analyses for interior grid points are usually performed using a Fourier technique. An alternate method is required to analyze the stability of a scheme when the boundaries of the computational region are also to be included in the analysis, for example, patch boundaries. Reference 11 uses the amplification matrix to test the stability of the interior scheme together with the patch-boundary scheme. This is done by computing the largest eigenvalue and the L_2 norm of arbitrary powers of the amplification matrix. The scheme is stable if and only if

$$||[G(\Delta x)]^n|| \leq K e^{\alpha n \Delta t}; n = 1, 2, \dots$$

where G is the amplification matrix, Δx is a measure of the grid spacing, and K and α are some constants independent of Δx . Unlike traditional stability analyses, using Fourier techniques, this approach relies heavily on numerical methods to compute eigenvalues and L_2 norms of matrices. Reference 11 demonstrates stability

of the patched-grid schemes presented earlier (as applied to a system of linear hyperbolic partial differential equations) and also sheds light on the processes that govern the stability of patched-grid schemes.

Patched-Grid Calculations in Three Dimensions

The patched-grid scheme can be extended in a straightforward manner to three spatial dimensions. Although the programming logic in three dimensions is more complex, conceptually there are no problems in extending the two-dimensional scheme to more dimensions. Preliminary results for an ogive cylinder, with a plane perpendicular to the axis of the ogive cylinder acting as a two-dimensional patch boundary separating two three-dimensional regions agree well with experimental data. The factored, implicit patched-grid approach was used to develop the three-dimensional code.

The flux balance in three dimensions is performed on a surface instead of a line (CD in fig. 8). In order to calculate the interpolation coefficients $N_{j,l}$, the overlap areas of the control volume sides that come together along the flux balance surface need to be calculated. In the case of planar patch boundaries, this amounts to finding the area of overlap of two triangles given the locations of their vertices. This can be a time consuming process depending on the method used. Investigations to find the simplest way of calculating the area of overlap of two general triangles are currently in progress. The interpolation required to enforce the continuity of dependent variables across the patch boundary also needs to be two-dimensional in nature to perform three-dimensional patched-grid calculations. The trial calculation mentioned above uses linear interpolation over triangles. Details of three-dimensional patched-grid calculations will be discussed in a forthcoming article.

Patched-Grids and Navier-Stokes Calculations

The Navier-Stokes equations can be written in the conservation-law form (just as the Euler equations were in eq. (1)), with the use of viscous flux vectors. These viscous flux vectors can be balanced across the flux balance line in a manner identical to the inviscid flux balance discussed in the last section. The viscous fluxes depend on both the dependent variables and their spatial derivatives. These fluxes can be evaluated using the dependent variables and their derivatives on one side of the patch boundary, and used to update the dependent variables on the other side of the patch boundary.

However, in many situations a much simpler technique may suffice. Most viscous calculations in the area of applied aerodynamics are performed with the thin-layer Navier-Stokes equations. The viscous terms in the direction parallel to the body surface are assumed to be negligible in comparison with the viscous terms in the direction normal to the body surface to obtain the thin-layer equations. Even in cases where this assumption does not hold true, the computer speeds and memory

available currently preclude the use of very fine grids in more than one spatial direction. Coarse grids will not resolve viscous terms and, hence, retaining viscous terms in a direction in which the grid is coarse does not serve any purpose (the magnitude of the viscous terms calculated on such grids will be negligibly small compared to the other terms). Most practical applications will require the use of patch boundaries that intersect the surface boundary and not patch boundaries that closely follow the surface (or are parallel to the surface). The use of the thin-layer equations in such situations does not require a flux balance of the viscous terms. However, the patch-boundary condition can be made fully conservative, with very few modifications, for the complete Navier-Stokes equations if the need arises.

Higher-Order Accurate Patch-Boundary Conditions

The linear interpolation used to enforce continuity of the dependent variables across the patch boundary and the piecewise-constant variation of the numerical fluxes assumed for the initial development of the patch-boundary condition lead to first-order accuracy at the boundary (even if the interior scheme is second-order accurate in nature). Further, a sudden change in spacing (spacing normal to the patch boundary) across the patch boundary could lead to additional deterioration of the solution accuracy in the vicinity of the patch boundary. To overcome these problems, it is necessary to use higher-order accurate interpolation schemes and a piecewise linear (or more accurate) variation of the numerical fluxes. In addition, the accuracy with which numerical fluxes are calculated must be made independent of sudden jumps in spacing (in the direction normal to the patch boundary). Higher-order accurate interpolation schemes must be used with care because they may result in unstable patch-boundary procedures. Higher-order accurate patch-boundary procedures are currently being investigated and will be discussed in a future article.

RESULTS

Results are presented in this section for inviscid supersonic flow past an 80° segment of a cylinder, subsonic flow past a full cylinder, blast-wave diffraction by a ramp, vortex motion through a patch boundary and time-dependent flow past airfoils that move relative to each other. The unsteady Euler equations are integrated in time in all these cases. The results presented in this section were obtained with the explicit, factored implicit and implicit-relaxation schemes and give a flavor of the quality of solutions possible with each scheme. The case of supersonic flow over a cylinder demonstrates the shock-capturing quality of the various schemes and the convergence rates possible with each one. The blast-wave simulation shows the applicability of patched grids in situations requiring selective grid refinement and the vortex calculation shows the time-accuracy of the patch-grid schemes and the distortion-free motion of vortices through patch boundaries. The subsonic cylinder case demonstrates the time-accuracy of the implicit-relaxation patch-boundary scheme and the feasibility of performing calculations on patches that move relative to each

other. The double-airfoil calculation shows the applicability of the moving-patch technology to rotor-stator interaction calculations.

Cylinder in a Supersonic Free Stream

The first test case is that of a cylinder in a supersonic free stream ($M_\infty = 2$) with the associated bow shock. Figure 10 shows the grid used for the calculation. The region of interest was divided into two patches separated by the patch boundary AB. The discontinuity of the constant ξ grid lines at the patch boundary is evident. The values of the dependent variables at all the grid points were set equal to their free stream values initially. The equations of motion together with the various boundary conditions were integrated (including the patch-boundary conditions) until the solution converged to its steady-state value.

Figure 11 shows the pressure contours obtained at convergence with the explicit, first-order accurate Osher scheme and the explicit patch-boundary scheme. The contour lines can be seen to be continuous across the patch boundary (AB). In fact the contour lines seem almost slope continuous across AB. The square symbols in this figure (and the following figures pertaining to the cylinder) represent the shock position predicted by another numerical approach in reference 26. The captured shock is a little to the left of the predicted shock. This discrepancy is characteristic of the first-order accurate Osher scheme and will disappear with the use of a second-order accurate integration scheme.

The bow shock associated with the supersonic flow over a cylinder first appears at the surface of the cylinder and then moves outward to its final converged position (for the initial conditions chosen). Figures 12-15 depict pressure contours showing the progression of the shock through the grid system. The results in figures 12-15 were obtained with the first-order accurate, implicit, relaxation scheme, and the corresponding implicit patched-grid scheme. The pointwise relaxation technique was employed for this calculation. Because of the large transients that occur during the first few steps of the calculation, the CFL number was initially restricted to 10.0 (the first 10 steps) and thereafter increased to 500.0. The use of CFL numbers larger than 500.0 did not alter the convergence rate.

Figure 12 shows the pressure contours after 20 integration steps. The shock at this instant in time is quite distant from the patch boundary. Figure 13 shows the pressure contours after 35 steps, and figure 14 the contours after 60 steps. The smooth transition of the shock from patch 1 to patch 2, even at a CFL number of 500.0, is evident. Figure 15 presents the pressure contours obtained at convergence (after 280 steps). The continuity of the contour lines across the patch boundary in figures 14 and 15 demonstrate the quality of solutions possible with the present patch-boundary scheme.

Figure 16 displays the convergence history for the explicit first-order scheme and the implicit relaxation first-order scheme. The explicit scheme required approximately 2700 steps to converge. The convergence criterion chosen for this and the following cylinder calculations was

$$|\Delta\rho|_{\max} \leq 5 \times 10^{-4}$$

(based on a freestream density value of 1.0). The relaxation scheme with only one iteration per step required 280 steps to converge; that is, the use of the implicit relaxation scheme increased the convergence rate by a factor of 9.65. Since the implicit scheme required 1.22 times as much computing time per step as the explicit scheme, the actual computing cost was reduced by a factor of 7.91 with the use of the relaxation scheme. It should be remembered that the extra programming required to implement pointwise relaxation is minimal (typically, less than 100 lines of Fortran). Figure 16 also shows the convergence rate for the implicit relaxation scheme when two iterations are used at each time step. The scheme in this case required only 157 steps to converge. However, since it requires approximately twice as much computing time per step (compared to the relaxation scheme with one iteration per step) the total computing cost was almost the same. Figure 17 shows the variation of the magnitude of the maximum residue (R) in the continuity equation as a function of the number of integration steps

$$R = \left| \frac{\hat{E}_{j+1/2,k}^c - \hat{E}_{j-1/2,k}^c}{\Delta\xi} + \frac{\hat{F}_{j,k+1/2}^c - \hat{F}_{j,k-1/2}^c}{\Delta\eta} \right|_{\max}$$

where the superscript c represents the element of the vector corresponding to the continuity equation. The relaxation scheme with one iteration per step reduces R by 9 orders of magnitude in about 1000 steps and the scheme with two iterations per step required about 500 steps to decrease R by the same amount. Table 1 summarizes the convergence rates and computing times for the variants of the first-order accurate Osher scheme mentioned above. All computations were performed on a CRAY-XMP. The computer programs used in the present study were vectorized for use on this machine. Additional information regarding computing times and convergence rates for other relaxation techniques such as the line-relaxation approach can be found in reference 9.

First-order accurate schemes are insufficient to provide accurate results for a general class of problems. In order to obtain reliable results it is necessary to resort to second-order accurate integration schemes. The first-order results presented in this study were included merely to demonstrate the increase in convergence rate (compared to that obtained with the explicit patched-grid scheme). Figure 18 shows the pressure contours obtained at convergence with the implicit, relaxation second-order accurate Osher scheme for the cylinder problem. This scheme uses flux limiters to achieve the TVD property in each dimension. The shock position can be seen to be predicted more accurately than in the previous case. The contours once again transition smoothly across the patch boundary despite the discontinuity of the grid lines.

Figures 19-22 are very similar to figures 12-15 in that they show the progression of the shock through the grid system to its final converged position. However, the results shown in figures 19-22 were obtained with the implicit, factored,

first-order accurate Osher scheme. Once again, because of the large transients that occur in the initial stages of the calculation, the CFL number was restricted to 5.0 in the first 10 steps, and was then held constant at a value of 40.0 for the rest of the calculation. Unlike the implicit relaxation scheme, the implicit factored scheme became unstable for CFL numbers larger than 40.0 for this case. Figures 19, 20, and 21 show the pressure contours obtained after 13, 19, and 24 integration steps, respectively. The shock is seen to be passing through the patch boundary in figure 20, and in figure 21 the shock has passed through the patch boundary. Figure 22 shows the pressure contours at convergence.

Unlike the shock transition, from patch 1 to patch 2 obtained with the implicit, relaxation scheme, the shock transition obtained with the implicit-factored scheme is not distortion free. This can be clearly seen in figures 20 and 21. The oscillations near the shock are seen even before the shock encounters the patch boundary. These oscillations grow larger as the shock passes through the boundary and eventually vanish at convergence (fig. 22) as expected. This phenomenon is because of the inconsistency between the linearization of the fluxes at the patch boundary and the fluxes in the interior of each patch employed in the factored, implicit patched-grid scheme. Such an inconsistency is absent in the case of implicit, relaxation patched-grid schemes where the pointwise relaxation technique or the line-relaxation technique (with the lines chosen to belong to the same family as the patch boundary) are employed. Since the distortion is because of linearization error alone, it vanishes when the solution converges or if the iteration procedure is carried to convergence at each time step. To demonstrate the restoration of the properties of the fully implicit scheme (when the iterations converge), the following test was performed. The solution obtained after 22 integration steps (from the previous calculation) was used as the starting solution and was integrated through two time steps. A CFL number of 40.0 with 5 iterations per step was used. The residual was reduced by approximately an order of magnitude at the fifth iteration. The pressure contours obtained as a result of this calculation are presented in figure 23. Clearly, the oscillations of figure 21 are absent in figure 23 (figs. 21 and 23 can be directly compared since they show pressure contours at the same time step). The monotonicity property is restored, because at convergence, the difference equations corresponding to the fully implicit scheme are satisfied.

Figure 24 shows the convergence history for the factored, implicit, first-order calculation (with the implicit patch-boundary condition) and for the explicit first-order calculation (with the explicit patch-boundary condition). The convergence criterion was chosen to be the same as before. The factored, implicit scheme required 94 steps to converge, whereas the explicit scheme required 2700 steps to converge; that is, the use of the factored, implicit scheme increased the overall convergence rate by a factor of 28.7. However, the factored, implicit scheme with two iterations per time step (the results shown in figs. 19-22 were obtained with two iterations per time step) requires 3.35 times as much computing time per time step as the explicit scheme. Hence, the actual computing cost was reduced by a factor of 8.6 with the use of the factored, implicit scheme. Figure 25 shows the variation of the magnitude of the maximum residual in the continuity equation (R) as

a function of the number of integration steps. The factored, implicit scheme with two iterations per step reduced R by 9 orders of magnitude in about 250 steps. The explicit scheme requires about 3000 steps to reduce R by two orders of magnitude. Table 2 summarizes the computation times and convergence rates for the factored implicit scheme.

Figure 26 displays the pressure contours obtained at convergence with the factored, implicit, second-order accurate Osher scheme. Unlike the implicit, relaxation scheme, the factored implicit scheme does not require the TVD property to be satisfied in each spatial direction. Hence, the fluxes used for the calculation shown in figure 26 were not postprocessed using a flux limiter. For this reason the pressure contours in the vicinity of the shock are oscillatory. However, the oscillations are confined to a small region near the shock.

A general-purpose, patched-grid Euler code should have the capability of handling as many patches as necessary to cover the region of interest. In order to demonstrate the generality of the present patched-grid scheme and its applicability in a general-purpose, patched-grid Euler code, the region of interest for the cylinder was divided into four patches instead of two patches as in the previous case. The patches and the grids for each patch are shown in figure 27. A wide variation in cell shapes and sizes can be seen across each of the three patch-boundaries. Figure 28 shows the pressure contours obtained at convergence with the factored, implicit, first-order accurate Osher scheme. Small changes in contour line slopes can be seen at the patch boundaries. This is because of the sudden change in accuracy caused by the abrupt transition in mesh clustering and will be less noticeable for higher-order accurate schemes. Figure 29 shows the pressure contours obtained with the factored, implicit, second-order accurate Osher scheme. Once again, the contours are continuous across the patch boundaries (and slope continuous unlike the contours in fig. 28). The smooth transition of the shock from patch 2 to patch 4 emphasizes the quality of solutions possible with the patched-grid schemes presented here.

Blast-Wave Diffraction by a Ramp

As stated earlier, one of the main advantages of being able to perform patched-grid calculations is that one can selectively refine the grid in certain areas of the flow region without having to maintain grid-line continuity across patch boundaries. The problem of blast-wave diffraction by a ramp with its attendant complex shock patterns is a typical example of a problem requiring selective refinement of the grid. The grid used for the calculation presented here is shown in figure 30. The calculation was performed with an incident shock Mach number of 7.1, a ramp angle of 49° and a ratio of specific heats (γ) of 1.55. A double Mach reflection occurs for this choice of flow parameters. The discontinuities for this configuration include the incident shock, a kinked reflected shock, two Mach stems, and two slip lines. The region in which the triple point and Mach stems occur (the area covered by patch 2) requires a very fine grid in order to resolve all the flow

features. A very coarse grid is sufficient for the area covered by patch 3 because the independent variables are constant in this region.

The solution to the blast-wave diffraction problem is self similar in time and, hence, can be made to have an asymptotic limit in computational space with the help of a similarity transformation. Details of the similarity transformation can be found in reference 27. Figure 31 shows the isobars obtained at convergence with the explicit, first-order accurate Osher scheme. The kinked reflected shock (ABC), the incident shock (CD), and the first Mach stem (CE) are seen to be captured very sharply. In addition, the second Mach stem (much weaker than the first) can be seen emanating from the point B. The reflected shock passes through the patch boundary FG without any distortion; it merely becomes thinner in patch 2 because of the fine grid used in this patch. Figure 32 shows the density contours obtained at convergence. The additional feature that this figure brings to light is the first slip line emanating from the triple point C. The second slip line, which is supposed to emerge from point B, is much weaker than all the other discontinuities, and hence, cannot be seen in this figure.

Vortex Motion Through a Patch Boundary

This calculation consisted of a Lamb-type analytical vortex moving through a patch boundary. It is possible to affect vortex motion either by superimposing a moving free stream condition (in which case the vortex is convected along with the fluid at the free stream velocity), or by keeping the vortex stationary and moving the grid. The two approaches yield identical results. In this study the vortex was initialized using the procedure given in reference 28 and then the grid was moved at a constant speed in a direction opposite to the direction in which vortex motion was desired. Figure 33 shows the two-patch grid used for the calculation. Only the central portion of the flow field is presented in figures 33-38 since the essential features of the vortex are contained in this region. The discontinuous nature of the grid lines at the patch boundary is evident. The calculation was performed with the factored, implicit, second-order accurate Osher scheme and three iterations per step. Second-order accuracy in time was achieved by using a three-point backward difference for the time derivative on the right-hand side of equation (23).

Figure 34 shows pressure contours at initialization. The solid core at the center of the constant pressure circles in this figure and the following figures that show pressure contours, is the analytical center of the vortex. Figure 35 shows pressure contours after 85 integration steps. The slope continuity of the contour lines across the patch boundary is clearly seen. The center of the circles coincides with the analytical center of the vortex (this demonstrates the time-accuracy of the patched-grid scheme). Figure 36 presents pressure contours obtained after 180 integration steps. The vortex has moved entirely into patch 2. The contours are circular and are not distorted. However, because of asymmetric truncation errors the center of the circles is slightly above the analytical center of the vortex. Figure 37 shows a continuous grid on which the calculation was performed once again. The results of this computation are shown in figure 38 (pressure

contours after approximately 140 integration steps). Once again, a slight upward movement can be observed, demonstrating that this motion is not due to an inaccurate patch-boundary condition.

Cylinder in a Subsonic Free Stream (Moving Patches)

This calculation was performed for a complete cylinder in subsonic flow. The free stream Mach number for the calculation was 0.35. Figure 39 shows the two grids used to perform the calculation. All the grid points were initialized to their free stream values, and the governing equations together with the patch-boundary condition were integrated to convergence (both the grids were stationary for this phase of the calculation). The integration scheme used was the factored, implicit, Beam-Warming scheme in a patched-grid setting (ref. 7). Second-order accuracy in time was achieved as in the previous case. The outer grid was then made to rotate at a constant angular speed. An integration scheme without any truncation error would result in the dependent variables being stationary in physical space, and consequently, contour levels of pressure, density, etc., would also remain stationary (although in computational space, the dependent variables at a grid point of the outer grid would be constantly changing because of the changing physical location of the grid point).

Figure 40 shows the pressure contours obtained at each time step, as the outer grid performed one rotation, plotted on the same figure. The number of integration steps used per rotation was 260. Five iterations were performed at each step in order to reduce the magnitude of the residue by approximately an order of magnitude. For an integration scheme of infinite accuracy, the thickness of the bands would be zero. Since the integration scheme used is only second-order accurate in space and time, the thickness of the contour bands is finite. The thickness of the bands gives a qualitative measure of the time accuracy of the integration scheme coupled with the patched-grid scheme. Further details of this calculation can be found in reference 29. Reference 29 also includes a demonstration calculation which shows that the finite thickness of the contour bands is because of the accuracy of the integration scheme and not because of any inadequacy of the patch-boundary scheme.

Time-Dependent Double-Airfoil Calculation

One of the important applications of the patched-grid approach is the treatment of regions that contain bodies which move relative to other bodies such as rotor-stator combinations in turbomachinery. The feasibility of performing such calculations has already been demonstrated in the previous calculation simulating flow over a full cylinder. In this subsection, results obtained with the unsteady Euler equations for a simple rotor-stator configuration in which both the rotor and stator are circular airfoils, are presented. The axial gap between them is 20% of the chord length. The free stream Mach number is 1.5. The integration scheme used is the implicit relaxation second-order accurate Osher scheme. Second-order accuracy

in time is obtained as in the previous case. Flux limiters have been used to make the scheme TVD in each spatial dimension.

Figure 41 shows the two-patch grid used to discretize the region of interest. The grid in patch 2 is stationary (as is the aft airfoil), and the grid in patch 1 is fixed to the first airfoil which is moving vertically downward. Although the grid lines are continuous at the patch boundary in figure 41, a discontinuity in these grid lines will develop as the first airfoil and patch 1 move downward. The patch-boundary points of patch 1 will slip past the patch-boundary points of patch 2.

Periodic boundary conditions are imposed on the upper and lower boundaries of both patches. Free stream conditions are imposed on the left boundary of patch 1, and supersonic exit boundary conditions are imposed on the right boundary of patch 2. The implicit, patch-boundary condition is used at the boundary separating the two patches. Details of the inviscid surface boundary condition used can be found in reference 10.

The calculation was initially performed with both airfoils stationary. After 50 integration steps, the first airfoil was given a downward velocity (the magnitude of the velocity corresponding to a Mach number of 0.1 with respect to free stream conditions), and the calculation was continued until the solution became periodic in time. The calculation was performed at a CFL number of approximately 2.0. At this CFL number, 250 integration steps were required for each cycle (one cycle corresponds to the motion of the upper boundary of patch 1 from its current position to the position occupied currently by the lower boundary of patch 1). Approximately three cycles were required to eliminate the initial transients and to establish a solution that was periodic in time.

Figures 42-47 show pressure contours at various positions of the forward airfoil (with respect to the aft airfoil) as it moves downward. These contours were obtained after the initial transients had subsided. Although the calculation was performed with only two airfoils, for the sake of clarity figures 42-47 depict four airfoils (information regarding the additional airfoils was obtained from the periodicity condition). Figure 42 shows contours at $t = 0.0$ (one cycle corresponds to $t = 1.0$). The downward motion of the forward airfoil results in an effective angle of attack which, in turn, results in an attached oblique shock on the lower side, and a weak expansion fan on the upper side at the leading edge of the first airfoil. The interaction of this shock with the adjacent forward airfoil is clearly seen. A second, weak attached shock is also evident at the trailing edge (lower side) of the forward airfoil. At the position $t = 0.0$, the shock associated with the second airfoil is detached. It is seen impinging on the surface of the adjacent airfoil.

The interaction of the trailing edge shock of the first airfoil and the leading edge shock of the second airfoil is also clear from figure 42. This interaction area moves downward as the first airfoil moves downward. This, in turn, results in the leading edge shock of the second airfoil attaching and detaching periodically from the leading edge. Figures 43-47 depict this attachment/detachment process. In

figure 43 the shock is beginning to reattach. In figure 44 it is a weak attached shock, and in figure 45 it is a strong attached shock (beginning to detach again). It is completely detached in figure 46 and finally, in figure 47 the contours are identical to those in figure 42 thus demonstrating the accuracy of the present technique in calculating periodic flows.

An important feature in figures 42-47 is that the contours are continuous, even slope continuous, across the patch boundary along which grid points from the two grids are slipping past each other. This high degree of continuity is because of the conservative nature of the patched-grid scheme, and the manner in which continuity of dependent variables is enforced across the patch boundary. (Another interesting feature is that the captured shocks are almost oscillation-free. The absence of large oscillations is because of the TVD nature of the integration scheme.)

Figure 48 shows the pressure variation with time at midchord on the lower surface of the aft airfoil. This pressure variation corresponds to the fourth and fifth cycles. Clearly, the pressure is periodic in time, thus demonstrating the capability of the integration, and patch-boundary schemes in simulating periodic time-dependent flow. Figure 49 shows the surface pressure variation at midchord on the upper surface of the aft airfoil. The behavior seen in figure 49 is similar to that seen in figure 48 except for a phase shift and a difference in the mean value of the pressure.

One aspect of rotor-stator configurations that is not represented in the present results is the effect of the aft airfoil on the forward airfoil (the supersonic nature of the flow does not permit such an interaction). However, the patch-boundary conditions presented earlier will accurately simulate such an interaction, if it were present. The calculation of reference 23 (presented in the next section) with purely subsonic flow in the region of interest shows the capability of the patched-grid scheme in accurately predicting such an interaction.

AN APPLICATION TO ROTOR-STATOR INTERACTION

The aerodynamic processes associated with the flow of fluid through turbomachines pose one of the most challenging problems for the computational fluid dynamicist. The unsteady nature of the flow, the complex geometries involved, the motion of some parts of the system relative to others, and the periodic transition of the flow from laminar to turbulent are some of the factors that contribute to the complexity of the problem. A clear understanding of these types of flows is essential for the optimization of the performance of turbomachinery. This section presents an analysis of two-dimensional flow past the rotor-stator configuration of an axial-turbine (ref. 23), using the patched-grid methodology described earlier.

The two-dimensional analysis of stator airfoils in isolation or rotor airfoils in isolation is a relatively straightforward task. Such an analysis is valid when the two rows of blades are set far enough apart that the interaction effects are minimal. However, the desire to minimize engine length requires the stator and

rotor rows to be closely spaced. Clearly, the interaction effects will become more important as the axial gap between the rows is reduced. In fact, the flow becomes periodically unsteady for small values of the axial gap. The experimental results of reference 30 show that the pressure fluctuation (difference between the minimum and maximum pressure values) near the leading edge of the rotor airfoil can be as much as 72% of the exit dynamic pressure when the axial gap is reduced to 15% of the chord length (for the operating conditions and geometry chosen). Hence, it is important that the rotor and stator airfoils be treated as a single system when the interaction effects become predominant. A computational tool which provides the design engineer with the necessary aerodynamic data can be used to great advantage in redesigning rotor and stator airfoils to enhance performance. Such a tool would have to accurately simulate the unsteady flow associated with rotor-stator configurations which exhibit a strong interaction.

The multiple-grid approach can be used to great advantage in simulating the flow associated with rotor-stator configurations. The motion of the rotor airfoil with respect to the stator airfoil makes it impractical to wrap a single grid around both airfoils. It is much simpler to contain the stationary airfoils in one set of grids (grids that are stationary) and the moving airfoils in another set of grids (grids that move along with the airfoils) and to have the two sets of grids communicate with each other using patched-grid technology. The ability to accurately transfer information from patch to patch, in such a situation, has already been demonstrated in the previous section.

One aspect of rotor-stator configurations that is not represented in the rotor-stator results of the previous section is the effect of the aft airfoil on the forward airfoil (the supersonic nature of the flow does not permit such an interaction). However, the patch-boundary conditions were implemented such that an interaction, if present, would be properly accounted for. The calculation presented in this section, with the blade geometry of reference 30 and purely subsonic flow in the region of interest, tests the capability of the patched-grid scheme in accurately simulating such an interaction.

Although the relative merits of overlaid and patched grids have been discussed in the introductory section, the procedures used to transfer information between overlaid grids have not been presented. The main advantage of overlaid grids is that, unlike patched grids, the outer boundaries of the individual grids do not have to conform to each other. This aspect of overlaid grids can be very useful when dissimilar geometries are to be coupled; for example, when a circular body is required to fit into a rectangular flow region as in figures 1(a) and 1(b) (the overlaid approach requires fewer zones). Reference 31 deals with the use of overlaid grids in solving the Euler equations. Encouraging results are presented for several example problems. However, the issues of time-accuracy and conservation are not addressed in reference 31. This section includes the necessary extensions to the overlaid grid technique of reference 31 in order to make it time-accurate.

In this section, both the patched and overlaid grid techniques are used to simulate the flow associated with the rotor-stator configuration of reference 30. The thin-layer, time-dependent, Navier-Stokes equations in two spatial dimensions

are solved using a variant of the Beam-Warming scheme (ref. 5) that is developed in reference 8. Comparisons with the experimental data of reference 30 are also made. The comparisons include time-averaged values of surface pressure, pressure amplitudes and phase relationships.

Integration Method

The integration method used is the factored, implicit algorithm developed earlier with modifications to include the viscous terms. To describe the scheme we consider the unsteady, Navier-Stokes equations in two dimensions

$$Q_t + E_x + F_y = R_x + S_y \quad (49)$$

where the vectors Q , E , and F are given in equation (2). The vectors R and S are given by

$$R = \begin{pmatrix} 0 \\ \tau_{xx} \\ \tau_{xy} \\ \beta_x \end{pmatrix} \quad S = \begin{pmatrix} 0 \\ \tau_{xy} \\ \tau_{yy} \\ \beta_y \end{pmatrix} \quad (50)$$

where

$$\left. \begin{aligned} \tau_{xx} &= 2\mu u_x + \lambda(u_x + v_y) \\ \tau_{xy} &= \mu(u_y + v_x) \\ \tau_{yy} &= 2\mu v_y + \lambda(u_x + v_y) \\ \beta_x &= u\tau_{xx} + v\tau_{xy} + \gamma\mu Pr^{-1}\bar{e}_x \\ \beta_y &= u\tau_{xy} + v\tau_{yy} + \gamma\mu Pr^{-1}\bar{e}_y \\ \lambda &= -2\mu/3 \\ \bar{e} &= p/[\rho(\gamma - 1)] \end{aligned} \right\} \quad (51)$$

Making the independent variable transformation given in equation (4) and the thin layer approximation (ref. 32), we obtain

$$\tilde{Q}_\tau + \tilde{E}_\xi + \tilde{F}_\eta = Re^{-1}\tilde{S}_\eta \quad (52)$$

where \tilde{Q} , \tilde{E} , and \tilde{F} are given in equation (6) and the vector \tilde{S} is given by

$$\tilde{S} = \begin{pmatrix} 0 \\ K_1 u_\eta + K_2 \eta_x \\ K_1 v_\eta + K_2 \eta_y \\ K_1 \{ \text{Pr}^{-1} (\gamma - 1)^{-1} (a^2)_\eta + [(u^2 + v^2)/2]_\eta \} + K_2 (u \eta_x + v \eta_y) \end{pmatrix} \quad (53)$$

and

$$K_1 = \mu(\eta_x^2 + \eta_y^2)$$

$$K_2 = \mu(\eta_x u_\eta + \eta_y v_\eta)/3$$

Equations (52) and (53) assume that the body surface is a constant η line (in incorporating the thin-layer approximation).

The factored, implicit algorithm for the unsteady, thin-layer, Navier-Stokes equations is given by

$$\begin{aligned} & \left[I + \frac{\Delta \tau}{\Delta \xi} (\nabla_\xi \tilde{A}_{j,k}^+ + \Delta_\xi \tilde{A}_{j,k}^-) \right]^p \left[I + \frac{\Delta \tau}{\Delta \eta} (\nabla_\eta \tilde{B}_{j,k}^+ + \Delta_\eta \tilde{B}_{j,k}^- - \text{Re}^{-1} \delta_\eta \tilde{M}) \right]^p (\tilde{Q}_{j,k}^{p+1} - \tilde{Q}_{j,k}^p) \\ &= -\Delta \tau \left(\frac{\tilde{Q}_{j,k}^p - \tilde{Q}_{j,k}^n}{\Delta \tau} + \frac{\hat{E}_{j+1/2,k}^p - \hat{E}_{j-1/2,k}^p}{\Delta \xi} + \frac{\hat{F}_{j,k+1/2}^p - \hat{F}_{j,k-1/2}^p}{\Delta \eta} \right. \\ & \quad \left. - \frac{\hat{S}_{j,k+1/2}^p - \hat{S}_{j,k-1/2}^p}{\text{Re} \Delta \eta} \right) \end{aligned} \quad (54)$$

where

$$\tilde{A}^\pm = (\partial \tilde{E} / \partial \tilde{Q})^\pm$$

$$\tilde{B}^\pm = (\partial \tilde{F} / \partial \tilde{Q})^\pm$$

$$\tilde{M} = \partial \tilde{S} / \partial \tilde{Q}$$

and Δ , ∇ , and δ are forward, backward, and central difference operators, respectively. The quantities $\hat{E}_{j+1/2,k}$, $\hat{F}_{j,k+1/2}$, and $\hat{S}_{j,k+1/2}$ are numerical fluxes consistent with the physical fluxes \tilde{E} , \tilde{F} , and \tilde{S} . When second-order accuracy in time is required, the term $(\tilde{Q}_{j,k}^p - \tilde{Q}_{j,k}^n)$ on the right-hand side of equation (54) must be replaced by $(1.5\tilde{Q}_{j,k}^p - 2.0\tilde{Q}_{j,k}^n + 0.5\tilde{Q}_{j,k}^{n-1})$ in addition to iterating to convergence. Typically, three to four iterations per time step are sufficient to reduce the residual by an order of magnitude or more.

Different choices for the numerical fluxes lead to different integration schemes. The central difference scheme used in this study can be obtained with the numerical fluxes defined as

$$\left. \begin{aligned} \hat{E}_{j+1/2,k} &= \frac{1}{2} [\tilde{E}(Q_{j,k}, \xi_{j+1/2,k}) + \tilde{E}(Q_{j+1,k}, \xi_{j+1/2,k})] \\ \hat{F}_{j,k+1/2} &= \frac{1}{2} [\tilde{F}(Q_{j,k}, \eta_{j,k+1/2}) + \tilde{F}(Q_{j,k+1}, \eta_{j,k+1/2})] \\ \hat{S}_{j,k+1/2} &= \tilde{S}[Q_{j,k+1/2}, (Q_{\eta})_{j,k+1/2}, \eta_{j,k+1/2}] \end{aligned} \right\} \quad (55)$$

where

$$Q_{j,k+1/2} = \frac{1}{2} (Q_{j,k} + Q_{j,k+1})$$

$$(Q_{\eta})_{j,k+1/2} = Q_{j,k+1} - Q_{j,k}$$

The smoothing terms necessary to stabilize the calculation were included in the numerical fluxes by redefining them to be

$$\begin{aligned} \hat{E}_{j+1/2,k} &= \frac{1}{2} \{ \tilde{E}(Q_{j,k}, \xi_{j+1/2,k}) + \tilde{E}(Q_{j+1,k}, \xi_{j+1/2,k}) \\ &+ \frac{\epsilon}{2} [|\Delta \tilde{E}(Q_{j-1,k}, Q_{j,k}, \xi_{j+1/2,k})| - 2 |\Delta \tilde{E}(Q_{j,k}, Q_{j+1,k}, \xi_{j+1/2,k})| \\ &+ |\Delta \tilde{E}(Q_{j+1,k}, Q_{j+2,k}, \xi_{j+1/2,k})|] \} \end{aligned} \quad (56)$$

where

$$|\Delta \tilde{E}(Q_{j,k}, Q_{j+1,k}, \xi_{j+1/2,k})| = \left| \frac{\partial \tilde{E}}{\partial Q} (Q_{j+1/2,k}, \xi_{j+1/2,k}) \right| (\tilde{Q}_{j+1,k} - \tilde{Q}_{j,k}) \quad (57)$$

The numerical flux $\hat{F}_{j,k+1/2}$ is redefined in a similar manner. The advantage in including the smoothing term in the definition of the numerical flux is that it can also be made conservative across patch boundaries. The term ϵ in equation (56) determines the amount of smoothing used in the calculation, $\epsilon = 1$ corresponding to the amount of smoothing in a fully upwind scheme. Additional details of this smoothing parameter can be found in reference 7.

Grid System for the Rotor-Stator Configuration

The airfoil geometry of reference 30 is much more complicated than the simple circular-arc airfoils used in the previous section. Figure 50 shows the shape of the rotor and stator airfoils, and their orientation relative to each other and the inlet flow direction. The stator and rotor rows consisted of 22 and 28 airfoils, respectively. A Navier-Stokes calculation with a total of 50 airfoils would be extremely time consuming. To overcome this difficulty, the rotor airfoils were enlarged by a factor of $(28/22)$ keeping the pitch to chord ratio the same. It was then assumed (for the calculation) that there were only 22 airfoils in the rotor row. This assumption makes it possible to perform a calculation with only one rotor airfoil and one stator airfoil (a periodicity boundary condition is used to simulate the presence of the rest of the airfoils). The original stator airfoil and the modified rotor airfoil are shown in figure 51. The axial gap between them was chosen to be 15% of the average chord length.

This rotor-stator configuration and the associated flow region can be discretized using only patched grids. However, the number of patches required to solve the problem accurately would be twice as many as required when both patched and overlaid grids are used in conjunction with each other. Hence, a combination of patched and overlaid grids is used in this calculation.

The grid system chosen for the calculation consists of four different zones. The first zone contains the stator airfoil and is discretized with an "O" grid. The second zone contains the rotor airfoil and is also discretized with an "O" grid. These two grids do not overlap one another. Grids 1 and 2 were generated using an elliptic grid generator of the type developed in reference 33, and they are shown in figure 52. The set of grid lines that intersect the airfoil surfaces are orthogonal to these surfaces. Although the actual grids used for the calculation are very dense near the airfoil surfaces (to resolve the viscous effects), for the purpose of clarity figure 52 shows grids in which the points are equispaced in the direction normal to the airfoil surfaces.

Grids 3 and 4 are shown in figure 53. These grids are generated algebraically. Grid 3 contains grid 1 and, consequently, the stator airfoil. Grids 1 and 3 overlap each other and are also stationary with respect to each other. In fact, the inner boundary of grid 3 is contained within grid 1 and the outer boundary of grid 1 is contained within grid 3. This positioning of the boundaries is necessary for the transfer of information between grids 1 and 3. The relationship between grids 2 and 4 is similar to that between grids 1 and 3. Additionally, grids 3 and 4 abut each other along the patch-boundary ABCD (fig. 53). These two grids (3 and 4) slip past each other as the rotor airfoil moves downward. Grids 3 and 4 constitute a patched-grid system. It is advantageous to use a patch boundary (as opposed to an area of overlay) where one system of grids moves relative to another because both time-accuracy and conservation can be more easily controlled in patched-grid calculations.

An interesting feature of grids 3 and 4 as seen in figure 53 is that they do not align with each other. The segment AB of grid 4 does not seem to align with any

part of the patch-boundary of grid 3, and similarly, the segment CD of grid 3 does not seem to align with any part of the patch boundary of grid 4. However, the periodicity boundary condition can be used to solve this problem; the result being that the segment AB is matched with the segment CD. Figure 54 shows all the grids used in the calculation. The relative positions of the boundaries of each grid are clearly seen.

Boundary Conditions

The use of multiple grids in simulating the flow over the rotor-stator configuration shown in figure 51 results in several computational boundaries (fig. 54). The boundary conditions used at each of these boundaries is briefly outlined below.

Natural boundaries- The inner boundaries of the two "0" grids correspond to the airfoil surfaces and, hence, the "no slip" condition and adiabatic wall conditions (or wall temperature) are imposed at these boundaries. It should be noted that in the case of the rotor airfoil "no slip" does not imply zero velocity at the surface of the airfoil; instead, it means that the fluid velocity at the rotor surface is equal to the rotor speed. In addition to the "no slip" condition, the derivative of pressure normal to the wall surface is set to zero. The pressure derivative condition, the adiabatic wall condition and the equation of state together yield

$$\frac{\partial p}{\partial n} = 0$$

$$\frac{\partial e}{\partial n} = \frac{u}{\rho} \frac{\partial \rho u}{\partial n} + \frac{v}{\rho} \frac{\partial \rho v}{\partial n}$$

where n is the direction normal to the airfoil surface. These boundary conditions are implemented in an implicit manner by using the following equation instead of equation (54) to update the grid points on the airfoil surfaces

$$C(\bar{Q}_{j,1}^{p+1} - \bar{Q}_{j,1}^p) + D(\bar{Q}_{j,2}^{p+1} - \bar{Q}_{j,2}^p) = 0 \quad (58)$$

where

$$C = \begin{pmatrix} 1 & 0 & 0 & 0 \\ 0 & 1 & 0 & 0 \\ 0 & 0 & 1 & 0 \\ 0 & \alpha & \beta & 1 \end{pmatrix} \quad D = \begin{pmatrix} \theta & 0 & 0 & 0 \\ 0 & 0 & 0 & 0 \\ 0 & 0 & 0 & 0 \\ 0 & \alpha\theta & \beta\theta & \theta \end{pmatrix}$$

and

$$\theta = - \frac{J_{j,2}}{J_{j,1}}$$

$$\alpha = - \frac{u_{wall}}{\rho_{wall}}$$

$$\beta = - \frac{v_{wall}}{\rho_{wall}}$$

Equation (58) is an implicit, spatially first-order accurate implementation of the "no slip" and adiabatic wall conditions (first-order accurate because the zero normal derivative condition is implemented using a two-point forward difference). A second-order accurate, three-point forward difference corrector step is also implemented after each time step. It should be noted that equation (58) requires the grid to be orthogonal at the airfoil surfaces and the Jacobians of the transformation $J_{j,1}$ and $J_{j,2}$ to be independent of τ .

The left boundary of grid 3 is a subsonic inlet boundary. Three quantities need to be specified at this boundary. Those chosen for this study are (refs. 34 and 35) the Riemann invariants

$$R_1 = u + \frac{2c}{\gamma - 1}$$

$$R_3 = \frac{p}{\rho^\gamma}$$
(59)

and the inlet flow angle which in this case is equivalent to

$$v_{inlet} = 0$$
(60)

The fourth quantity (which is necessary to update the points on this boundary) is also a Riemann invariant

$$R_2 = u - \frac{2c}{\gamma - 1}$$
(61)

and is extrapolated from the interior of grid 3. The manner in which these boundary conditions can be implemented implicitly is described in reference 36.

The calculation assumes that there are an infinite number of rotor and stator airfoils in the positive and negative y directions in figure 51. Hence, a simple periodicity boundary condition is imposed on the upper and lower surfaces of grids 3 and 4. The implicit implementation of this boundary condition is straightforward and will not be discussed here. The right boundary of grid 4 is a subsonic exit boundary. A simple extrapolation procedure is used at this boundary. This boundary condition is implemented implicitly by using the equation

$$(\tilde{Q}_{j_{\max},k}^{p+1} - \tilde{Q}_{j_{\max},k}^p) - \frac{J_{j_{\max}-1,k}}{J_{j_{\max},k}} (\tilde{Q}_{j_{\max}-1,k}^{p+1} - \tilde{Q}_{j_{\max}-1,k}^p) = 0 \quad (62)$$

instead of equation (54) to update the grid points. While the use of equation (62) results in a stable calculation, it may be necessary to specify one condition (such as R_2 or the exit static pressure) to obtain accurate results in the vicinity of the exit boundary. The importance of such a modification to the exit boundary condition is currently being investigated.

Overlap boundaries- The overlap boundary conditions used at the inner boundaries of grids 3 and 4 and the outer boundaries of grids 1 and 2 are extremely simple. They are given by

$$(\tilde{Q}^{p+1} - \tilde{Q}^p)_{o.b.} = 0 \quad (63)$$

where the subscript o.b. refers to the points on the overlap boundary. This is followed by an explicit, corrective, interpolation procedure at the end of each iteration wherein the values of Q^{p+1} along the outer boundaries of grids 1 and 2 are interpolated from the interior grid points of grids 3 and 4, respectively, and the values of Q^{p+1} along the inner boundaries of grids 3 and 4 are interpolated from the interior grid points of grids 1 and 2, respectively (the values of Q^{p+1} obtained from the implicit integration procedure along the overlap boundaries are discarded). The results in this study were obtained using a linear interpolation over triangles.

The boundary condition given by equation (63) is not the same as that given by the following equation

$$(\tilde{Q}^{n+1} - \tilde{Q}^n)_{o.b.} = 0$$

Equation (63) (along with eq. (54) in the interiors of the grids) allows $(\tilde{Q}^{n+1} - \tilde{Q}^n)_{o.b.}$ to assume its right value when the iteration process is carried to convergence (together with the corrective interpolation procedure described above). Both time accuracy and a spatial accuracy consistent with the order of interpolation used are maintained at the overlap boundaries with the use of equation (63).

Patch boundaries- The implicit patched-boundary condition (for the factored, implicit algorithm) is used along patch-boundary ABCD separating grids 3 and 4 (fig. 54). The periodicity condition imposed on the upper and lower boundaries of these two grids implies that the segments AB and CD need to be patched together in the calculation. While this leads to more involved programming logic, the procedure is conceptually straightforward.

Results

In this subsection, we present results obtained for the rotor-stator configuration shown in figure 51. These results were obtained by integrating equation (54) and the boundary conditions described above. Four iterations were performed at each time step. The magnitude of the maximum residual in the system was reduced by more than an order of magnitude at the end of the fourth iteration. Approximately five cycles (a cycle corresponds to the motion of the upper boundary of grid 4 from its current position to the position occupied currently by the lower boundary of grid 4) were required to get rid of the initial transients and to establish a solution that was periodic in time. The calculation was performed at a constant time-step value of 0.04 (the corresponding maximum CFL number in the grid system was approximately 250).

The dependent variables were nondimensionalized with respect to the ambient pressure (p_∞) and density (ρ_∞). This yields

$$u_\infty = M_\infty \sqrt{\gamma}$$

$$v_\infty = 0 \text{ (inlet flow is axial)}$$

where M_∞ is a reference Mach number. For the purpose of initializing the dependent variables in the four grids and also specifying the Riemann invariants R_1 and R_3 , it was assumed that M_∞ was equal to 0.1. However, because the quantities that are prescribed at the inlet boundary are R_1 , R_3 and the inlet flow angle and not the dependent variables themselves, the average Mach number at the inlet (when the solution became periodic in time) was found to be approximately 0.08. The velocity of the rotor airfoil ω was taken to be approximately 1.33 times the average inlet velocity (this is fairly close to the experimental value, which was 1.28).

The Reynolds number for the calculation was chosen to be 100,000/in. The Baldwin-Lomax turbulence model (ref. 37) was used to determine the eddy viscosity. The kinematic viscosity was calculated using Sutherland's law. The viscous terms were evaluated only in grids 1 and 2. It was assumed that because of the sparseness of grid points in grids 3 and 4, the magnitudes of the viscous terms in these grids were negligible.

In the figures that follow, there are several comparisons made with experimental data. The following points must be kept in mind when evaluating these comparisons:

1. The airfoil geometry used in the numerical calculation only approximates that used in the experiment (the actual configuration consisted of 22 stator airfoils and 28 rotor airfoils; the calculation was performed with 22 of each with an enlarged rotor geometry).

2. The rescaling of the rotor geometry requires the modification of the Reynolds number to simulate equivalent conditions in the calculation, and it is not clear how this modification should be effected.

3. The inlet conditions were reasonably close to but not identical with those used in the experiment. Since the quantities that are specified at the inlet are not the dependent variables themselves, it is difficult to exactly specify experimental inlet conditions such as inlet velocity and inlet total pressure. The specification of quantities such as inlet velocity may require an iterative procedure wherein the inlet values of the Riemann variables are continuously modified such that the time-averaged numerical inlet conditions such as velocity and pressure match the time-averaged experimental inlet conditions.

4. The current analysis is only two-dimensional in nature whereas the actual flow is three-dimensional.

5. The axial gap between the airfoils in the experiment was 15% of the chord length. It is difficult to estimate the equivalent axial gap in the case of the modified rotor. The calculation was performed using an axial gap that was 15% of the average chord length.

Time-averaged pressures- Figure 55 shows the time-averaged pressure coefficient (C_p) as a function of the axial distance along the stator airfoil. The pressure coefficient is defined as

$$C_p = \frac{p_{avg} - (p_t)_{inlet}}{(1/2)\rho_{inlet}\omega^2}$$

where p_{avg} is the static pressure averaged over one cycle, $(p_t)_{inlet}$ is the average total pressure at the inlet, and ρ_{inlet} is the average density at the inlet. Clearly, there is a good agreement between theory and experiment. A small separation bubble was found on the trailing edge circle of the stator in the numerical results. This is seen as a sharp dip and rise of C_p toward the trailing edge on the pressure side. The experimental data also indicate such a separation. However, the magnitude of the pressure fluctuation obtained numerically may be suspect because the turbulence model was not tailored to yield accurate estimates of the eddy viscosity in such regions.

Figure 56 shows the time-averaged C_p distribution for the rotor airfoil. The agreement is good except on the suction side of the rotor toward the trailing edge ($4.0 \leq x \leq 7.0$). This difference between experimental and numerical results is probably because of three-dimensional effects (caused by the low aspect ratio of the airfoil). A small separation bubble was found on the pressure side as in the case of the stator. The bubble is seen as a spatial fluctuation in pressure. Once again, the magnitudes of these fluctuations may be inaccurate. It is suspected that the increased mixing that exists in the bubble will result in larger eddy viscosity values and smaller pressure fluctuations in the real case (the sparsity of experimental points precludes any definite conclusions at the present time).

Unsteady pressures- Figure 57 shows the magnitude of the pressure fluctuation \tilde{C}_p along the surface of the stator (plotted as a function of the axial distance). The quantity \tilde{C}_p is defined as

$$\tilde{C}_p = \frac{p_{\max} - p_{\min}}{(1/2)\rho_{\text{inlet}}\omega^2}$$

where p_{\max} and p_{\min} are the maximum and minimum pressures that occur over a cycle at a given point. The agreement between experiment and theory in figure 57 is fairly good considering that in the experiments the rotor moving past the stator is much larger than the actual one. Figure 58 shows the \tilde{C}_p distribution for the rotor. The comparison between experimental and numerical values is not as good as in the case of the stator. However, the numerical calculation does predict all the qualitative features shown by the experiment.

The periodic boundary conditions on the upper and lower boundaries of grids 3 and 4 result in a periodicity in time of the solution within these grids. The pressure and other dependent variables become periodic in time after the initial transients dissipate. Any numerical scheme (including the interior and boundary schemes) that is devised to calculate rotor-stator flow must be able to simulate this periodicity in time. To test this particular capability of the interior integration and boundary schemes, the pressure was monitored at selected locations on the stator. Figure 59(a) shows the locations at which the pressure was monitored, and figures 59(b)-59(d) show the variation of pressure over three cycles, as a function of time, at these locations. The periodicity in time is clearly observed, thus demonstrating the capability of the method in simulating periodic time-dependent flows. The magnitude of the temporal pressure fluctuations vary and was found to be maximum at the point B. A similar test was performed at selected locations on the rotor. The test locations are shown in figure 60(a) and the temporal pressure fluctuations at these locations are shown in figures 60(b)-60(d). Clearly, the fluctuations are periodic in time.

Figure 61 shows a three-dimensional plot of pressure as a function of time and position on the stator. To facilitate comparisons with a similar plot in reference 30 it has been plotted with pressure decreasing in the upward direction (however, the plot in ref. 30 does not contain the mean component of the pressure). This results in low-pressure regions appearing as peaks and high-pressure regions as valleys. The variation of pressure amplitude on the stator can be clearly seen in figure 61. The largest amplitudes occur on the suction side and close to the trailing edge. The amplitudes at the leading edge, and on most of the pressure side, are very small. There is a gradual increase in amplitude as we move from the leading edge to the trailing edge on the suction side. Another interesting feature is the sudden change in amplitude at the trailing edge as one moves from the suction to the pressure side. Figure 61 also shows the phase shift that occurs in the low pressure region L along the suction side. The low-pressure peaks close to the leading edge are almost 180° out of phase with respect to the peaks at the trailing edge. All the features mentioned above agree qualitatively with the experimental data of reference 30.

Figure 62 shows the three-dimensional plot of unsteady pressures for the rotor. The pressures in this case are plotted with increasing values in the upward

direction. The largest amplitudes occur at the leading edge and on the suction side. The pressure amplitudes are rather small at the trailing edge and all along the pressure surface. The amplitudes decay as we move away from the leading edge on the suction surface. There is also an abrupt change in amplitude as we move from the suction to the pressure side at the leading edge. An interesting feature that can be observed in figure 62 is the phase shift that occurs in the high pressure region H as one moves away from the leading edge on the suction surface (the high-pressure peaks occur at different times). As in the previous case, the numerical data agree qualitatively with the experimental data.

While it is difficult to make detailed comparisons of the unsteady pressure surfaces (figs. 61 and 62) obtained experimentally and numerically, it is a relatively simple matter to make comparisons of any one particular feature on these surfaces. Figure 63 shows the phase of the low-pressure region L (fig. 61) for the stator. The plot shows the time at which the low-pressure peak occurs as a function of arc length along the stator. The initial positions ($t = 0$) for the rotor and stator are shown in figure 51. The experimental values are below the numerical values on the pressure side and above the numerical values on the suction side. This is because the frequency at which the rotor airfoils pass the stator airfoils in the experiment is different than that in the calculation (there are fewer rotor airfoils in the calculation). This happens despite the fact that the tangential velocity (ω) of the rotor airfoils is the same in both the experiment and numerical calculation. While the numerical data can be modified to take into effect the differences in blade passing frequency (between the experiment and the calculation), truly accurate phase estimates can be obtained only with a multiple-airfoil calculation.

Mach number contours- Figures 64-66 depict Mach number contours at various positions of the rotor with respect to the stator. Although the calculation was performed with only two airfoils, for the sake of clarity these contour plots depict several airfoils. The information regarding the additional airfoils is obtained from the periodicity condition. The thickening of the boundary layer as we move from the leading to the trailing edges of the rotor and stator is evident. The wakes associated with the airfoils are also clearly seen. In figure 64 the stator wake is below the rotor. In figures 65 and 66 an interaction between the stator wake and the rotor is observed.

Figures 64-66 show contour lines that are smooth and continuous across the patch boundary. However, this is not the case with the contour lines in the vicinity of the overlap boundaries. It was found that the overlap boundaries gave rise to small-amplitude, high-frequency oscillations in the pressure and density values close to the overlap boundaries. The low Mach numbers in the calculation tended to sustain these oscillations because of the decoupling of the continuity, momentum, and energy equations. It is suspected that the overlap boundary procedure gives rise to these oscillations because conservation is not strictly enforced at these boundaries (the patch-boundary condition, on the other hand, is fully conservative).

Areas for Future Research

There are several differences between the experimental conditions and the conditions under which the numerical calculation was performed. Chief among them is the difference in the number of rotor airfoils and the size of these airfoils. To accurately simulate the experimental data one needs to use a minimum of 11 stator airfoils and 14 rotor airfoils (in order to be able to implement the periodicity boundary condition at the proper locations). Such a calculation would be extremely time consuming. A better approach, and one that would justify the necessity for a multiple-airfoil calculation, would be to use 4 stator airfoils and 5 rotor airfoils; a total of 9 airfoils. The ratio of the number of airfoils (rotor vs. stator) for this configuration is $5/4 = 1.250$, whereas the ratio in the real case is $28/22 = 1.273$. Hence, the factor by which the rotor airfoils will have to be enlarged is $1.273/1.250 = 1.018$ instead of the factor 1.273 used in the present calculation. The 9-airfoil calculation should yield better phase relationships and pressure amplitudes.

The second problem that needs to be addressed is the turbulence model. Experience indicates that an algebraic turbulence model does not accurately predict eddy viscosities in regions of separation and in wakes without requiring extensive "fine-tuning" of the model. Hence, it is important to use a more generally applicable turbulence model such as the two-equation models. Preliminary investigations show that the $K - \epsilon$ turbulence model (ref. 38) yields more accurate estimates of the eddy viscosity in the separation regions near the trailing edges of the airfoils and, hence, results in smaller spatial pressure fluctuations.

The conservative treatment of overlap boundaries is much more difficult than the conservative treatment of patch boundaries. For this reason, the overlap boundaries in the present study were not made fully conservative. In the author's opinion this is the cause for the high-frequency oscillations in the dependent variables close to the overlap boundaries. This problem may worsen in situations where there are flow discontinuities passing through overlap boundaries. Hence it is preferable to either use only patched grids for multiple-grid calculations or to develop a simple way of treating overlap boundaries in a conservative manner.

The improvements mentioned above are necessary in order to build a reliable rotor-stator analysis tool. Current research is therefore being focussed on building an unsteady, Navier-Stokes, multiple-blade, patched-grid code which uses a two-equation turbulence model.

SUMMARY

To summarize, these lecture notes give a brief review of the work that has been done in the area of multiple grids, both patched and overlaid grids and then present a patch-boundary condition that was developed by the author. This patch-boundary condition is stable, accurate and easily applicable in generalized coordinate

systems. It is developed for both explicit and implicit integration schemes. In the case of implicit schemes, it is developed within the framework of an iterative implicit procedure that makes possible the decoupling of the calculations in the various patches (decoupling within a time step). The iterative implicit procedure is also included in the text.

Results are presented for a variety of test cases. The example calculations include supersonic flow over a cylinder, blast wave diffraction by a ramp, the motion of vortices through patch boundaries, and subsonic flow over a cylinder demonstrating the feasibility of performing calculations on patches that move relative to each other. These calculations demonstrate the quality of solutions possible with the patch-boundary scheme in terms of both spatial and temporal accuracy.

One of the most important applications of the patched-grid technology is solution of problems that involve the motion of some parts of the system with respect to other parts. Typical examples are rotor-stator interaction in turbomachinery, helicopter rotor-fuselage interaction, propeller-nacelle interaction, and the counterrotating propfan. Two examples of rotor-stator interaction have also been included. The various boundary conditions employed to solve the rotor-stator problem are discussed in some length. Results in the form of steady and unsteady pressures and phase plots are presented. Numerical results are compared with experimental results for one of the cases. A good agreement between experimental and numerical results is obtained.

Current research is focussed on the following areas: (1) making the patch-boundary condition more accurate, and (2) extending the scheme to three-spatial dimensions. Preliminary results in both these areas of investigation have yielded encouraging results.

REFERENCES

1. Rai, M. M.; Chaussee, D. S.; and Rizk, Y. M.: Calculation of Viscous Supersonic Flows Over Finned Bodies. AIAA Paper 83-1667, July 1983.
2. Hennesius, K. A.; and Pulliam, T. H.: A Zonal Approach to Solution of the Euler Equations. AIAA Paper 82-0969, June 1982.
3. Rai, M. M.; Chakravarthy, S. R.; and Hennesius, K. A.: Metric-Discontinuous Zonal Grid Calculations Using the Osher Scheme. International Journal of Computers and Fluids, vol. 12, no. 3, 1984, pp. 161-175.
4. Cambier, L.; Ghazzi, W.; Veuillot, J. P.; et Viviani, H.: Une Approche par Domaines pour le Calcul d'Ecoulements Compressibles. Cinquieme Colloque International sur les Methodes de Calcul Scientifique et Technique, INRIA, Versailles, France, 14-18 Decembre 1981.
5. Beam, R. M.; and Warming, R. F.: An Implicit Factored Scheme for the Compressible Navier-Stokes Equations. AIAA J., vol. 16, no. 4, April 1978, pp. 393-402.
6. Rai, M. M.: A Conservative Treatment of Zonal Boundaries for Euler Equation Calculations. AIAA Paper 84-0164, January 1984.
7. Rai, M. M.: An Implicit Conservative Zonal Boundary Scheme for Euler Equation Calculations. AIAA Paper 85-0488, January 1985.
8. Rai, M. M.; and Chakravarthy, S. R.: An Implicit Form for the Osher Upwind Scheme. AIAA Paper 84-0088, January 1984.
9. Rai, M. M.: A Relaxation Approach to Patched-Grid Calculations with the Euler Equations. AIAA Paper 85-0295, January 1985.
10. Chakravarthy, S. R.: Implicit Upwind Schemes Without Approximate Factorization. AIAA Paper 84-0165, January 1984.
11. Eriksson, L. E.; and Rai, M. M.: A Stability Analysis of Various Patched Grid Interface Conditions for Hyperbolic Equations. To be published.
12. Eriksson, L. E.: Euler Solutions on O-O Grids Around Wings Using Local Refinement. Proceedings of the sixth Gamm Conference on Numerical Methods in Fluid Mechanics, Gottingen, September 25-27, 1985.
13. Usab, W. J.; and Murman, E. M.: Embedded Mesh Solutions of the Euler Equation Using a Multiple-Grid Method. AIAA Paper 83-1946-CP, July 1983.

14. Lombard, C. K.; and Venkatapathy, E.: Implicit Boundary Treatment for Joined and Disjoint Patched Mesh Systems. AIAA Paper 85-1503-CP, July 1985.
15. Lombard, C. K.; Bardina, J.; Venkatapathy, E.; and Olinger, J.: Multi-Dimensional Formulation of CSCM--An Upwind Flux Difference Eigenvector Split Method for the Compressible Navier-Stokes Equations. AIAA Paper 83-1895, July 1983.
16. Berger, M. J.: Adaptive Mesh Refinement for Hyperbolic Partial Differential Equations. Ph.D. Thesis, Department of Computer Sciences, Stanford University, August 1982.
17. Berger, M. J.: On Conservation at Grid Interfaces. ICASE Report No. 84-43, September 1984.
18. Atta, E.: Component Adaptive Grid Interfacing. AIAA Paper 81-0382, January 1981.
19. Atta, E. H.; and Vadyak, J.: A Grid Interfacing Algorithm for Three-Dimensional Transonic Flows About Aircraft Configurations. AIAA Paper 82-1017, June 1982.
20. Steger, J. L.; Dougherty, F. C.; and Benek, J. A.: A Chimera Grid Scheme. Mini-Symposium on Advances in Grid Generation, ASME Applied, Bioengineering and Fluids Engineering Conference, Houston, June 20-22, 1983.
21. Lee, K. D.; Huang, M.; Yu, N. J.; and Rubbert, P. E.: Grid Generation for Three-Dimensional Configurations. NASA CP-2166, October 1980.
22. Yu, N. J.: Transonic Flow Simulation for Complex Configurations With Surface Fitted Grids. AIAA Paper 81-1258, 1981.
23. Rai, M. M.: Navier-Stokes Simulations of Rotor-Stator Interaction Using Patched and Overlaid Grids. AIAA Paper 85-1519-CP, July 1985.
24. Chakravarthy, S. R.; and Osher, S.: High Resolution Applications of the Osher Upwind Scheme for the Euler Equations. AIAA Paper 83-1943, July 1983.
25. Roe, P. L.: Approximate Riemann Solvers, Parameter Vectors, and Difference Schemes. J. Comp. Phys., vol. 43, 1981, pp. 357-372.
26. Lyubimov, A. N.; and Rusanov, V. V.: Gas Flows Past Blunt Bodies. NASA TT-F-715, February 1973.
27. Shankar, V.; Kutler, P.; and Anderson, D. A.: Diffraction of a Shock Wave by a Compression Corner: Part II - Single Mach Reflection. AIAA J., vol. 16, no. 1, January 1978, pp. 4-5.

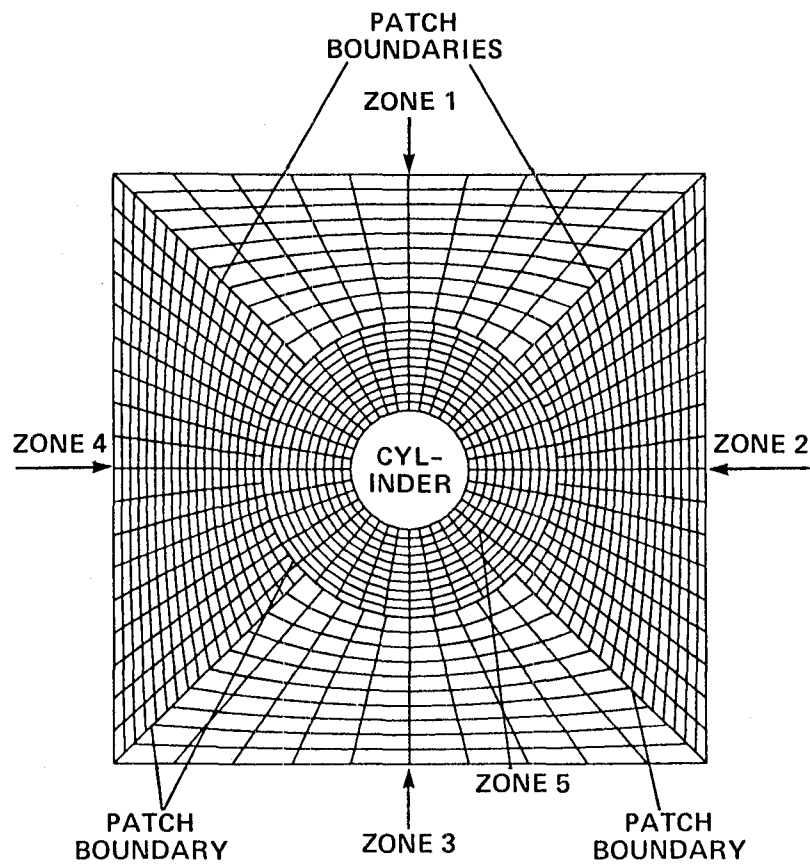
28. Srinivasan, G. R.; McCroskey, W. J.; and Kutler, P.: Numerical Simulation of the Interaction of a Vortex with Stationary Airfoil in Transonic Flow. AIAA Paper 84-0254, January 1984.
29. Hesseinius, K. A.; and Rai, M. M.: Applications of a Conservative Zonal Scheme to Transient and Geometrically-Complex Problems. AIAA Paper 84-1532, June 1984.
30. Dring, R. P.; Joslyn, H. D.; Hardin, L. W.; and Wagner, J. H.: Turbine Rotor-Stator Interaction. J. Eng. for Power, vol. 104, October 1982.
31. Benek, J. A.; Steger, J. L.; and Dougherty, F. C.: A Flexible Grid Embedding Technique with Application to the Euler Equations. AIAA Paper 83-1944, July 1983.
32. Pulliam, T. H., and Steger, J. L.: On Implicit Finite-Difference Simulations of Three Dimensional Compressible Flow. AIAA J., vol. 18, no. 2, February 1980, pp. 159-167.
33. Steger, J. L.; and Sorenson, R. L.: Automatic Mesh-Point Clustering Near a Boundary in Grid Generation with Elliptic Partial Differential Equations. J. Comp. Phys., vol. 33, no. 3, Dec. 1979, pp. 405-410.
34. Salas, M. D.; Jameson, A.; and Melnik, R. E.: A Comparative Study of the Nonuniqueness Problem of the Potential Equation. AIAA Paper 83-1888, July 1983.
35. Pulliam, T. H.; and Steger, J. L.: Recent Improvements in Efficiency, Accuracy, and Convergence for Implicit Approximate Factorization Algorithms. AIAA Paper 85-0360, January 1984.
36. Rai, M. M.; and Chaussee, D. S.: New Implicit Boundary Procedures: Theory and Application. AIAA J., vol. 22, no. 8, Aug. 1984, pp. 1094-1100.
37. Baldwin, B. S.; and Lomax, H.: Thin Layer Approximation and Algebraic Model for Separated Turbulent Flow. AIAA Paper 78-257, January 1978.
38. Chien, Kuei-Yuan: Predictions of Channel and Boundary-Layer Flows with a Low-Reynolds-Number Turbulence Model. AIAA J., vol. 20, no. 1, January 1982.

TABLE 1.- COMPUTING TIMES FOR THE EXPLICIT AND IMPLICIT
RELAXATION SCHEMES

Type of scheme used	Explicit	Implicit relaxation (one iteration/step)	Implicit relaxation (two iterations/step)
Time per 100 steps, sec	2.46	3.00	5.88
Number of steps to converge	2700	280	157
Time to converge, sec	66.42	8.40	9.23

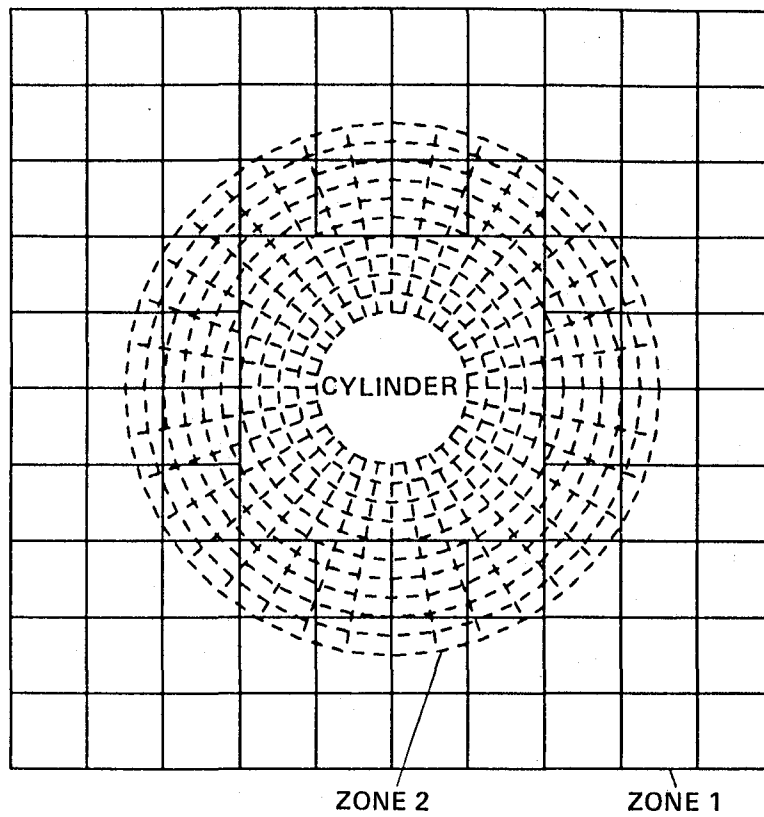
TABLE 2.- COMPUTING TIMES FOR THE FACTORED
IMPLICIT SCHEME

Computation cost parameters	Number of iterations per step	
	1	2
Time per 100 steps, sec	4.19	8.24
Number of steps to converge	Unstable	94
Time to converge, sec	Unstable	7.75



(a) An example of patched grids.

Figure 1.- Types of multiple-grids used in finite-difference calculations.



(b) An example of overlaid grids.

Figure 1.- Concluded.

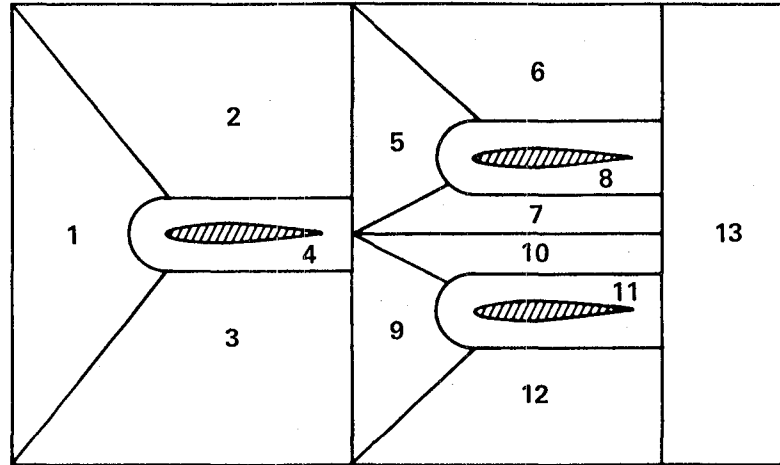
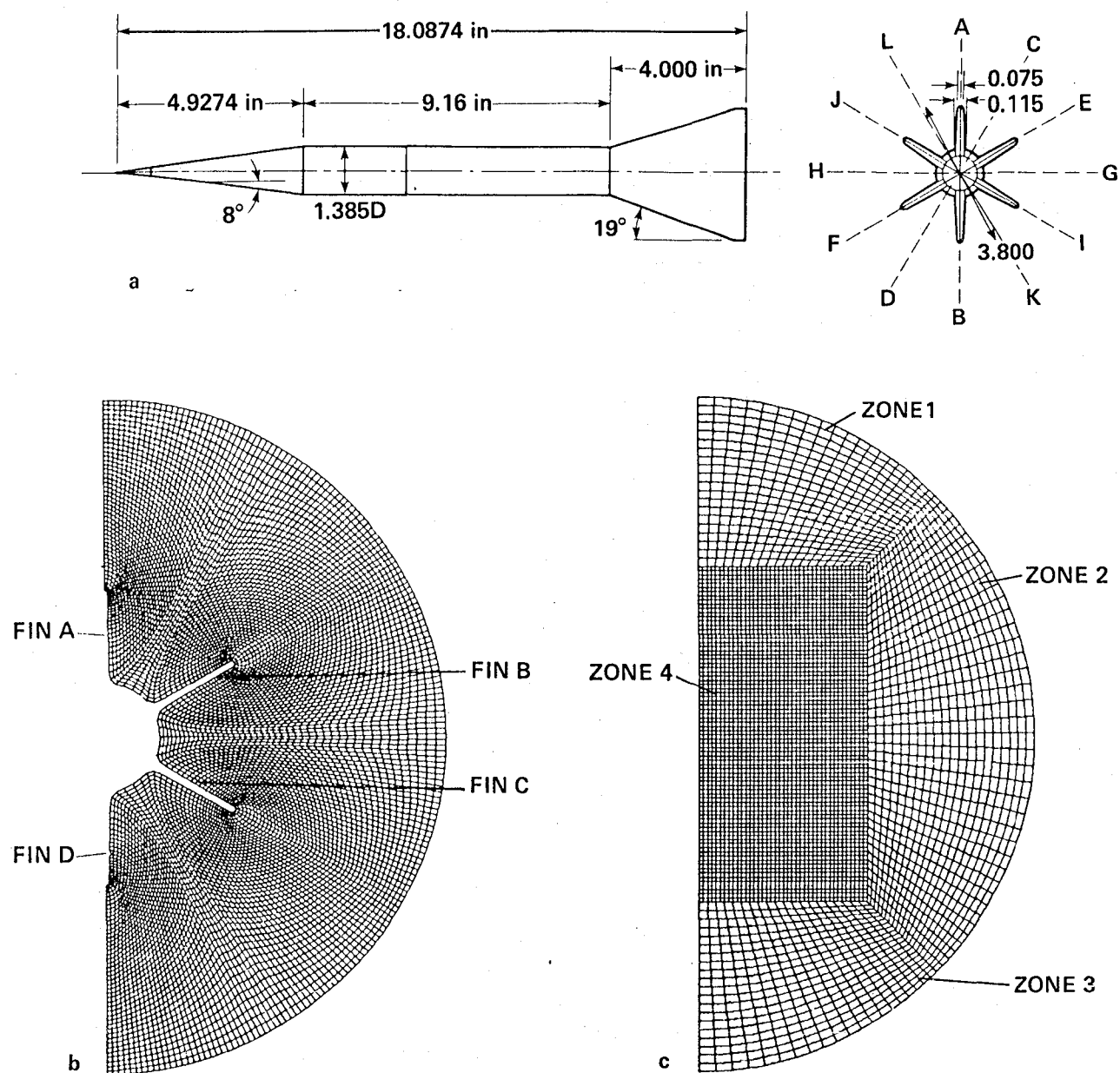


Figure 2.- Zoning of the multiply connected region associated with three airfoils.

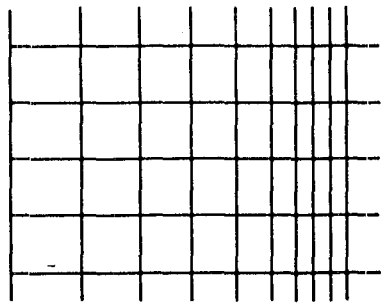


(a) Geometry of projectile.

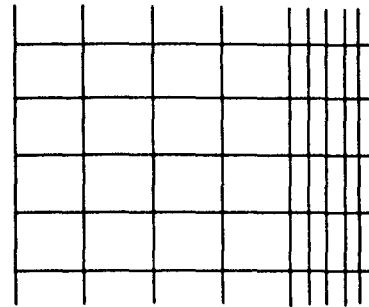
(b) Grid at the aft end (just before the body terminates).

(c) Grid at the aft end (just after the body terminates).

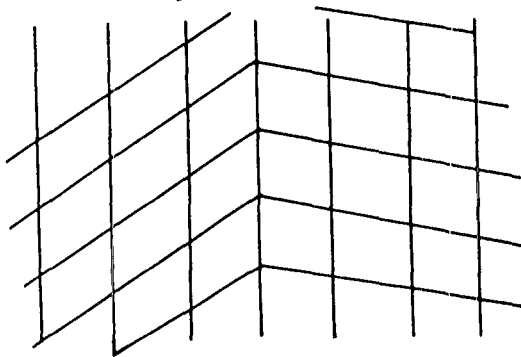
Figure 3.- Finned projectile.



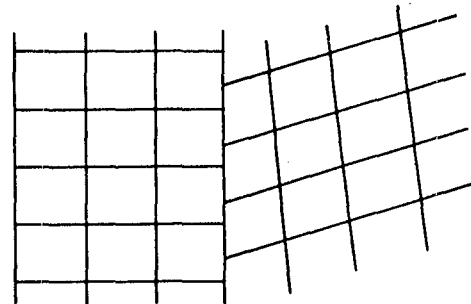
a CONTINUOUS GRID



b METRIC DISCONTINUOUS GRID



c METRIC DISCONTINUOUS GRID



d DISCONTINUOUS GRID

(a) Continuous.

(b) Metric-discontinuous.

(c) Metric-discontinuous.

(d) Discontinuous.

Figure 4.- Types of patched grids used in finite-difference calculations.

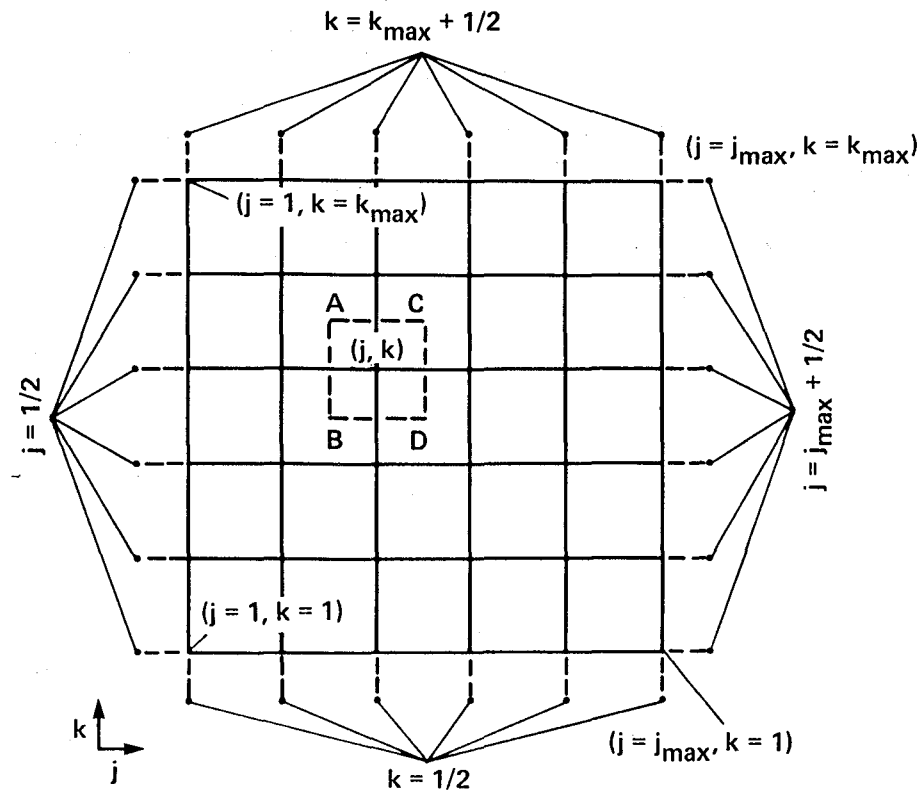


Figure 5.- Grid to illustrate global conservation property of conservative difference operators.

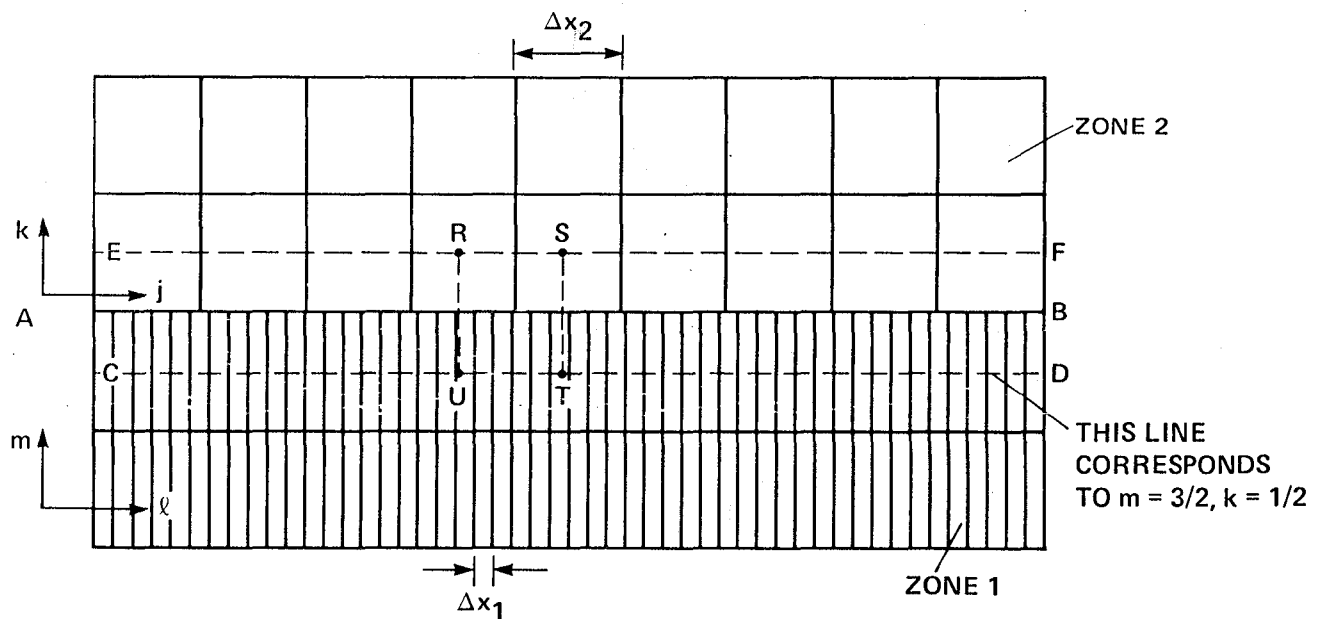


Figure 6.- Two-patch grid to illustrate patched-grid scheme in Cartesian coordinates.

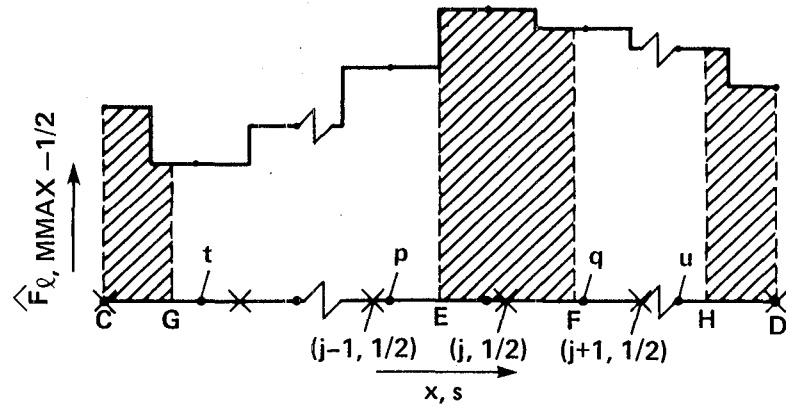


Figure 7.- Piecewise constant variation of the numerical flux \hat{F} as a function of x or s .

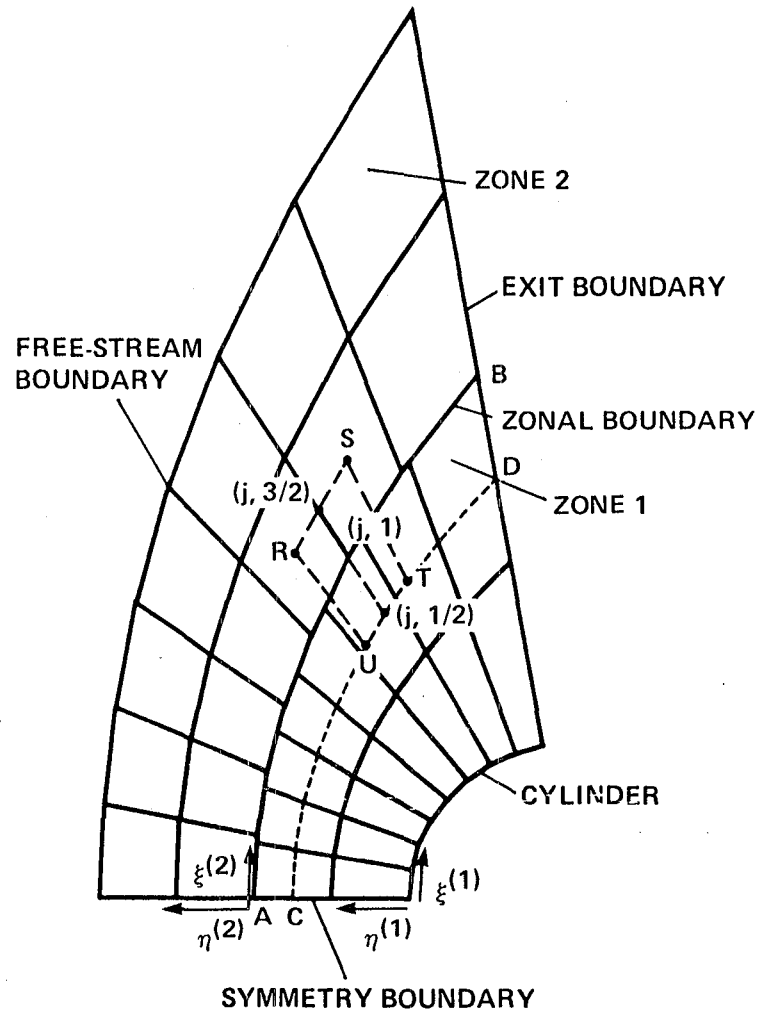


Figure 8.- Two-patch grid to illustrate patched-grid scheme in curvilinear coordinates.

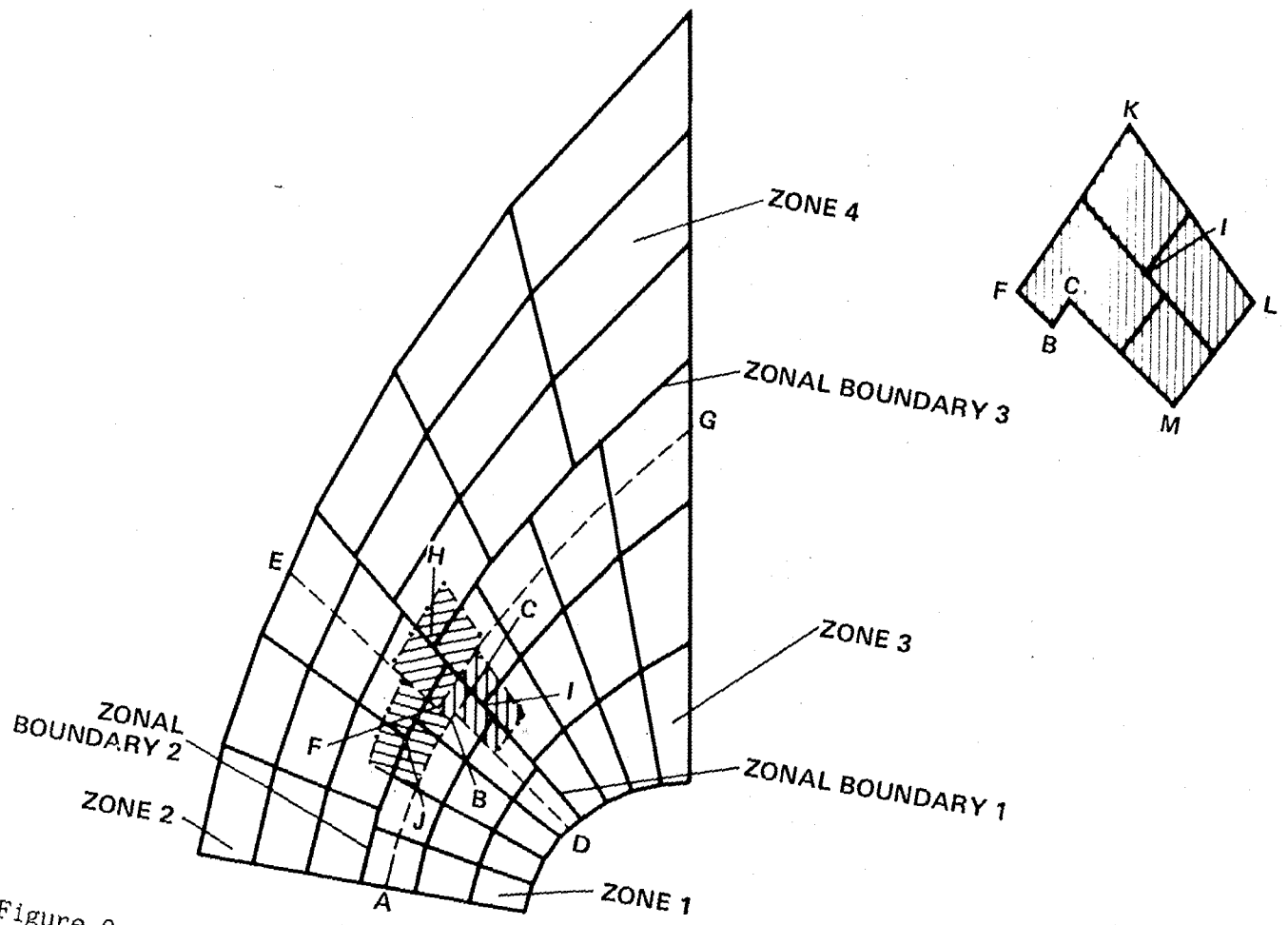


Figure 9.- Four-patch grid to illustrate patched-grid scheme in curvilinear coordinates.

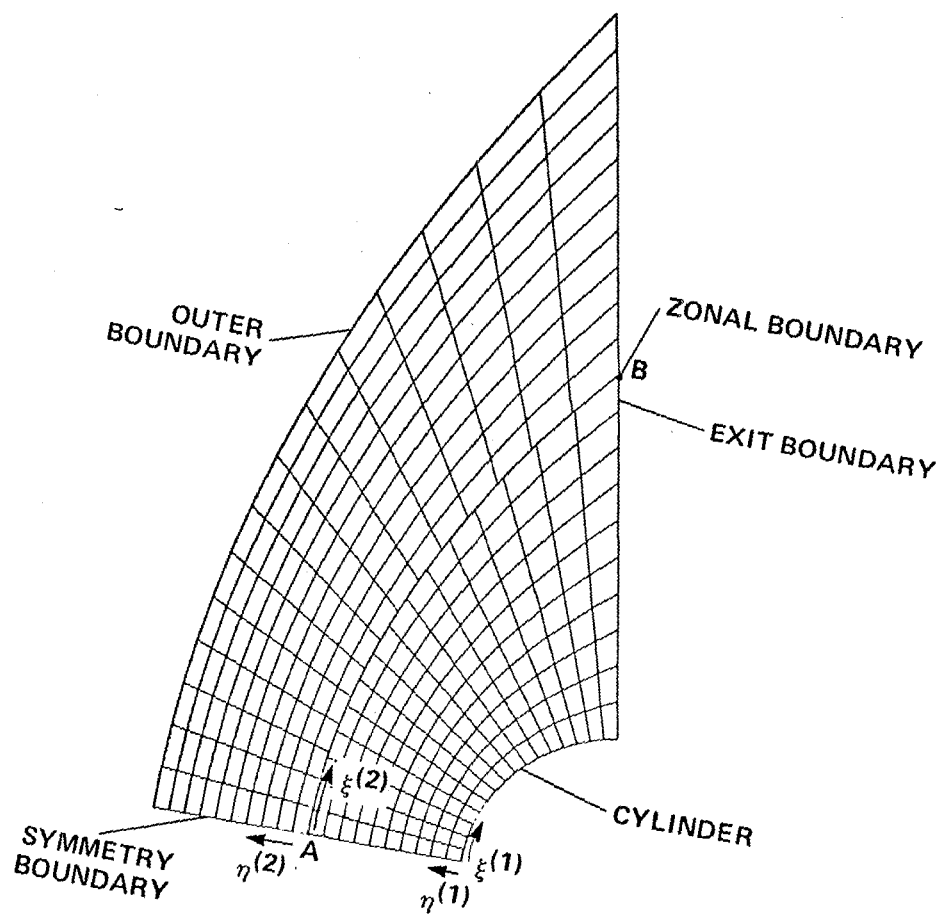


Figure 10.- Grid for two-patch cylinder calculation.

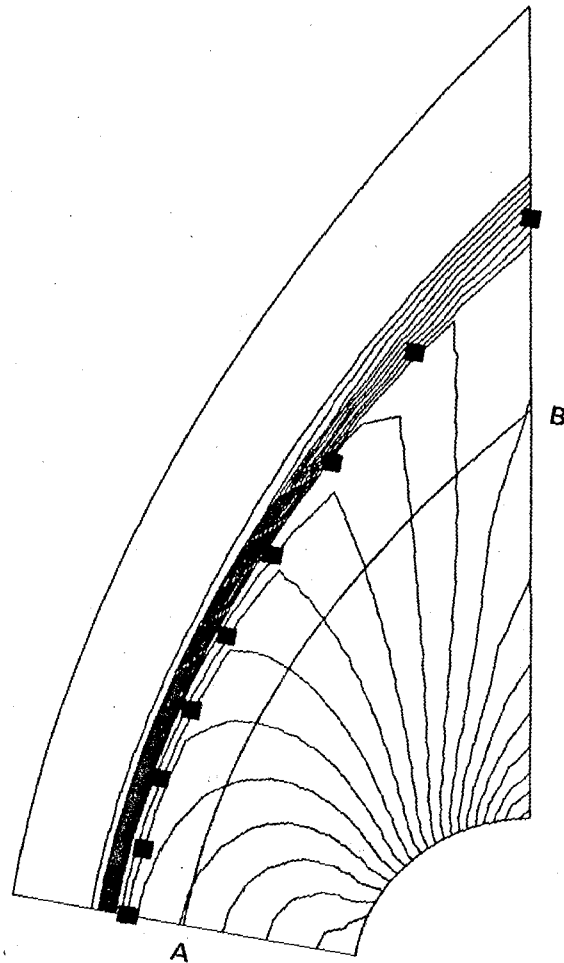


Figure 11.- Isobars at convergence (first-order explicit scheme).

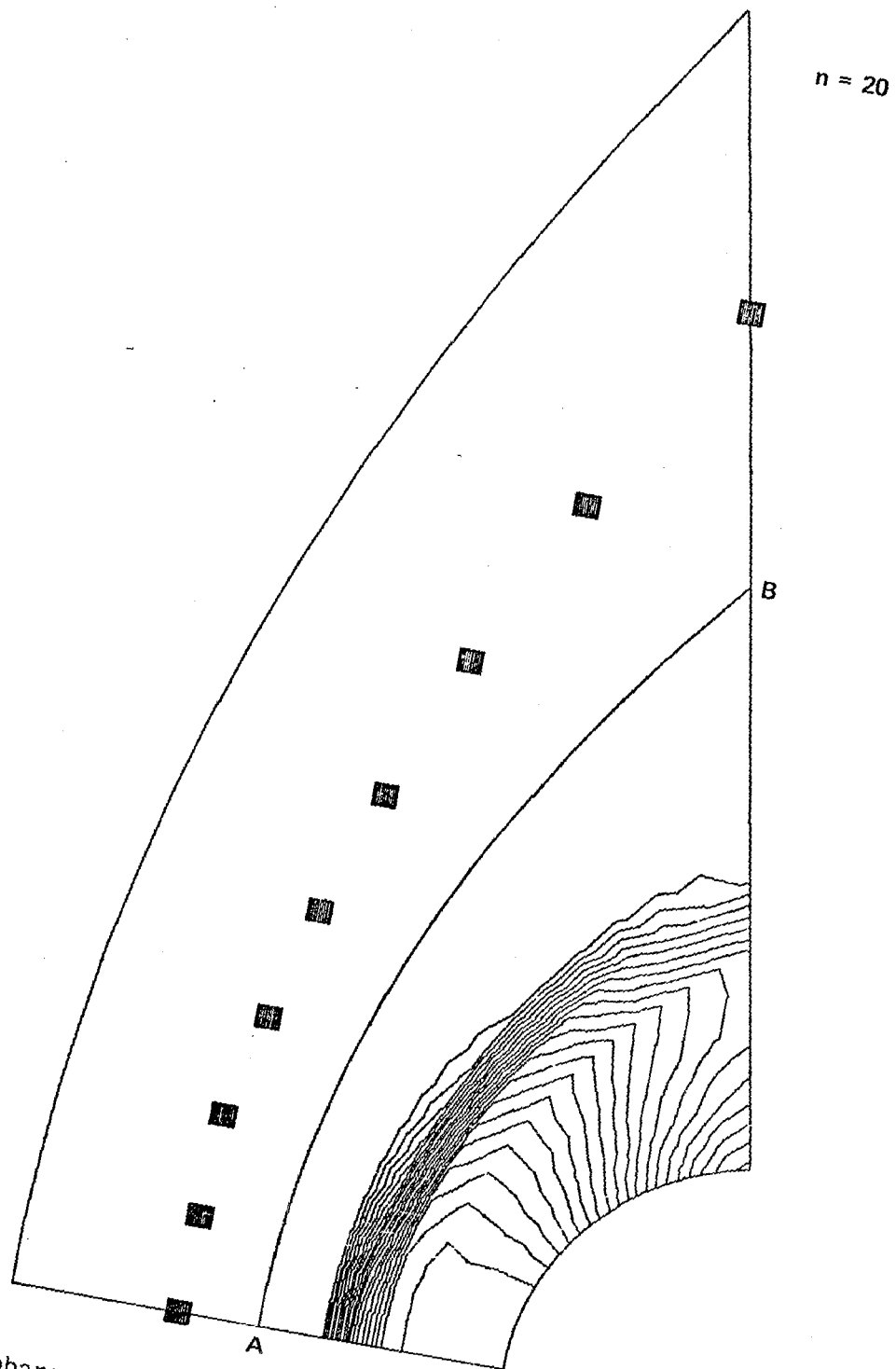


Figure 12.- Isobars after 20 integration steps (first-order relaxation scheme).

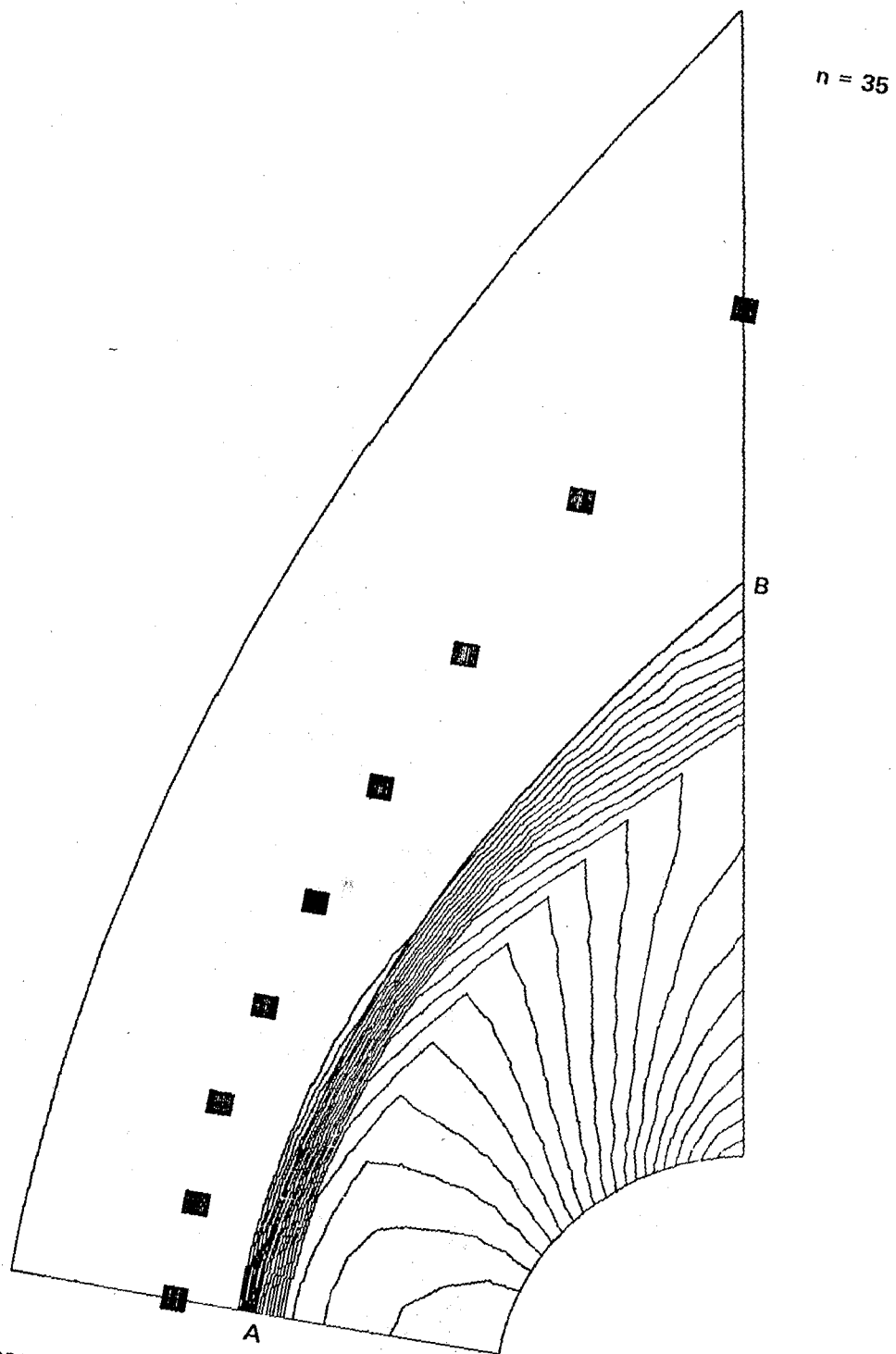


Figure 13.- Isobars after 35 integration steps (first-order relaxation scheme).

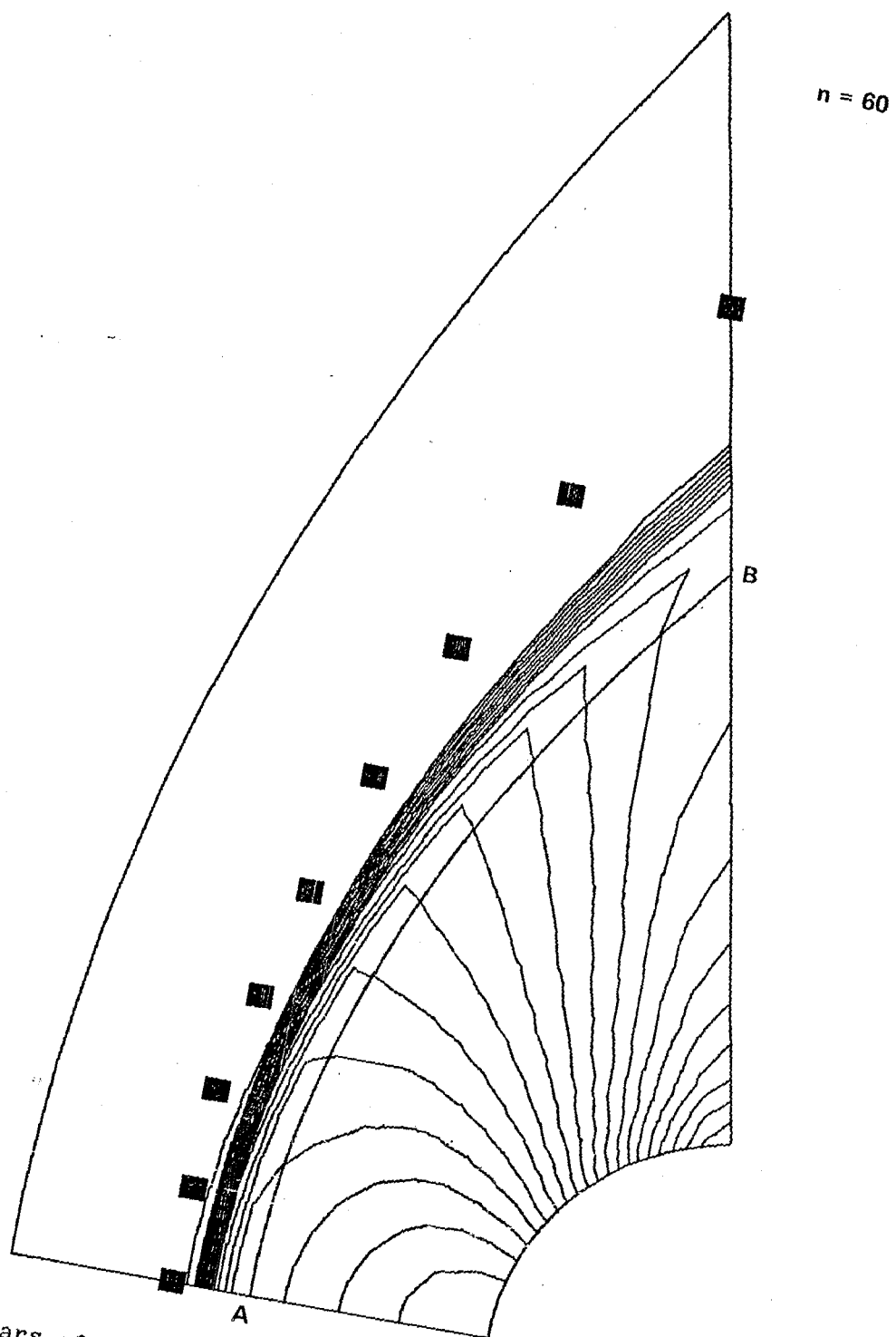


Figure 14.- Isobars after 60 integration steps (first-order relaxation scheme).

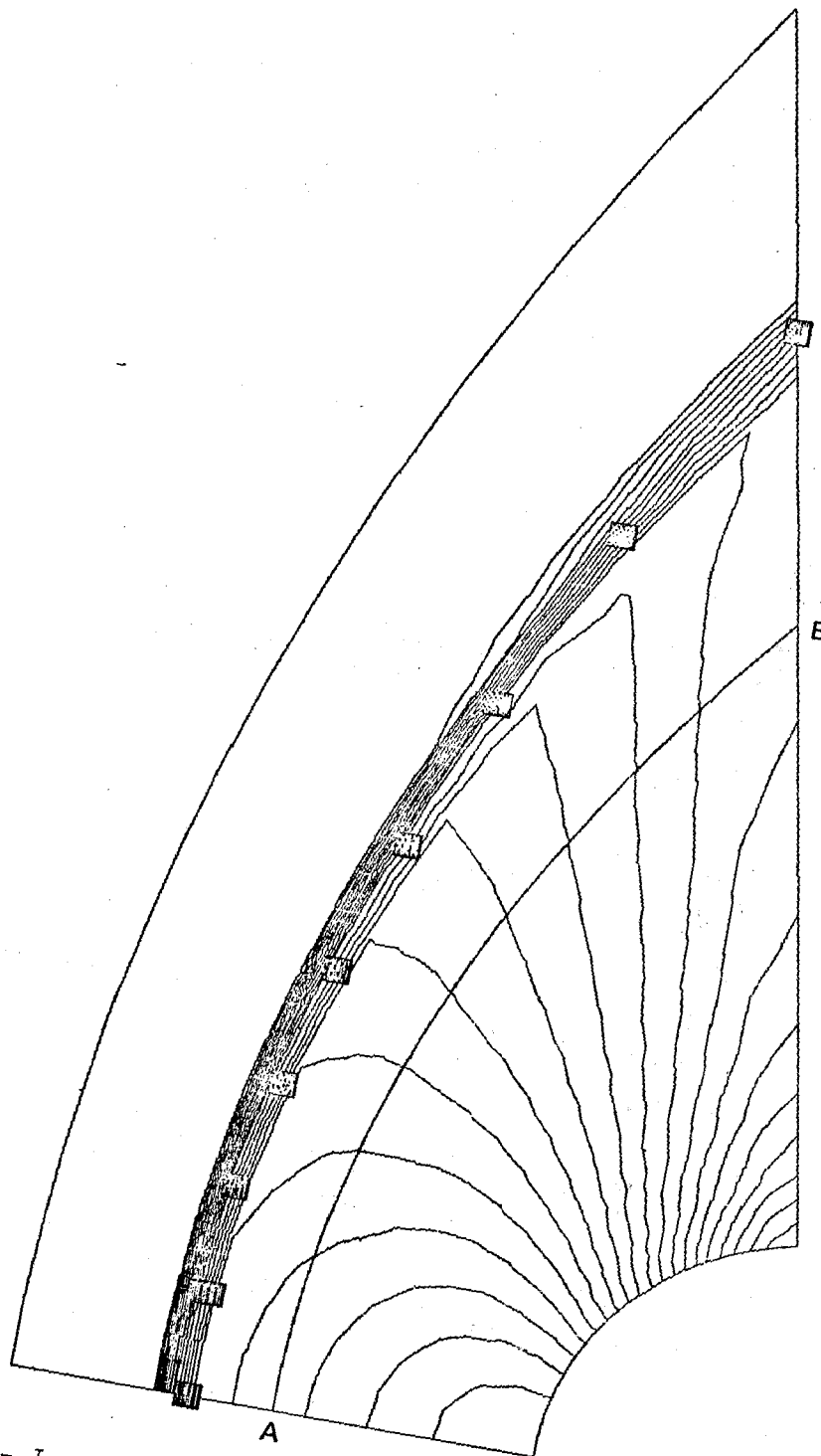


Figure 15.- Isobars at convergence (first-order relaxation scheme).

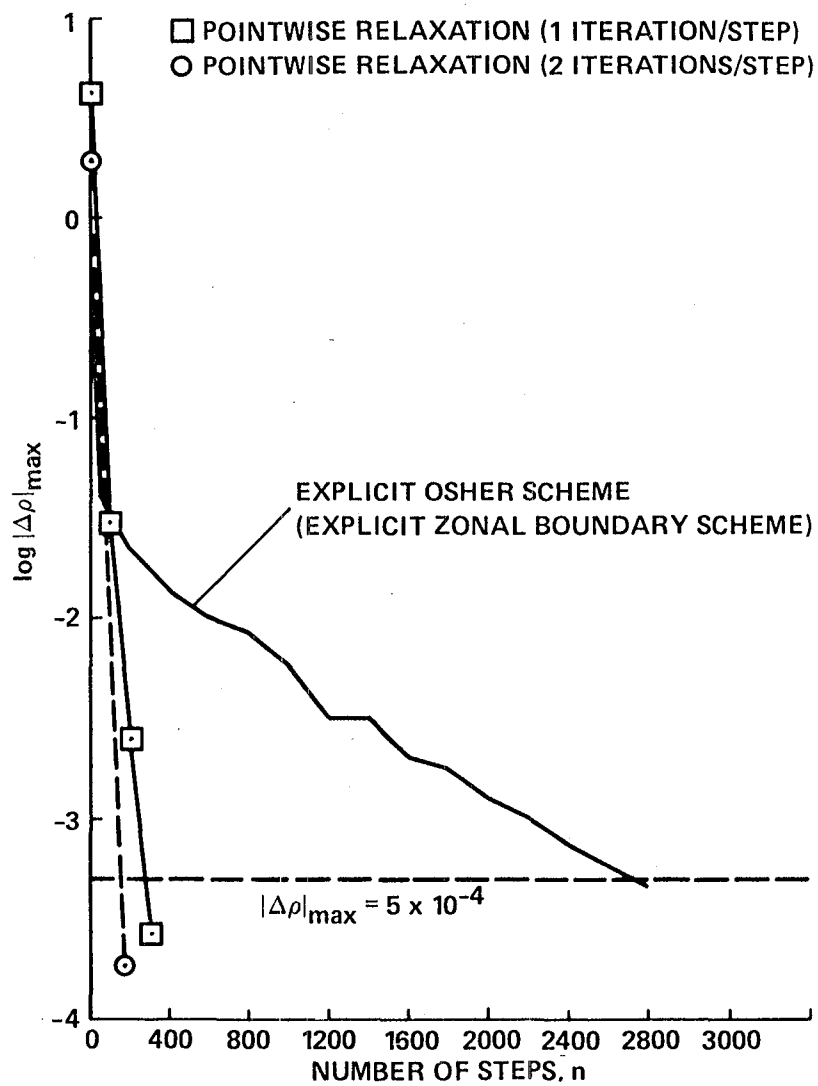


Figure 16.- Convergence history for the cylinder calculation (first-order explicit and implicit, pointwise relaxation calculations).

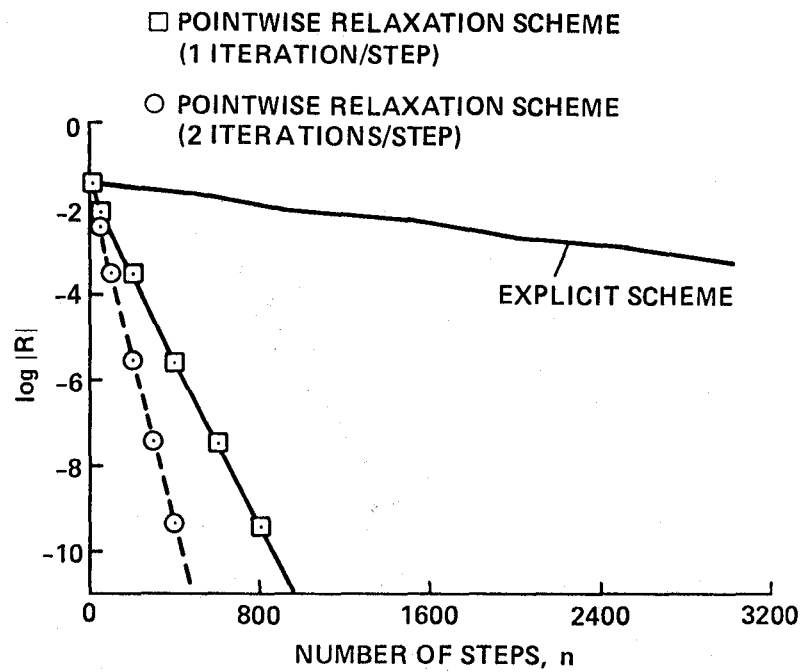


Figure 17.- Time-history of the maximum residual in the continuity equation (explicit and relaxation schemes).

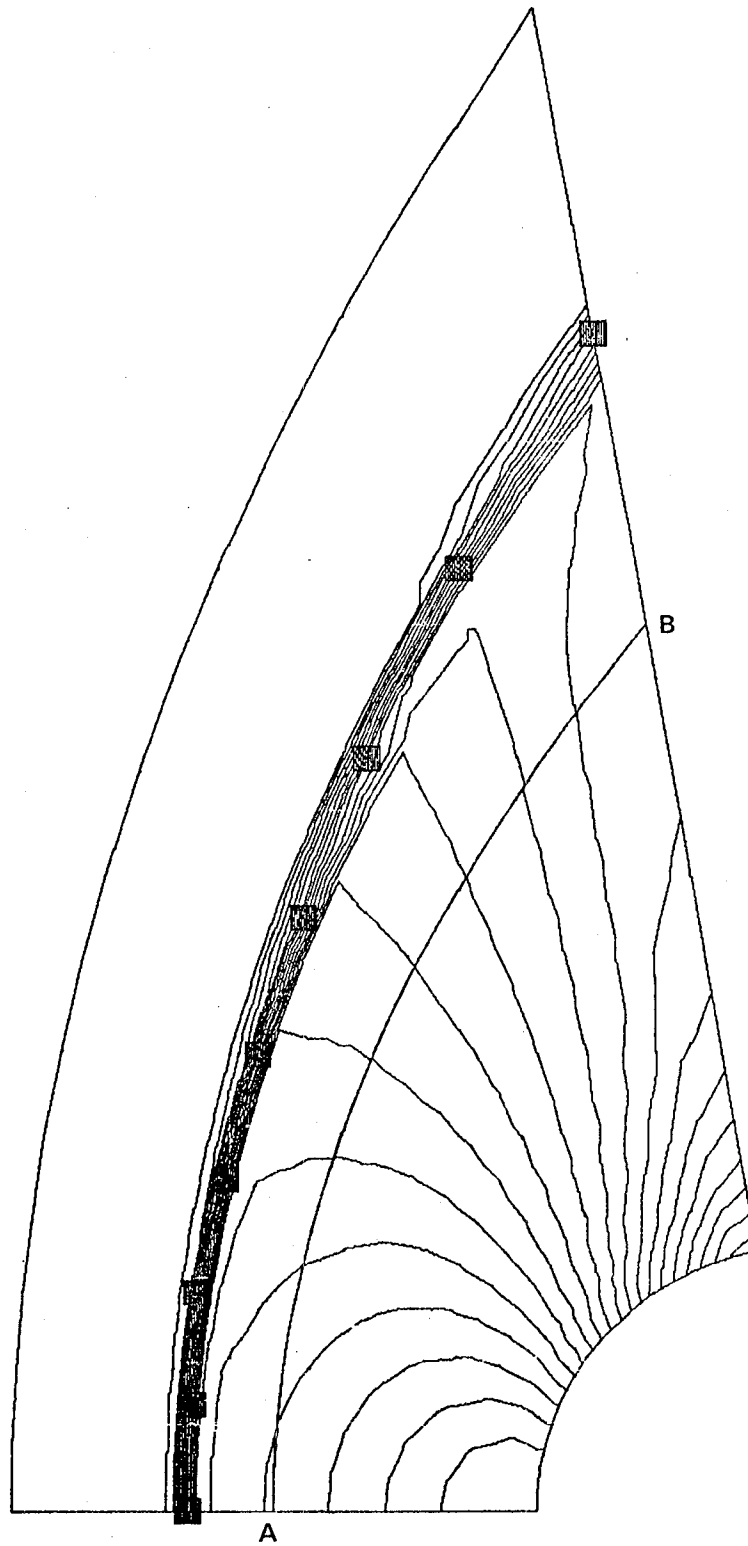


Figure 18.- Isobars at convergence (second-order relaxation scheme).

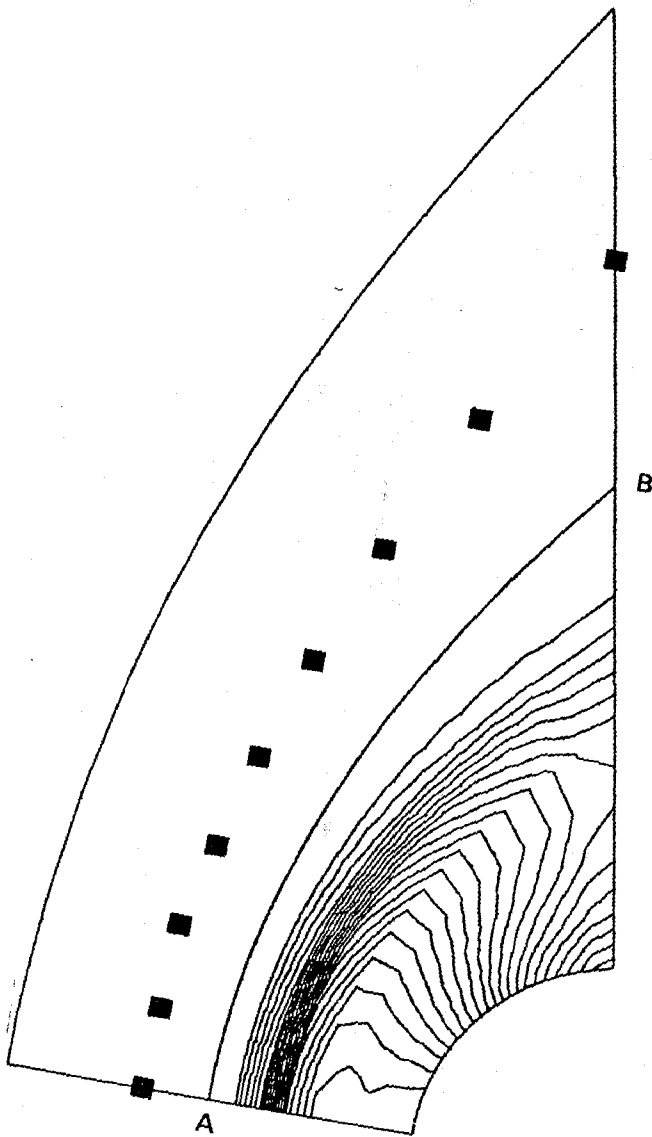


Figure 19.- Isobars after 13
integration steps (first-order
factored, implicit scheme).

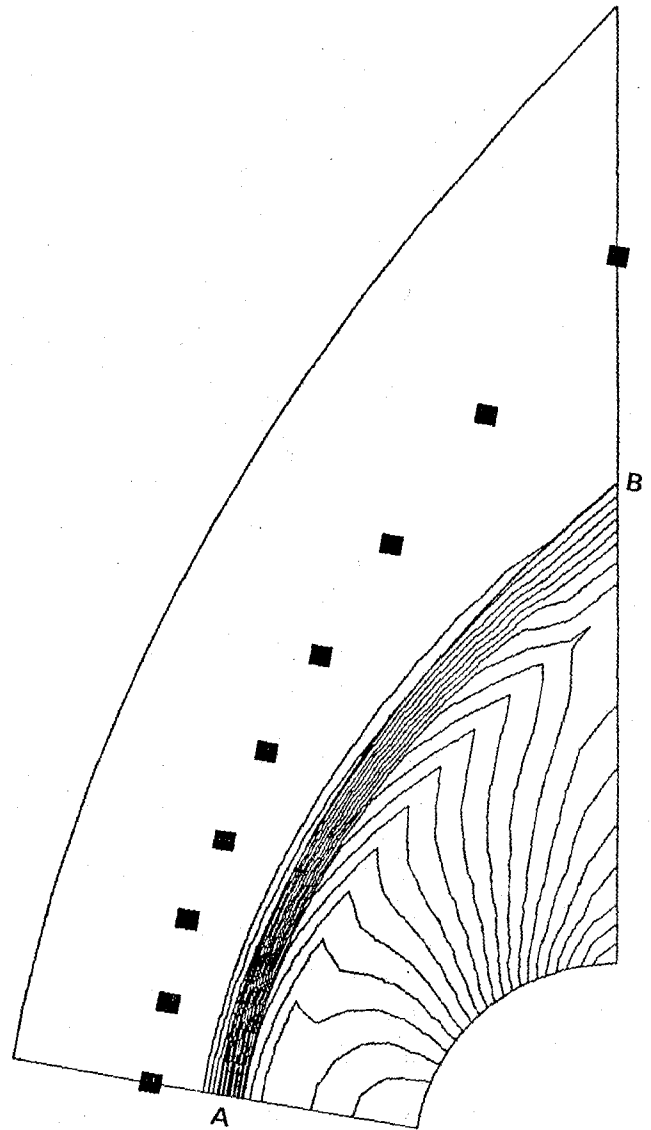


Figure 20.- Isobars after 19
integration steps (first-order
factored, implicit scheme).

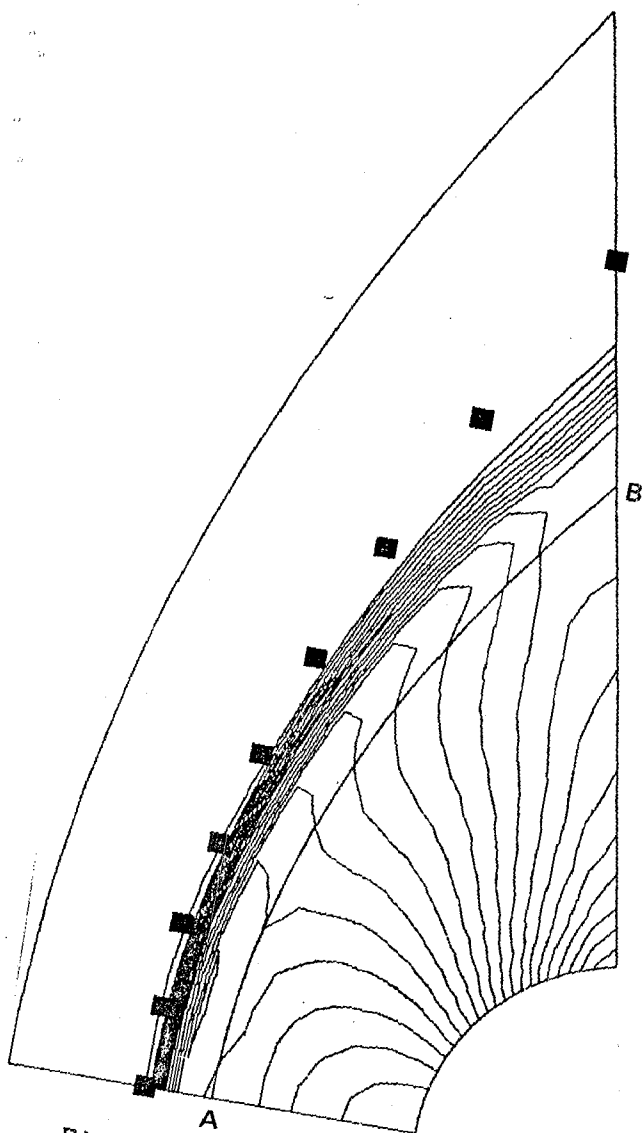


Figure 21.- Isobars after 24 integration steps (first-order factored, implicit scheme).

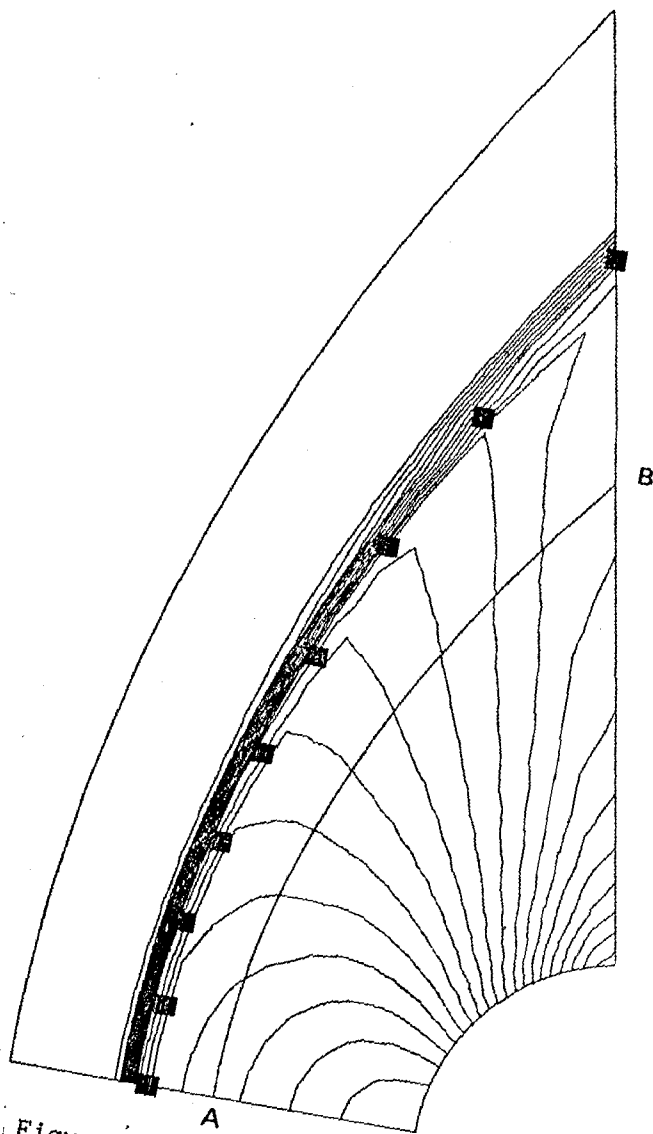


Figure 22.- Isobars at convergence (first-order factored, implicit scheme).

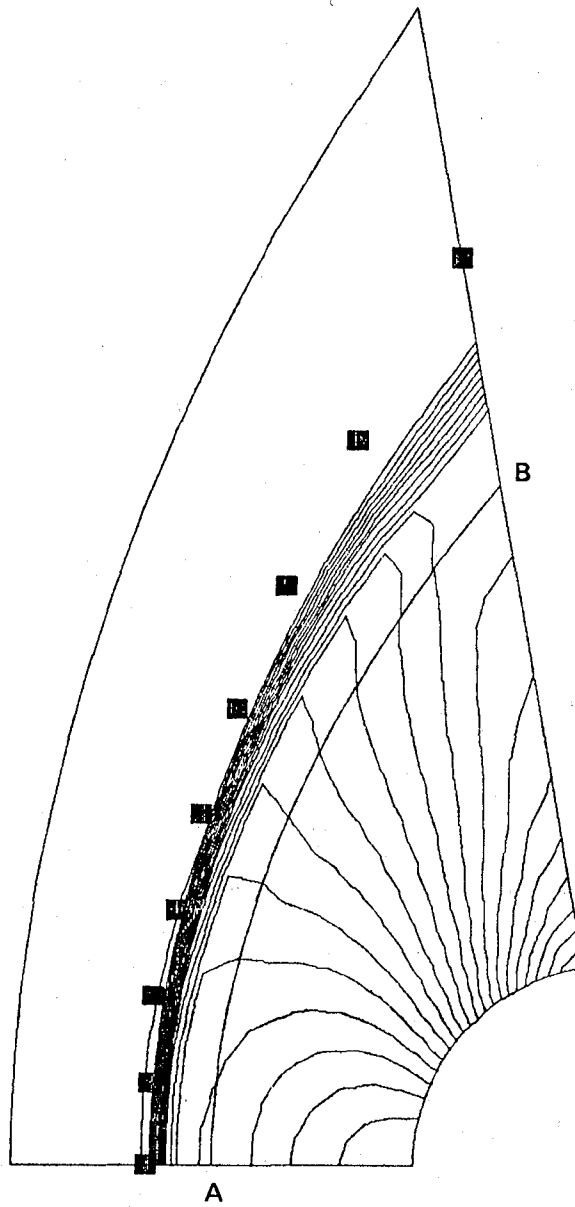


Figure 23.- Isobars after 24 integration steps (first-order factored, implicit scheme and five iterations/step).

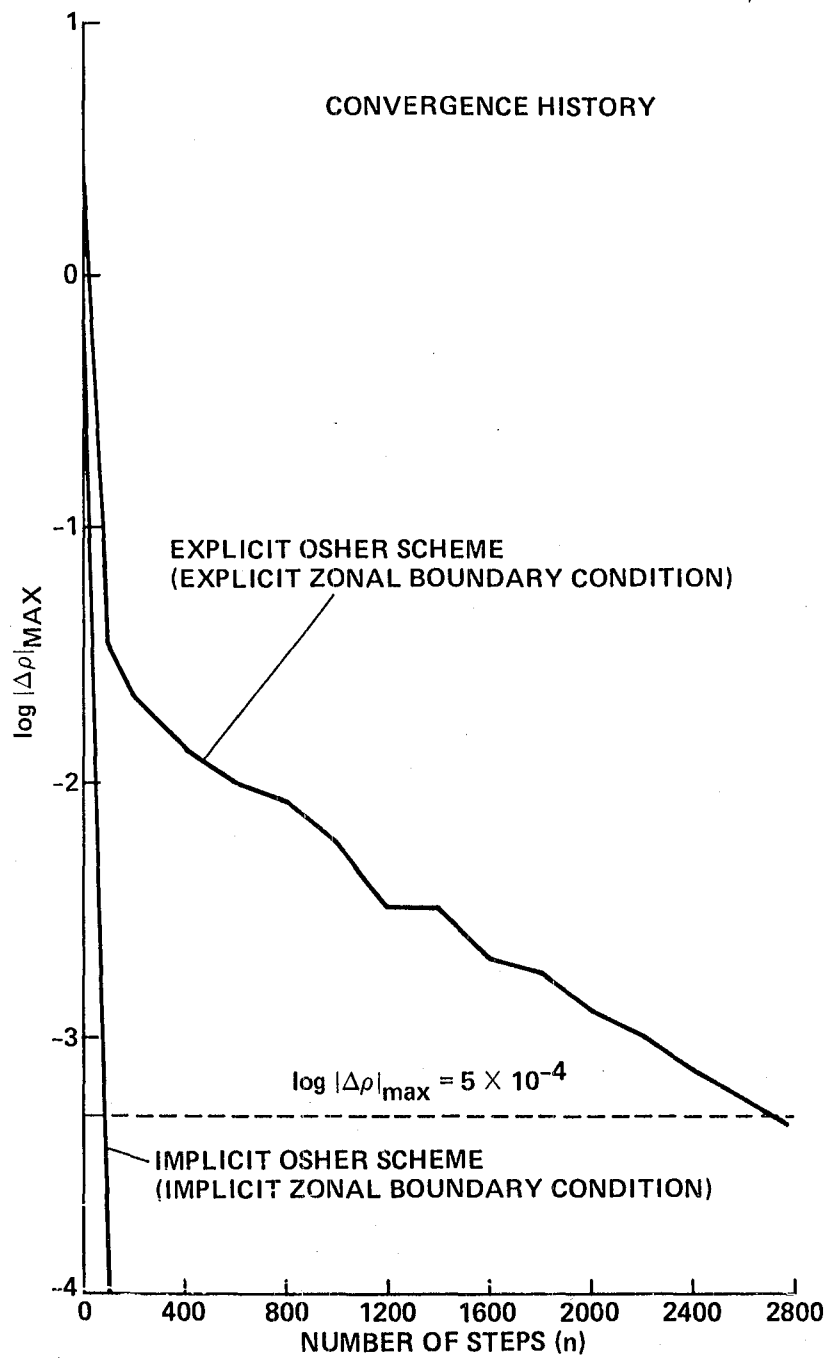


Figure 24.- Convergence history for the cylinder calculation (first-order explicit and factored, implicit calculations).

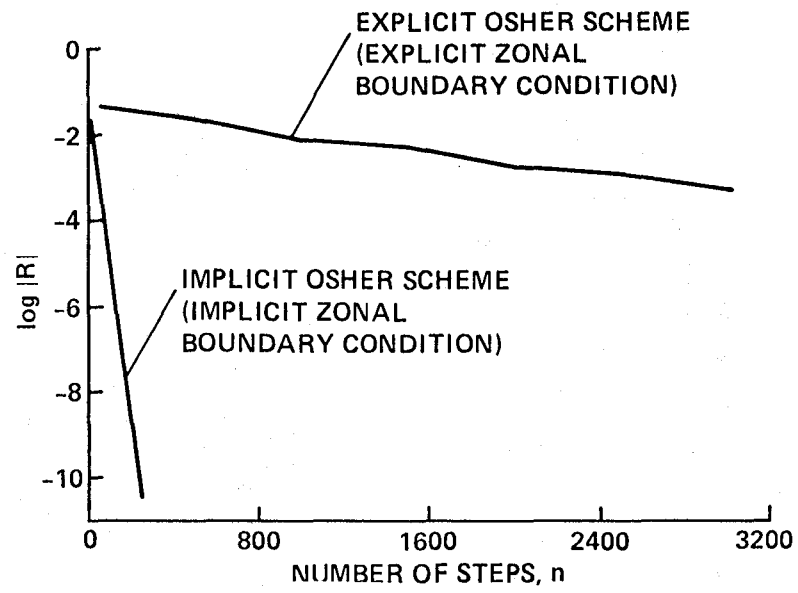


Figure 25.- Time history of the maximum residual in the continuity equation (explicit and factored, implicit schemes).

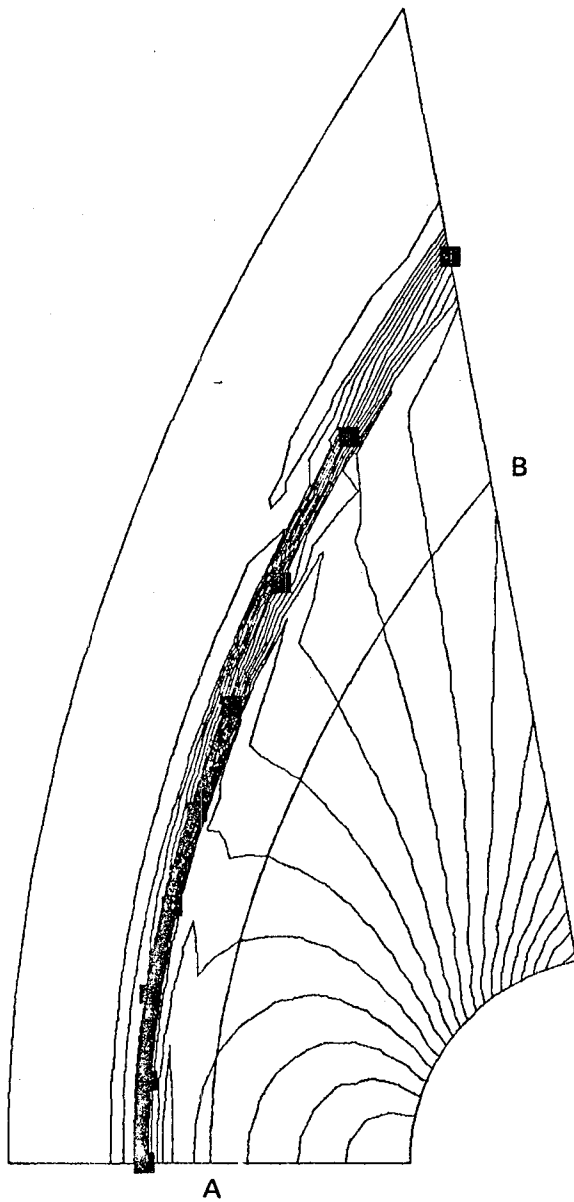


Figure 26.- Isobars at convergence
(second-order factored, implicit
scheme).

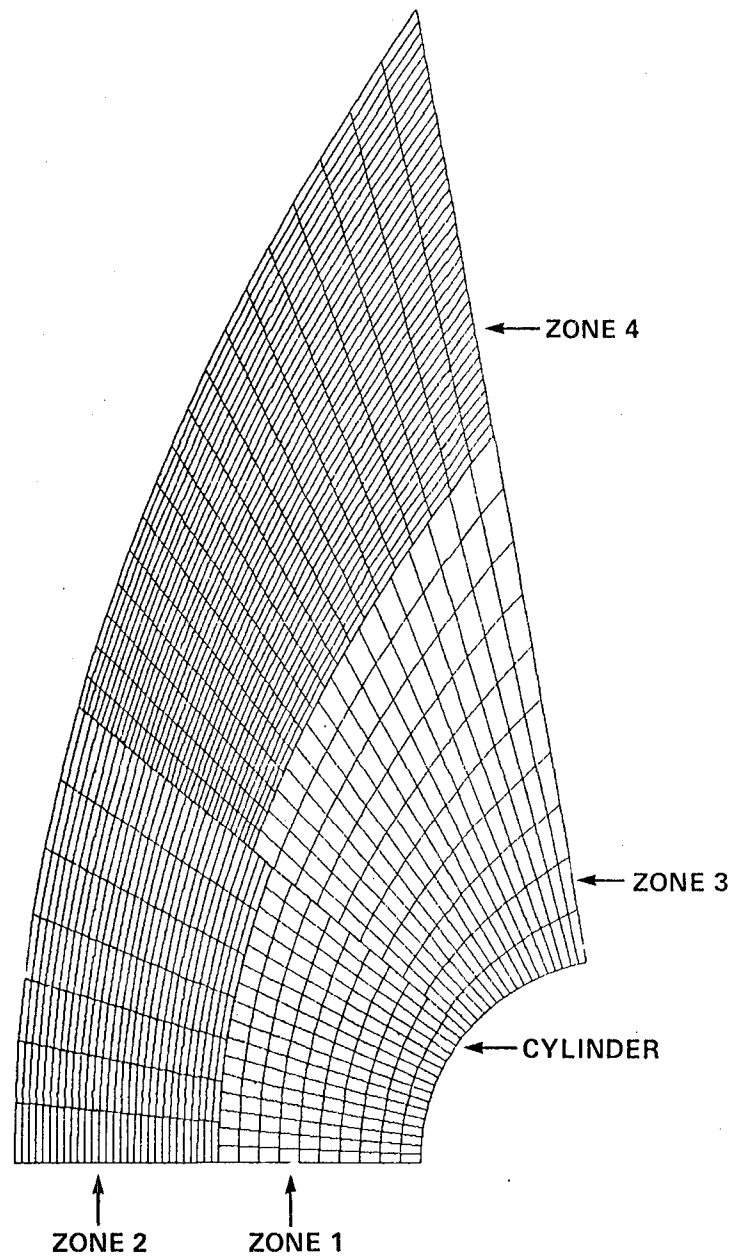


Figure 27.- Grid for four-patch
cylinder calculation.

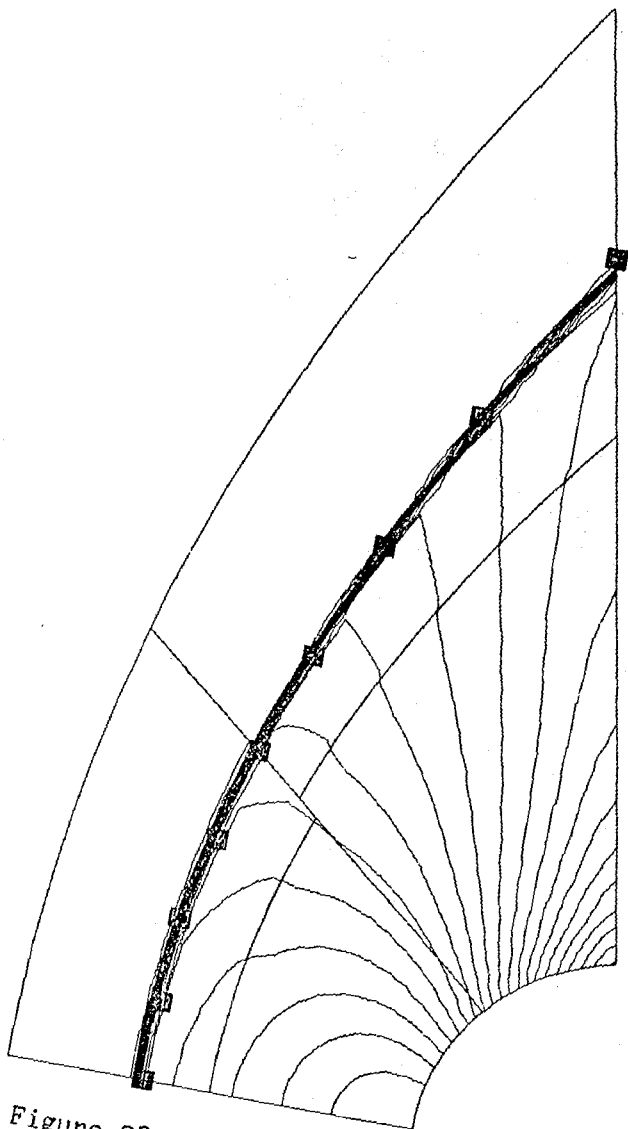


Figure 28.- Isobars at convergence
(first-order, factored implicit
scheme).

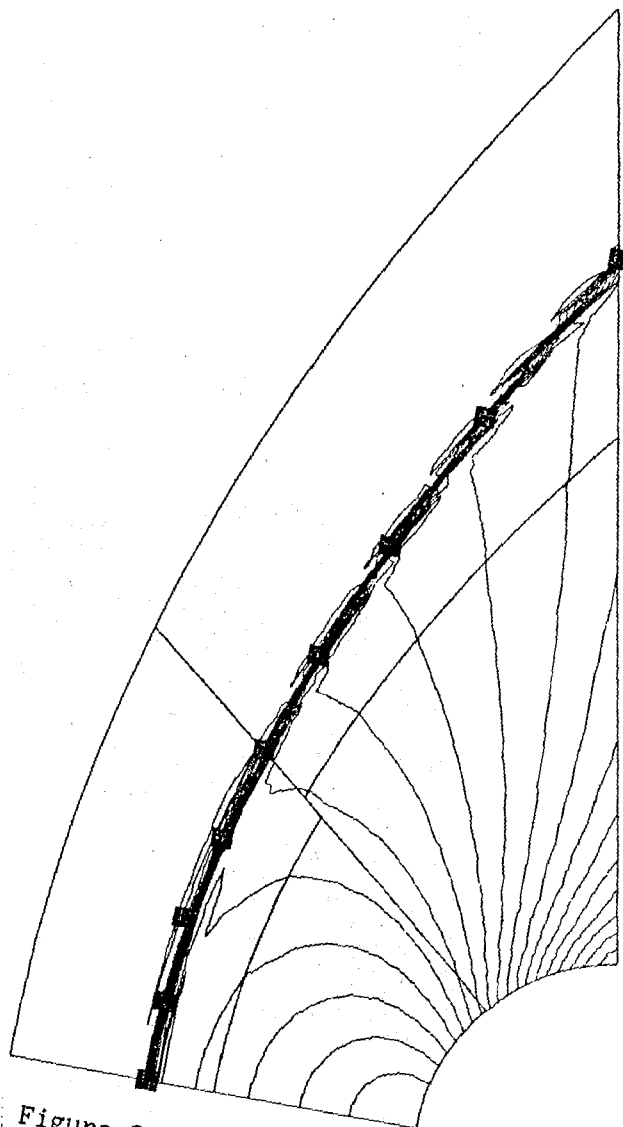


Figure 29.- Isobars at convergence
(second-order, factored implicit
scheme).

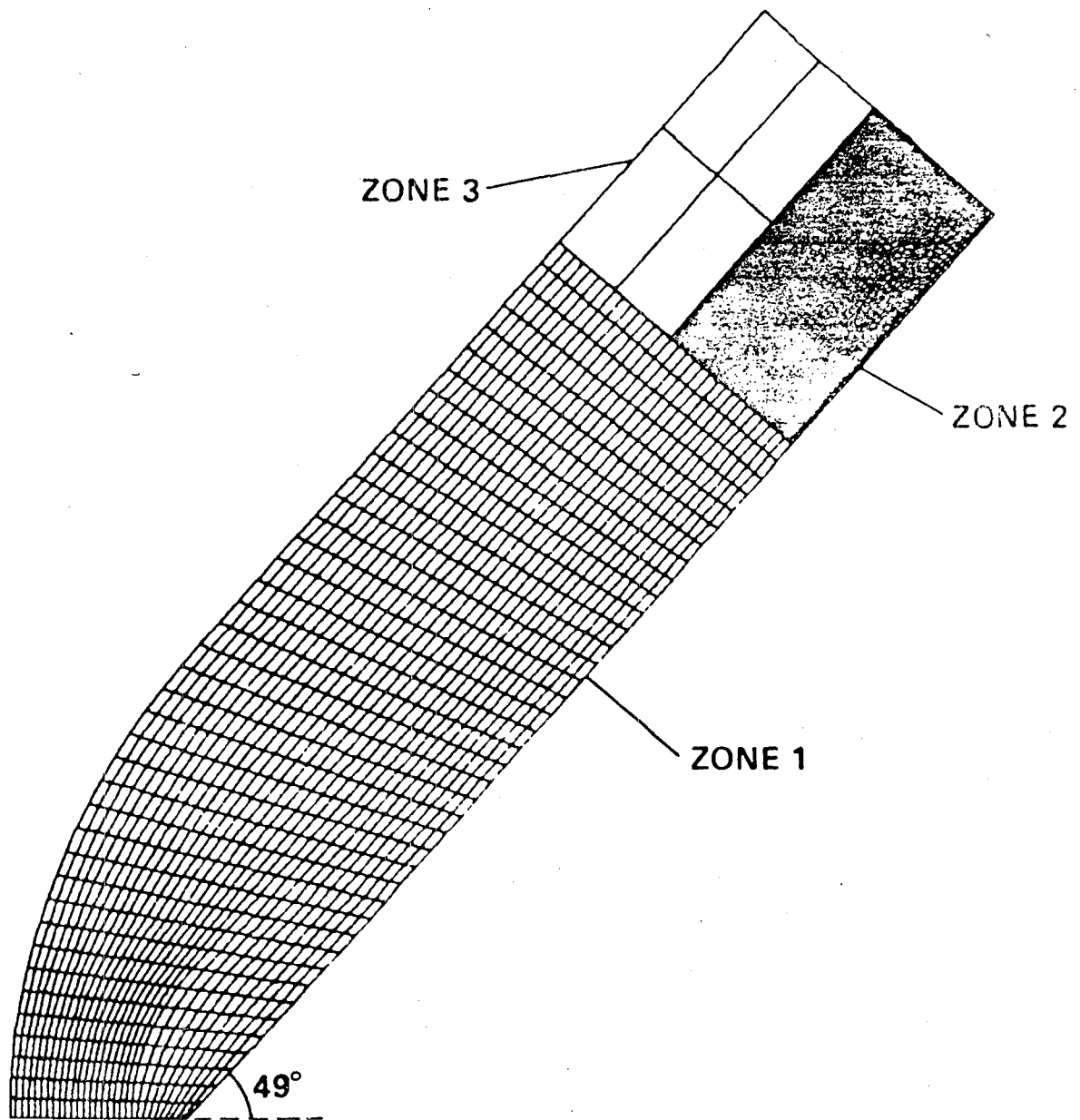


Figure 30.- Grid for three-patch blast wave calculation.

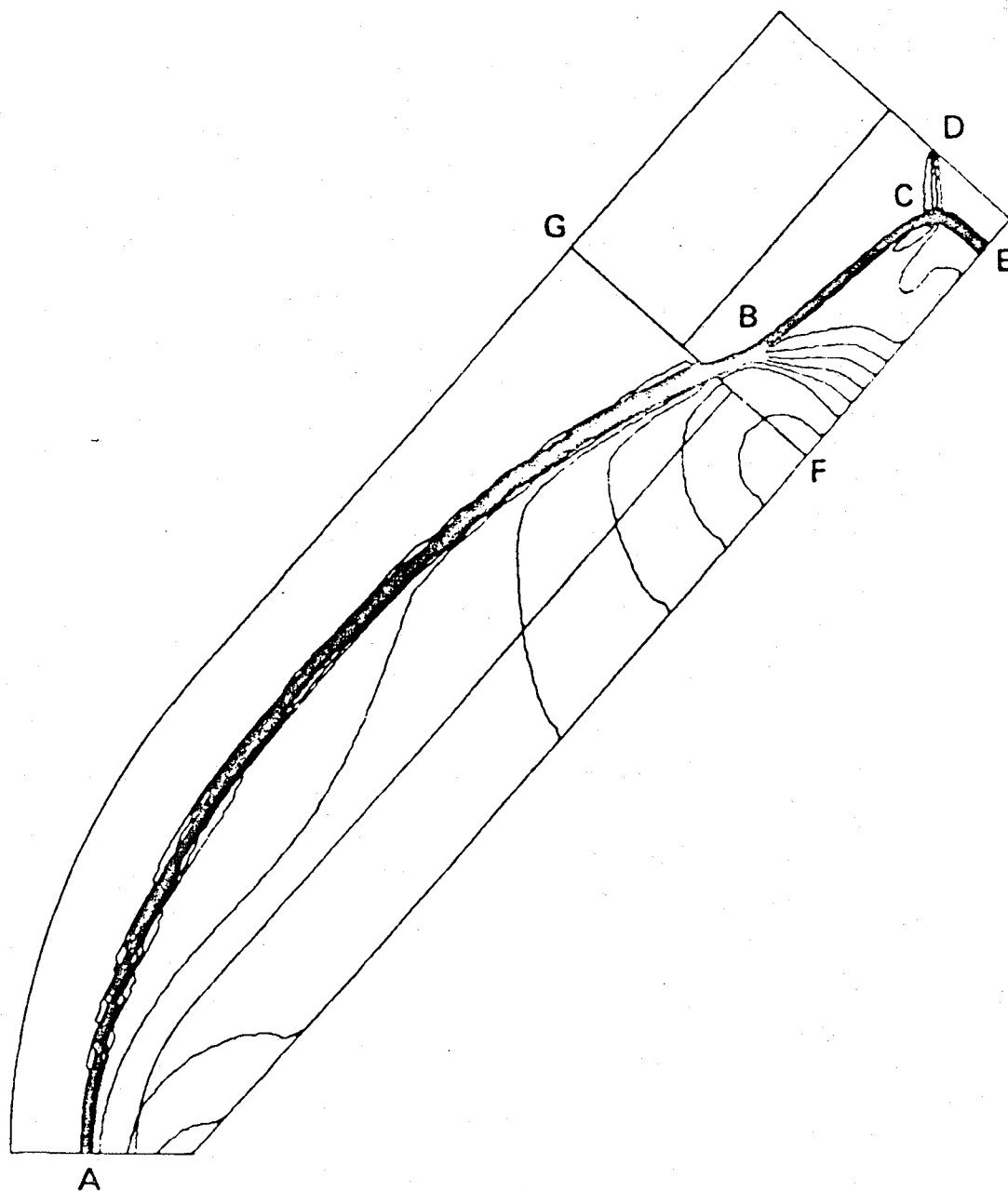


Figure 31.- Isobars obtained at convergence for the blast wave problem.

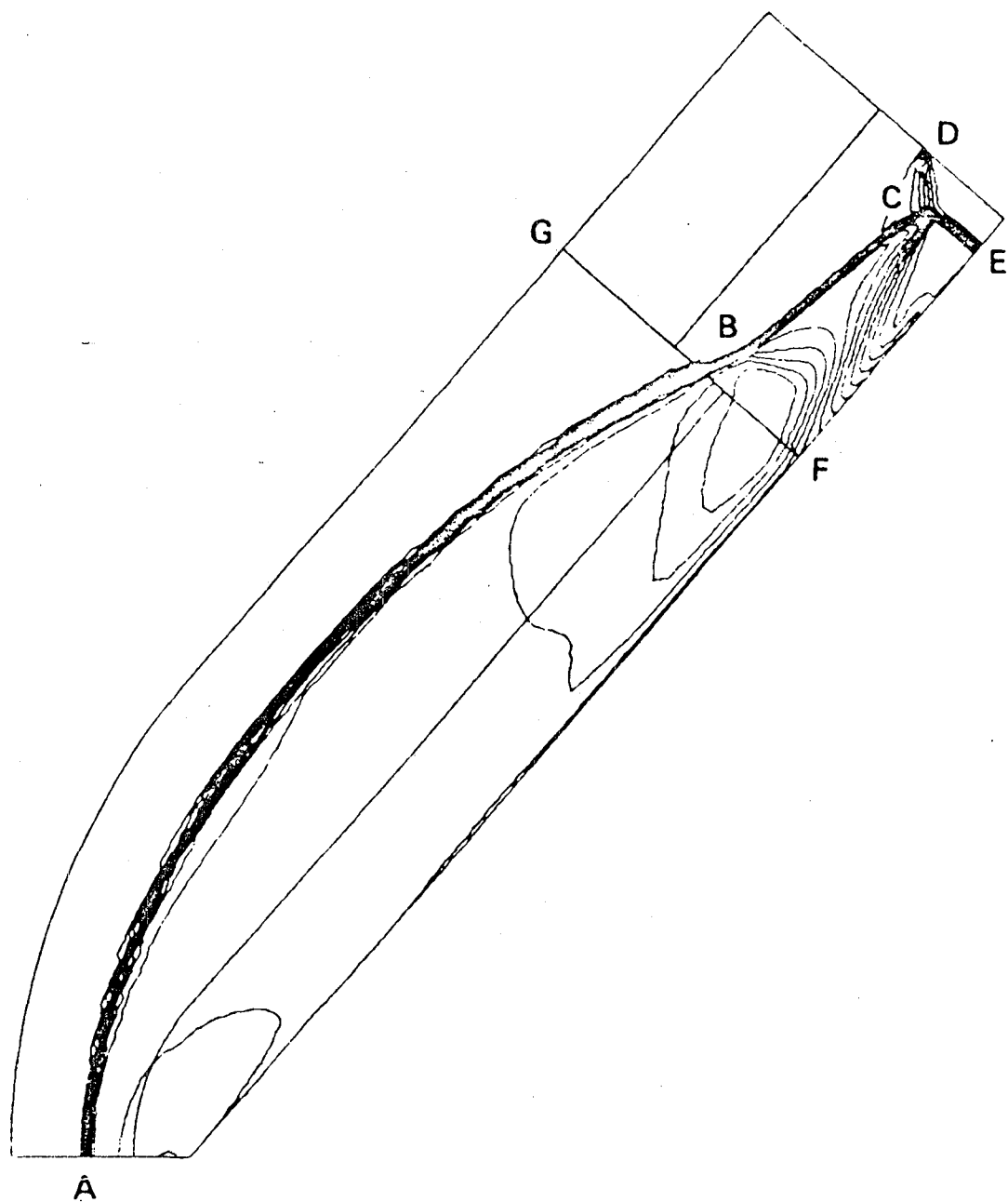


Figure 32.- Isopycnics obtained at convergence for the blast wave problem.

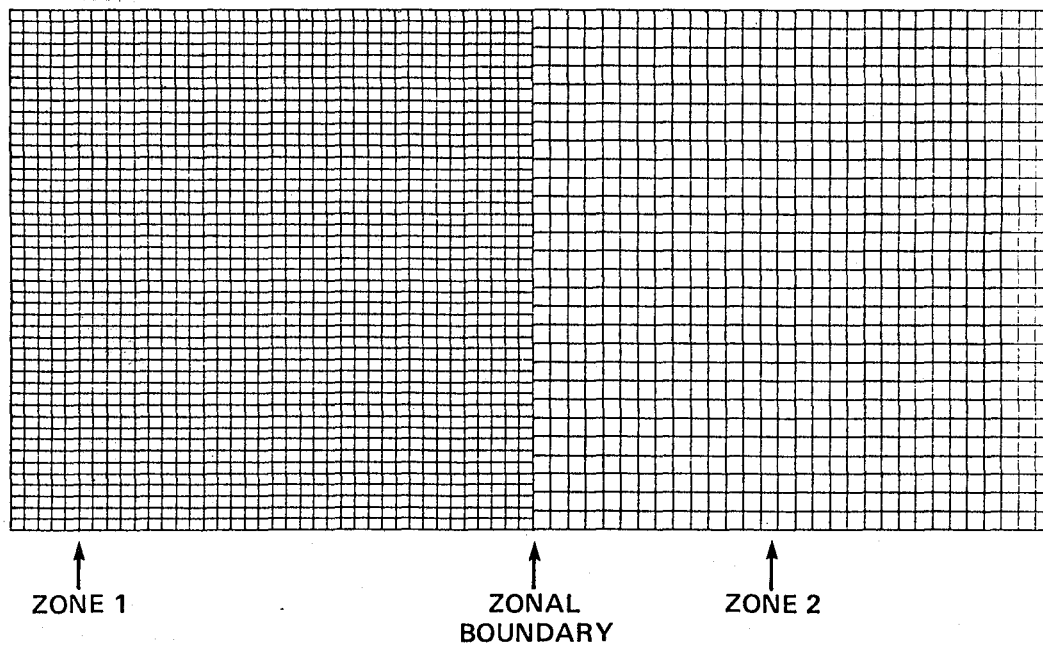


Figure 33.- Grid for two-patch vortex calculation.

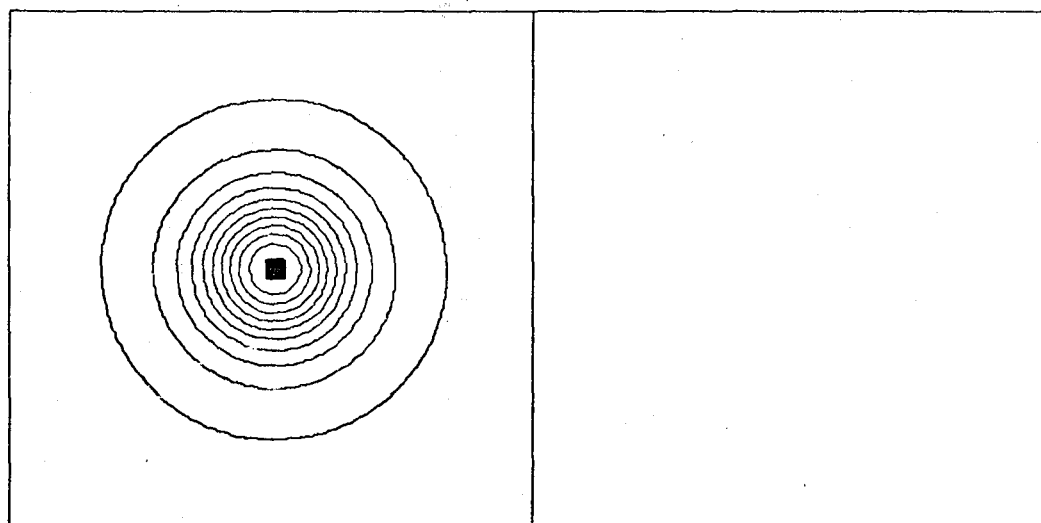


Figure 34.- Isobars for the vortex calculation (at initialization).

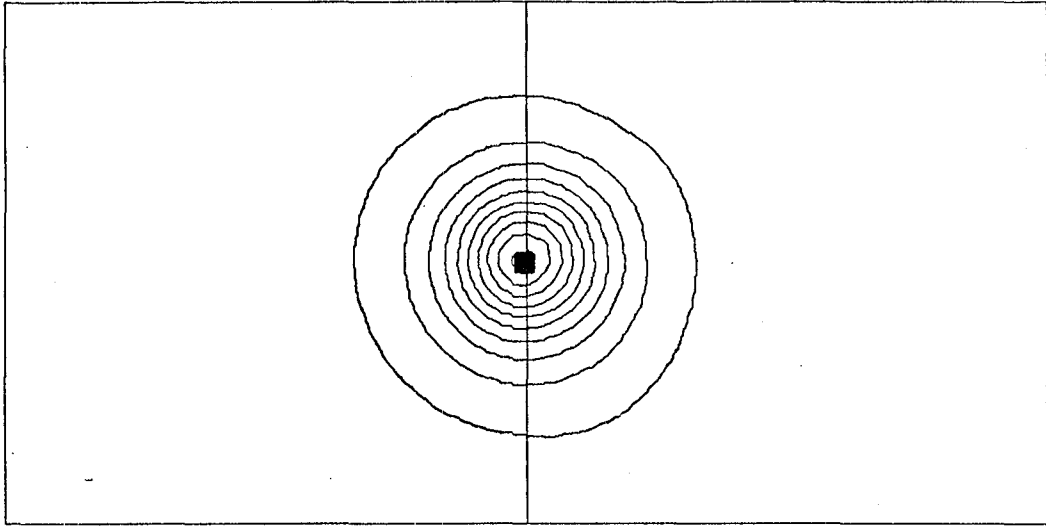


Figure 35.- Isobars for the vortex calculation (after 85 steps).

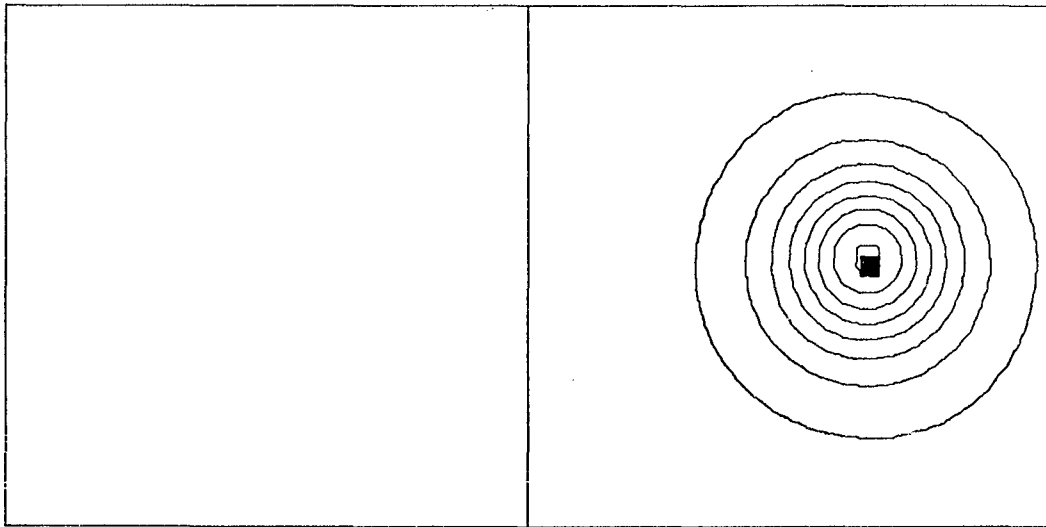


Figure 36.- Isobars for the vortex calculation (after 180 steps).

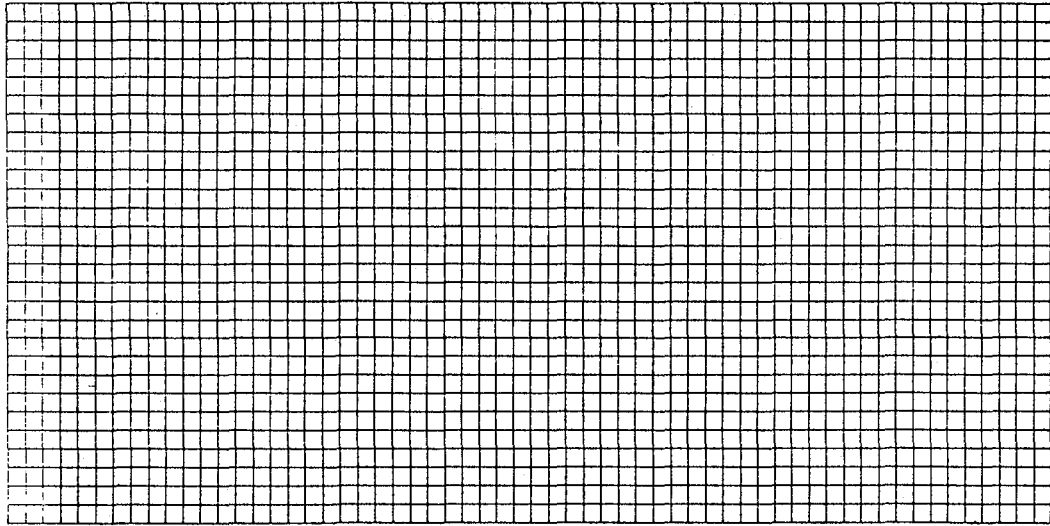


Figure 37.- Grid for single-patch vortex calculation.

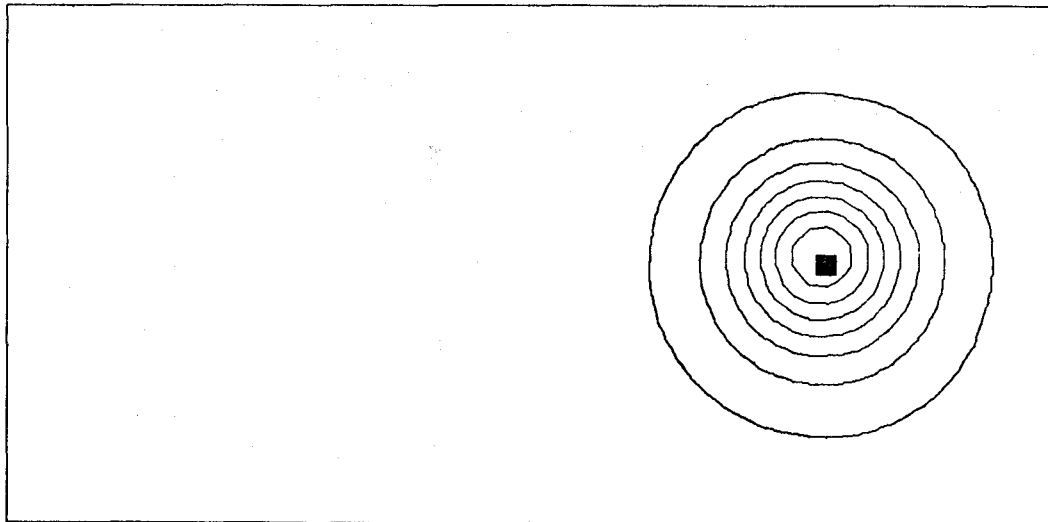


Figure 38.- Isobars for the vortex calculation (after 140 steps).

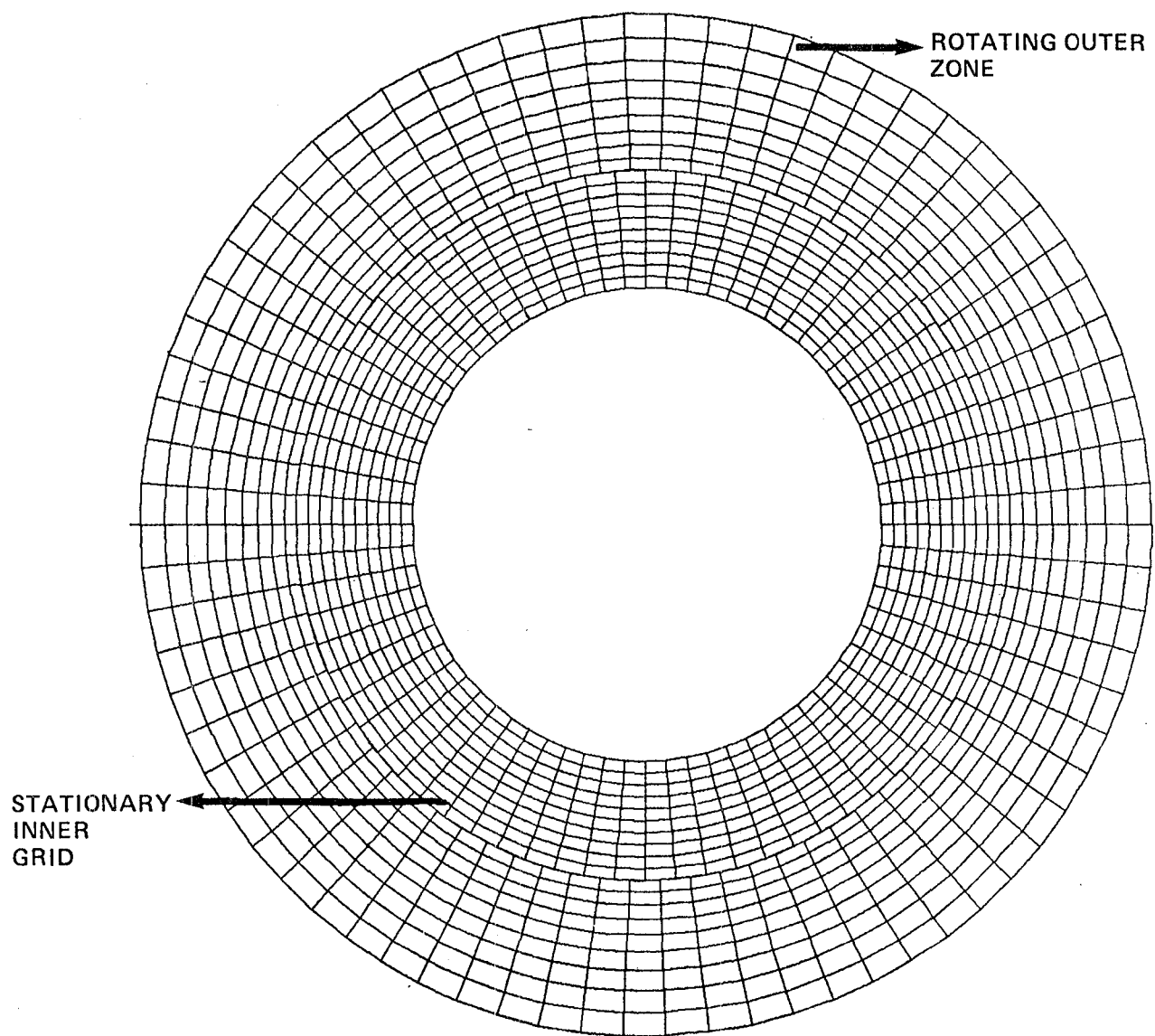


Figure 39.- Grid for two-patch cylinder (subsonic) calculation.

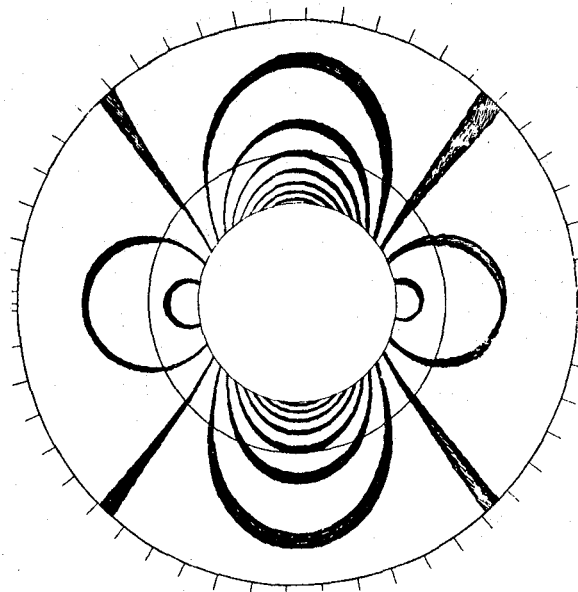


Figure 40.- Isobars at each step as the outer grid performs one rotation.

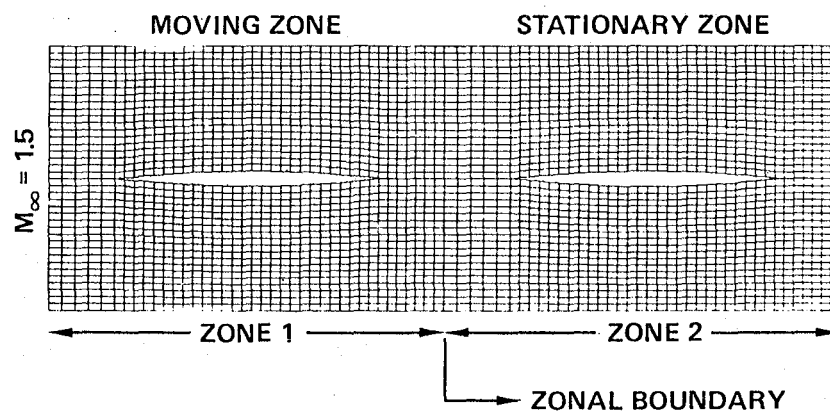


Figure 41.- Two-patch grid for the double-airfoil calculation.

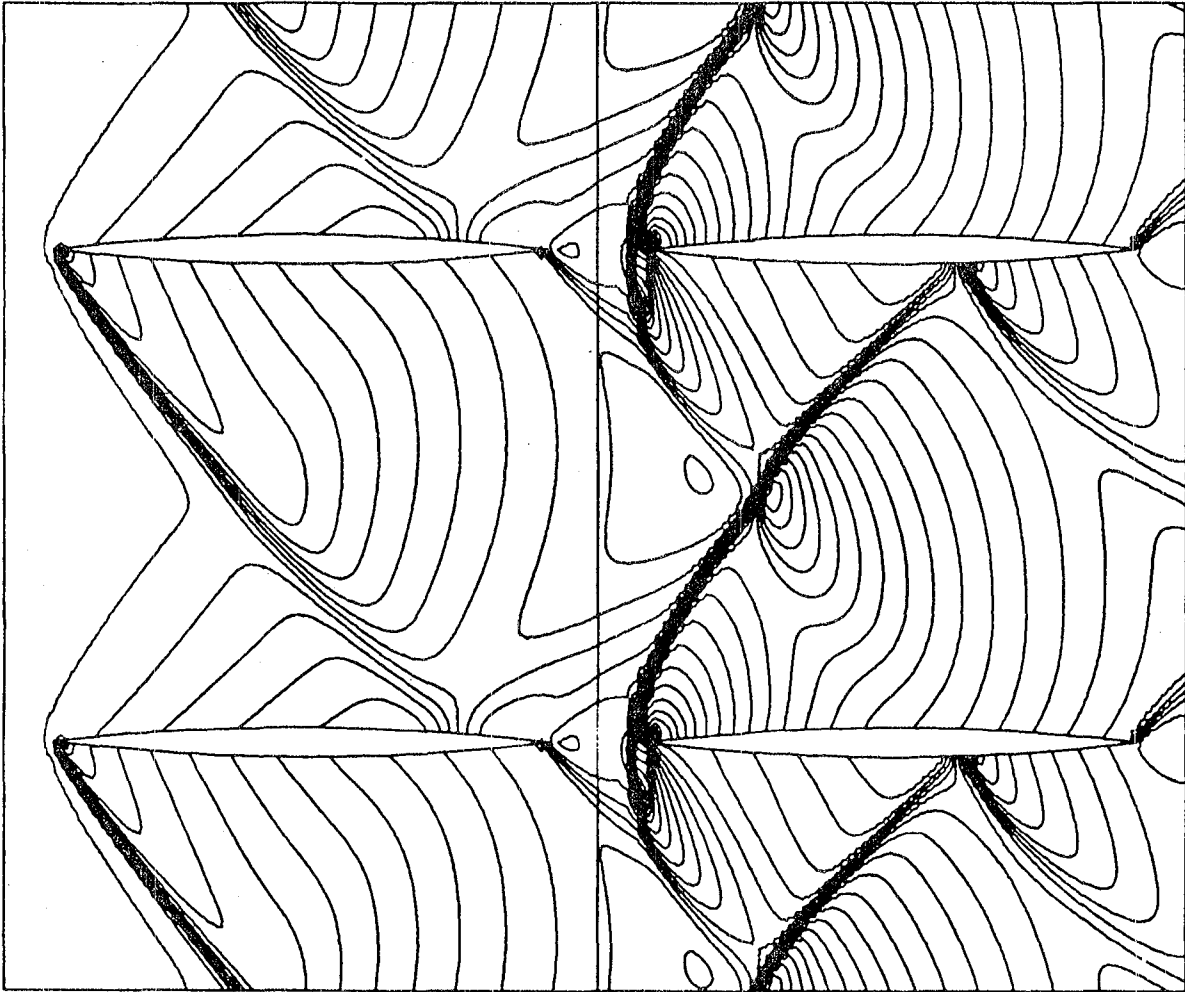


Figure 42.- Pressure contours after 4.0 cycles.



Figure 43.- Pressure contours after 4.2 cycles.

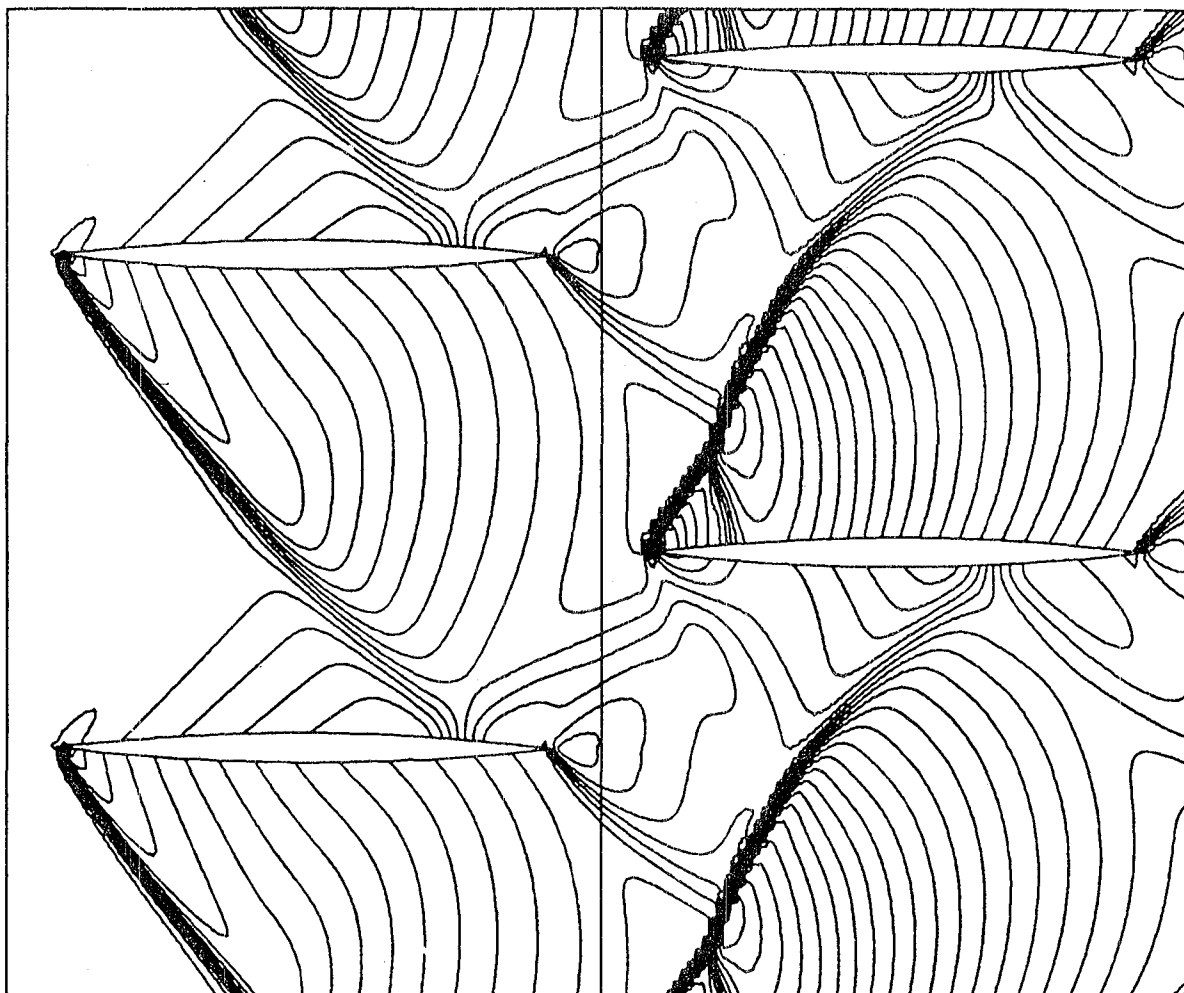


Figure 44.- Pressure contours after 4.4 cycles.

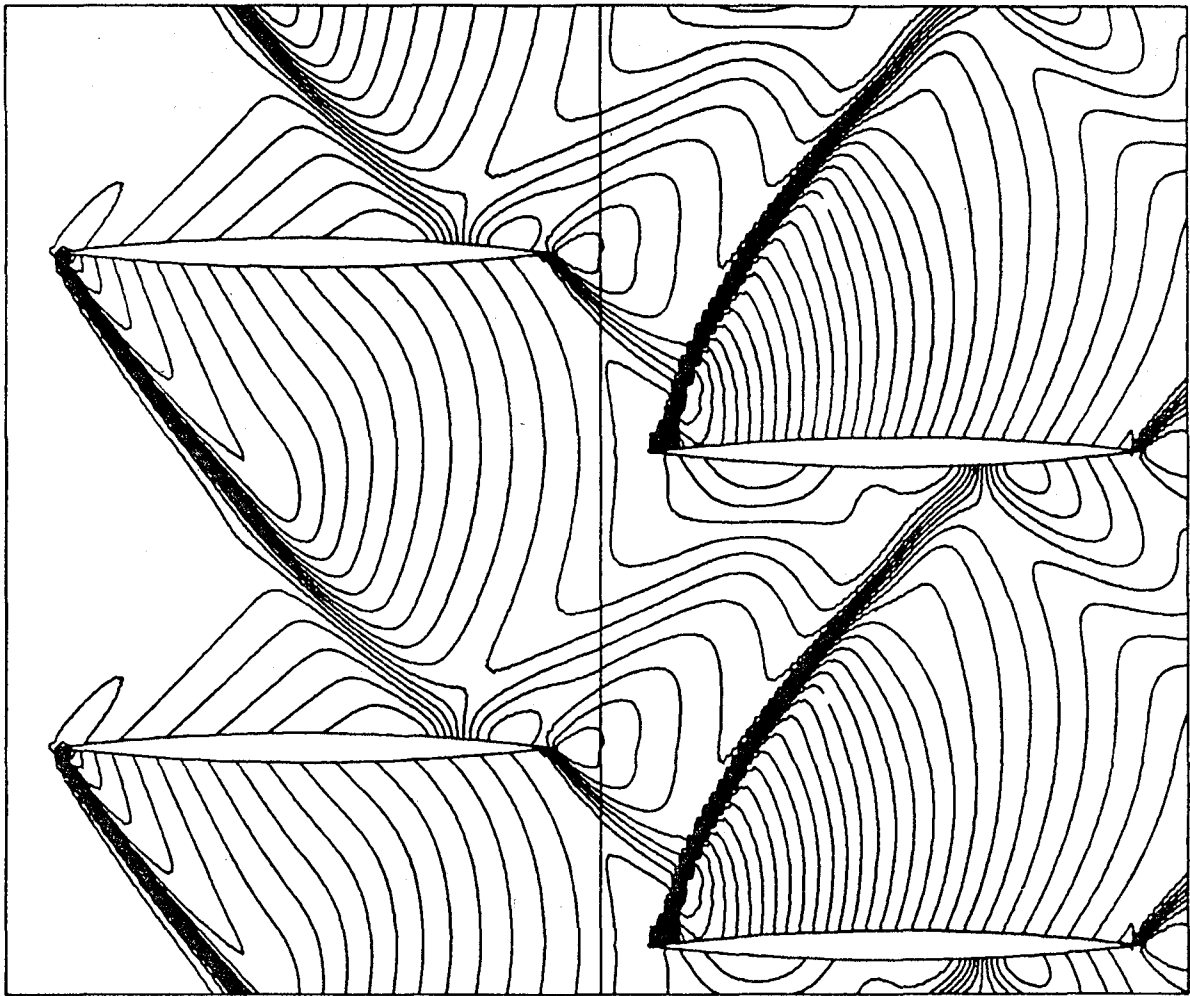


Figure 45.- Pressure contours after 4.6 cycles.

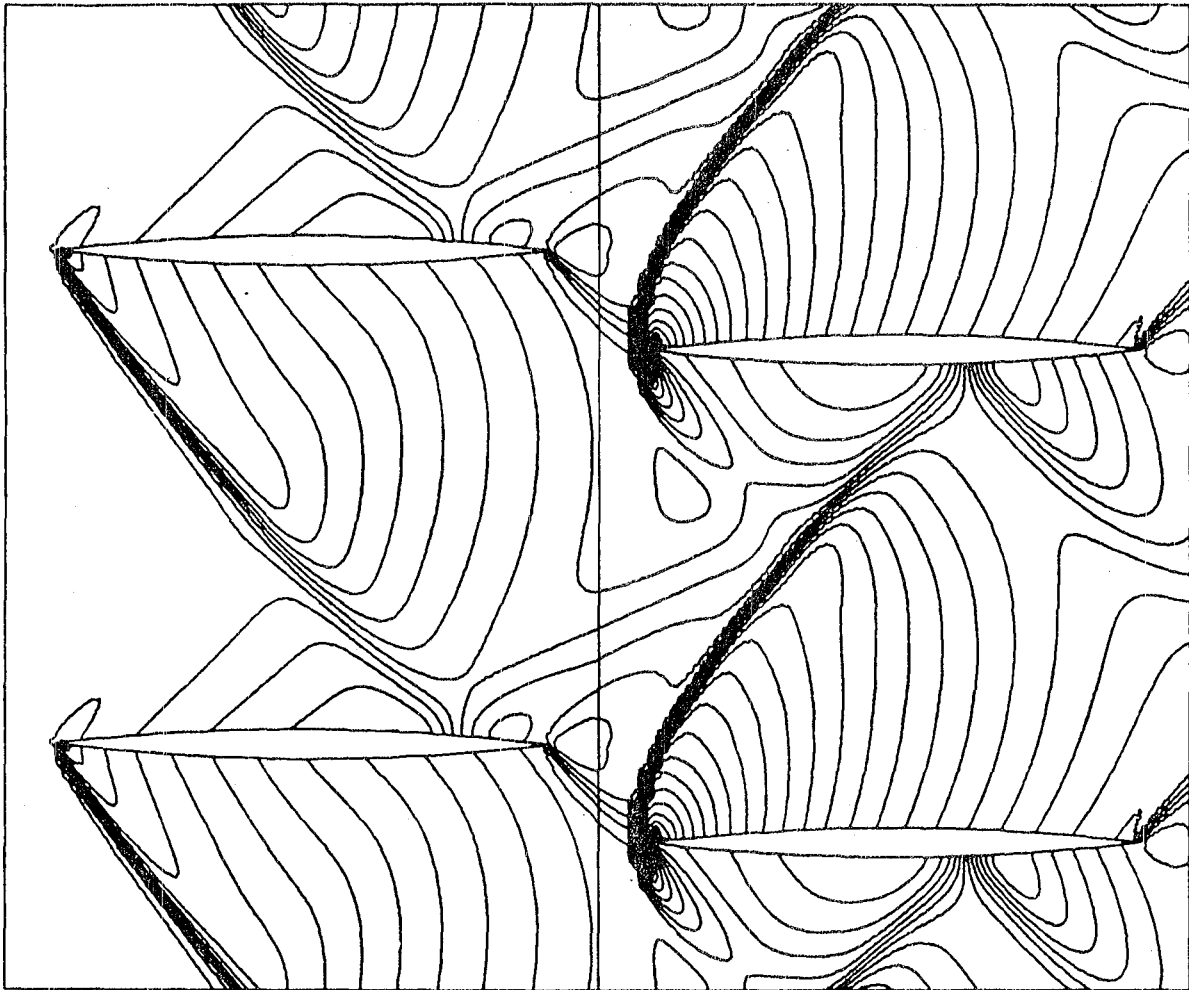


Figure 46.- Pressure contours after 4.8 cycles.

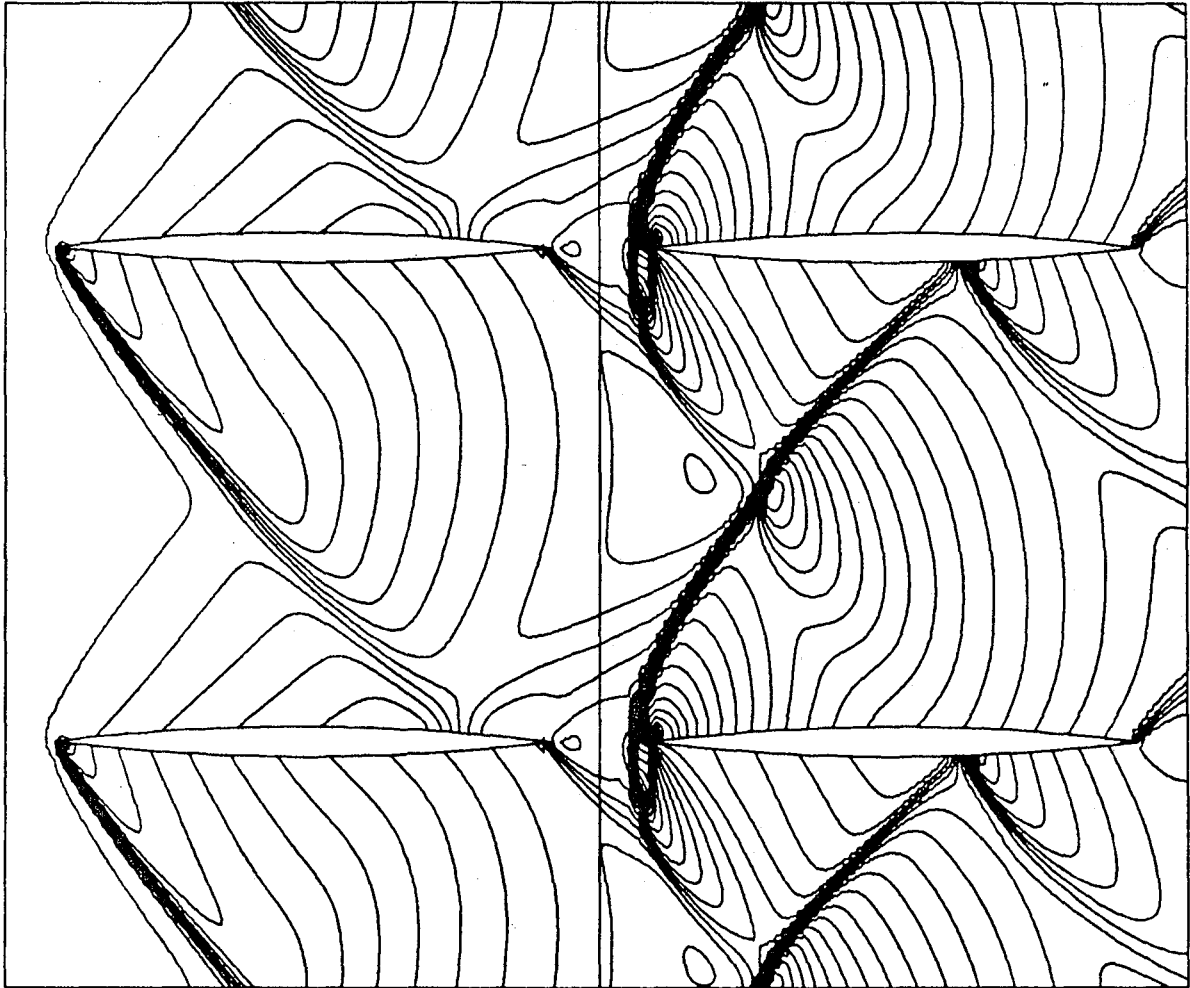


Figure 47.- Pressure contours after 5.0 cycles.

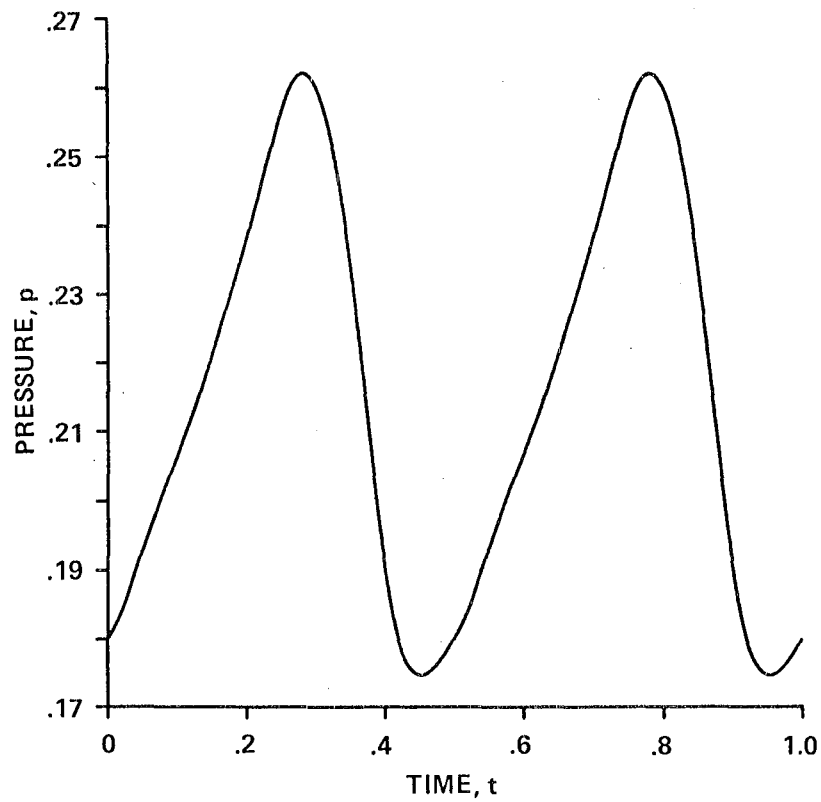


Figure 48.- Pressure history at midchord on the lower surface of the aft airfoil.

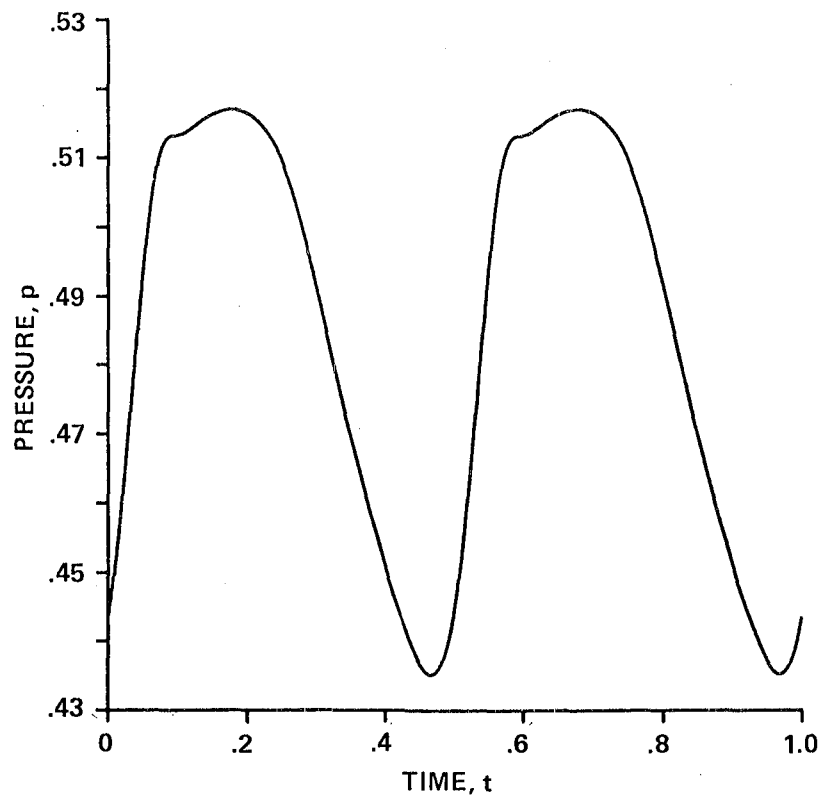


Figure 49.- Pressure history at midchord on the upper surface of the aft airfoil.

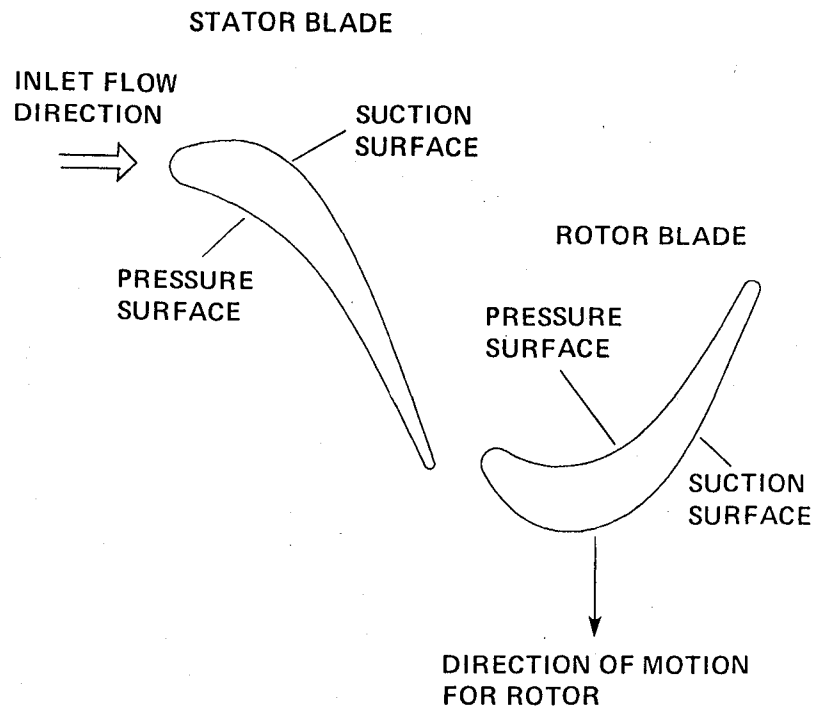


Figure 50.- Rotor-stator geometry of Dring et al. (ref. 30).

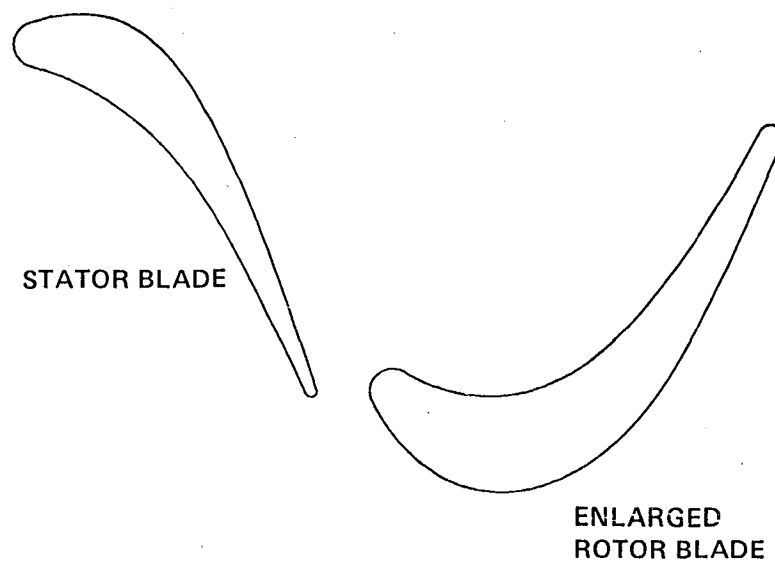


Figure 51.- Modified rotor-stator geometry.

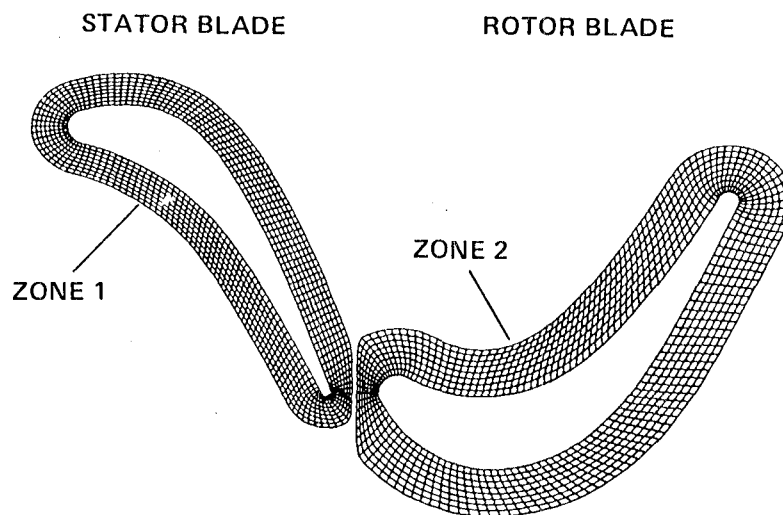


Figure 52.- "O" type grids for regions 1 and 2.

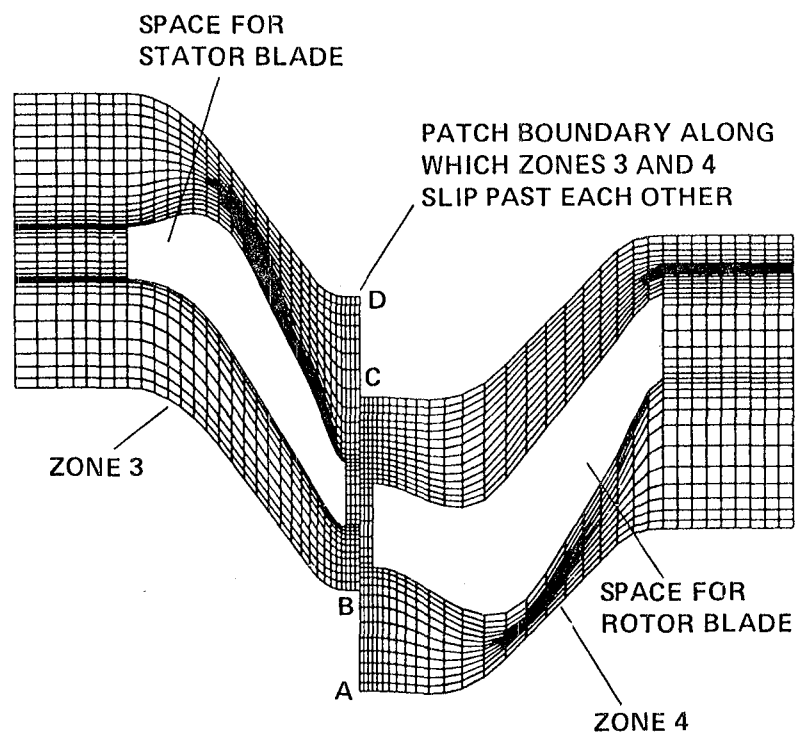


Figure 53.- Algebraically generated grids for regions 3 and 4.

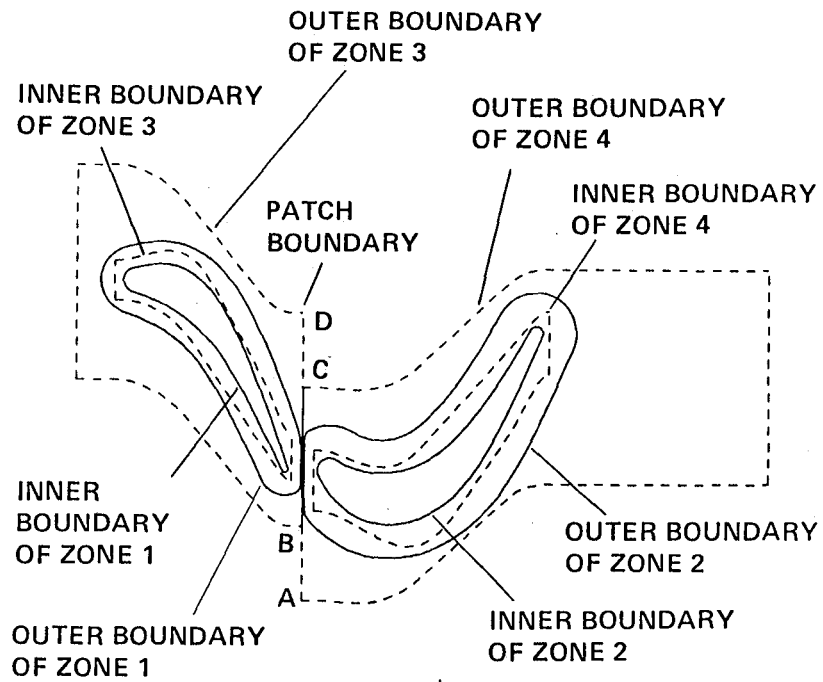


Figure 54.- Zoning of the rotor-stator problem showing patch and overlap boundaries.

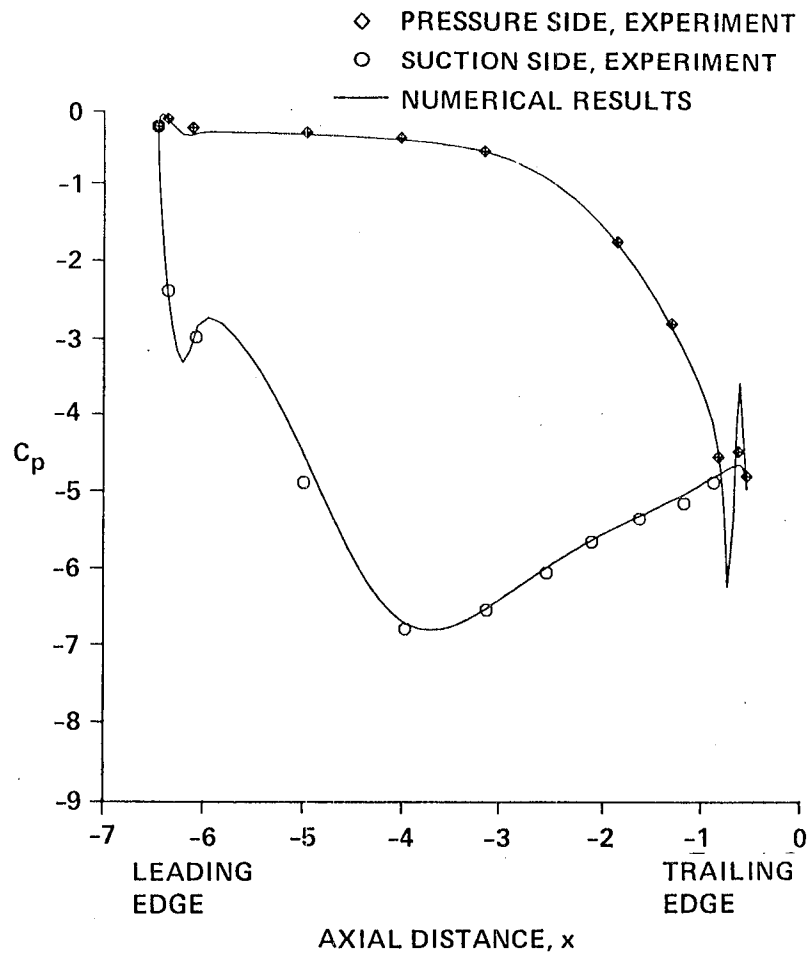


Figure 55.- Time-averaged pressure distribution on the stator.

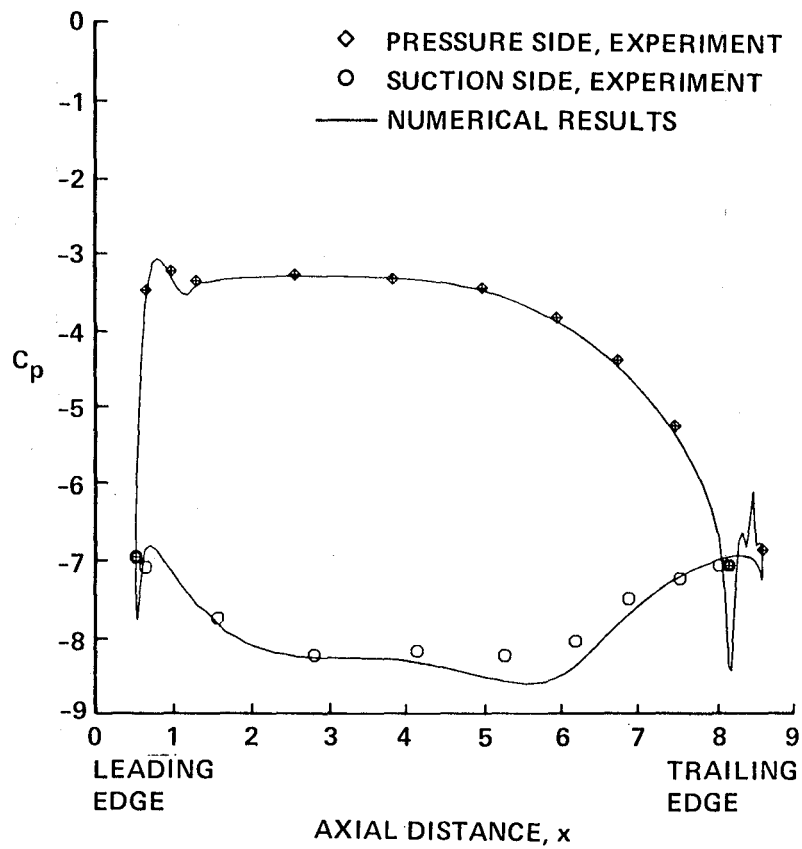


Figure 56.- Time-averaged pressure distribution on the rotor.

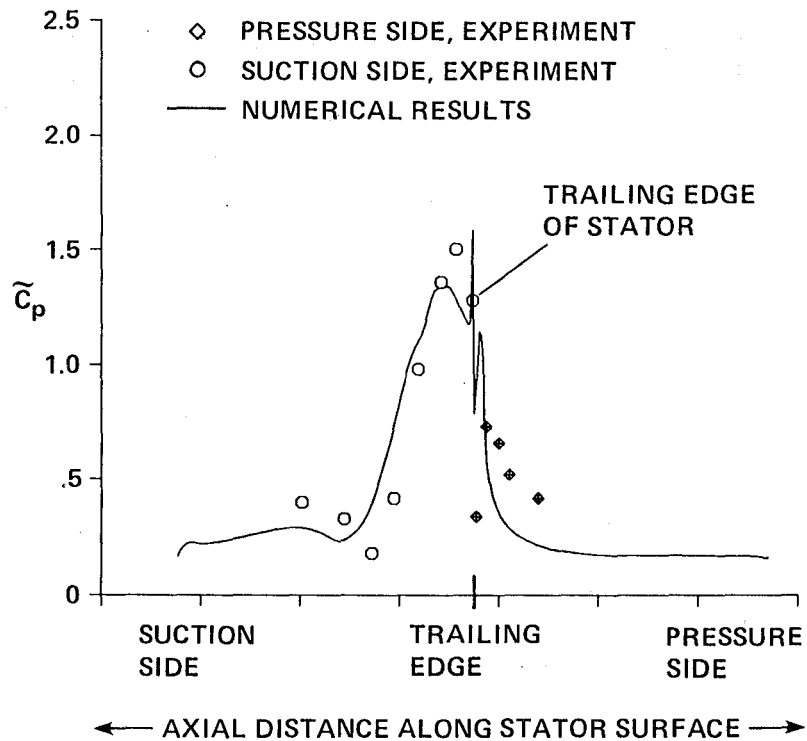


Figure 57.- Pressure-amplitude distribution on the stator.

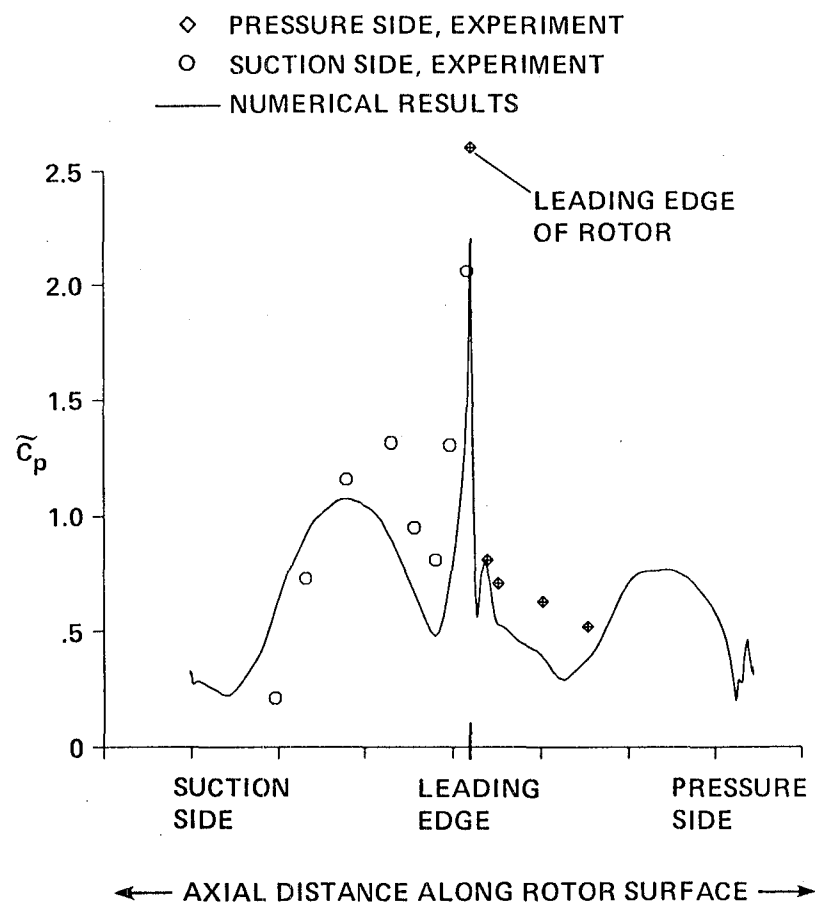
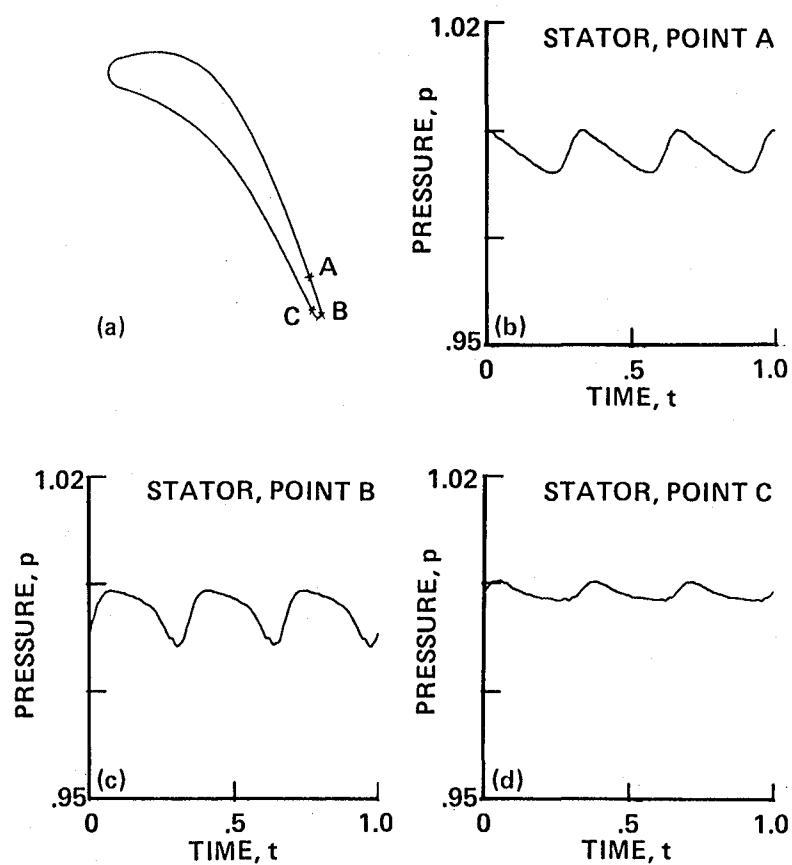


Figure 58.- Pressure-amplitude distribution on the rotor.



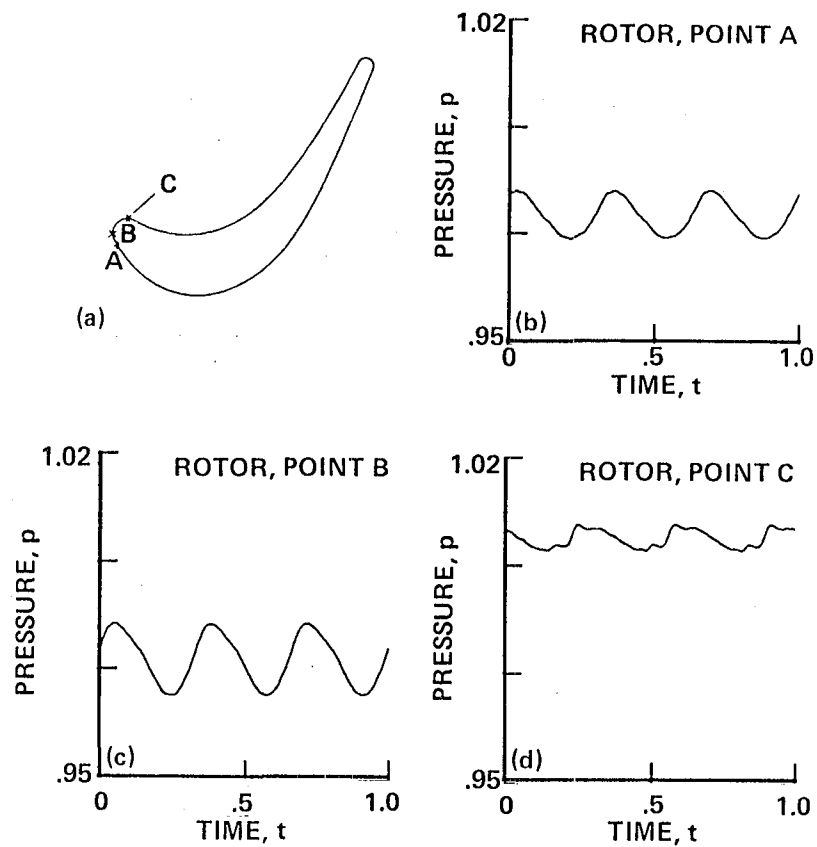
(a) Stator locations at which unsteady pressures were monitored.

(b) Unsteady pressure at point A on the stator.

(c) Unsteady pressure at point B on the stator.

(d) Unsteady pressure at point C on the stator.

Figure 59.- Unsteady pressures on the stator.



(a) Rotor locations at which unsteady pressures were monitored.

(b) Unsteady pressure at point A on the rotor.

(c) Unsteady pressure at point B on the rotor.

(d) Unsteady pressure at point C on the rotor.

Figure 60.- Unsteady pressures on the rotor.

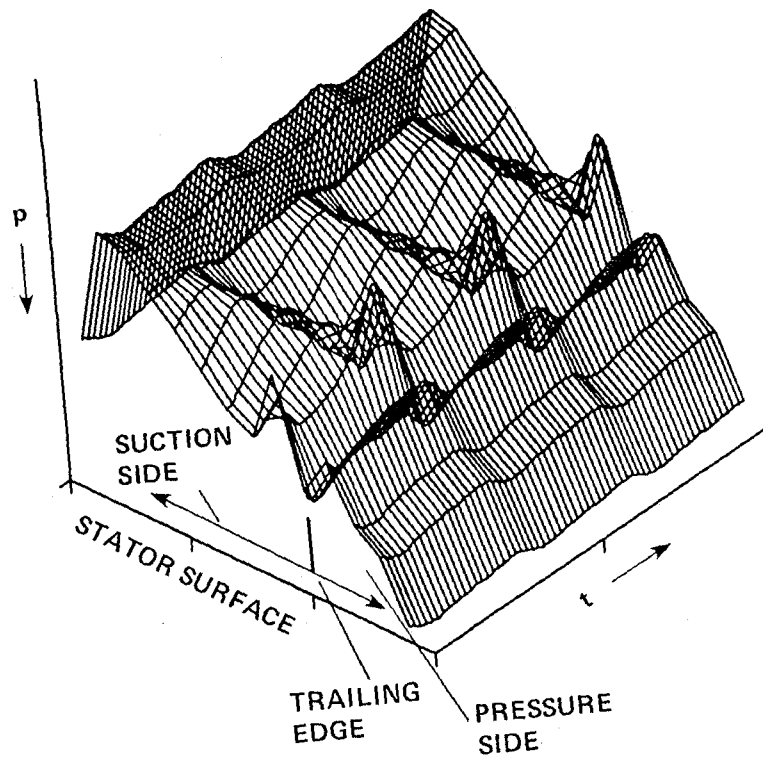


Figure 61.- Unsteady pressures on the stator surface.

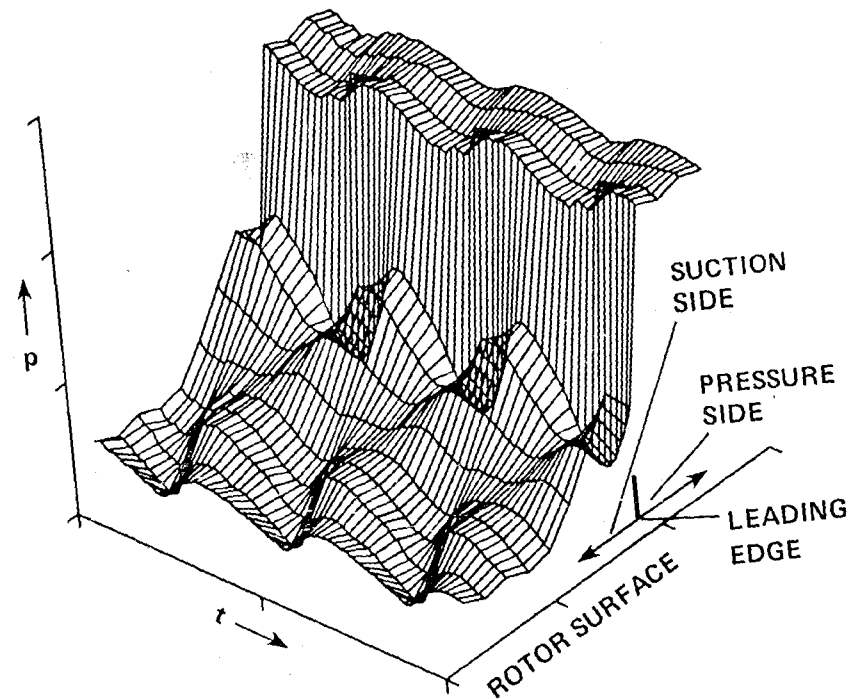


Figure 62.- Unsteady pressures on the rotor surface.

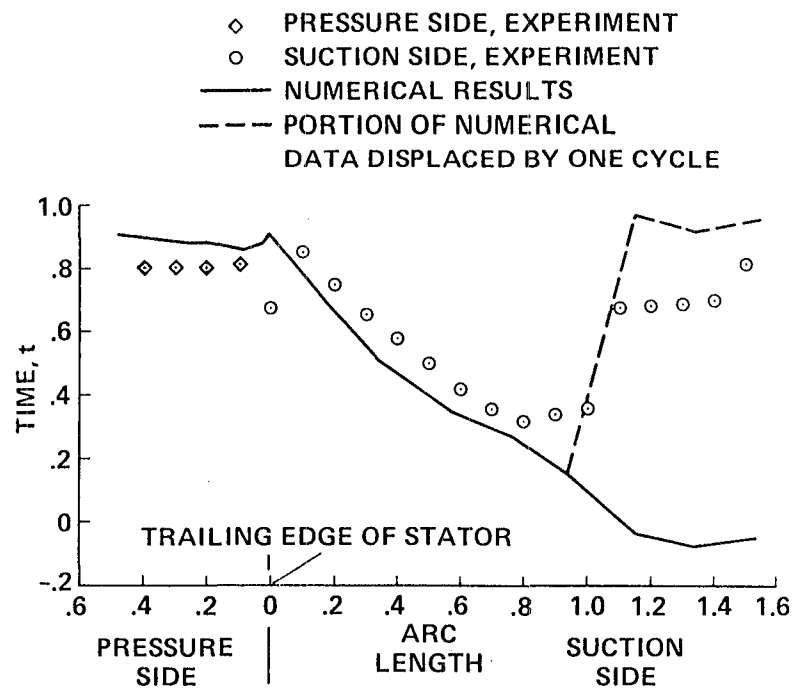


Figure 63.- Phase of the low-pressure peak seen in figure 61.

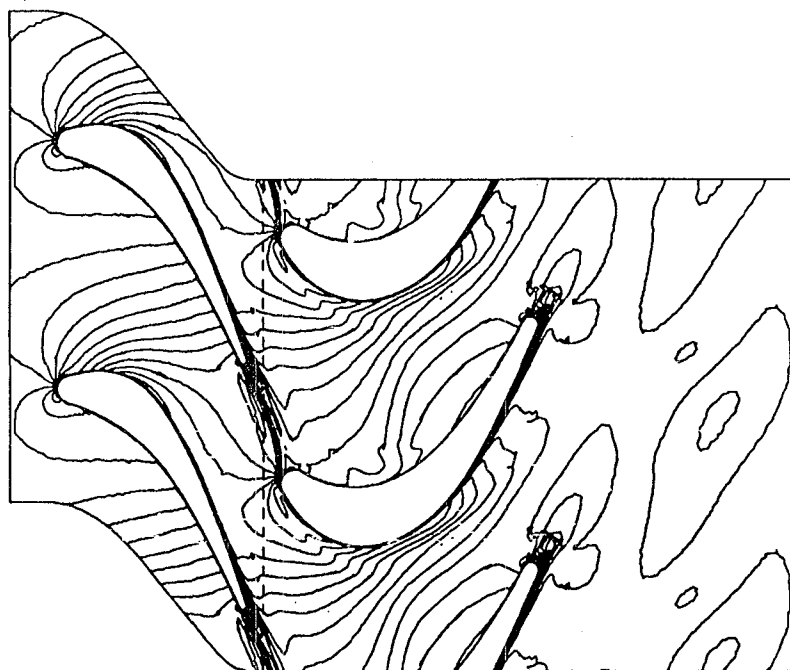


Figure 64.- Mach number contours ($t = 0.00$).

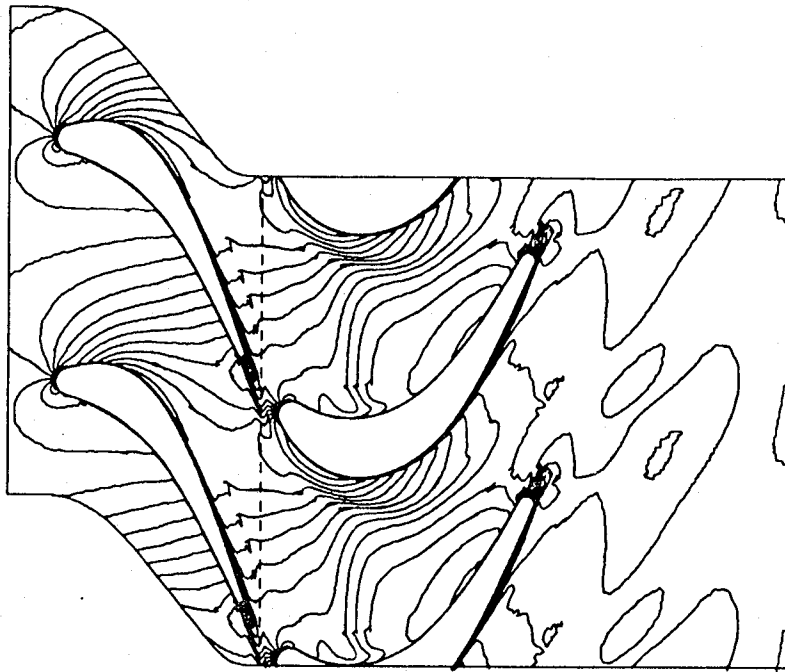


Figure 65.- Mach number contours ($t = 0.25$).

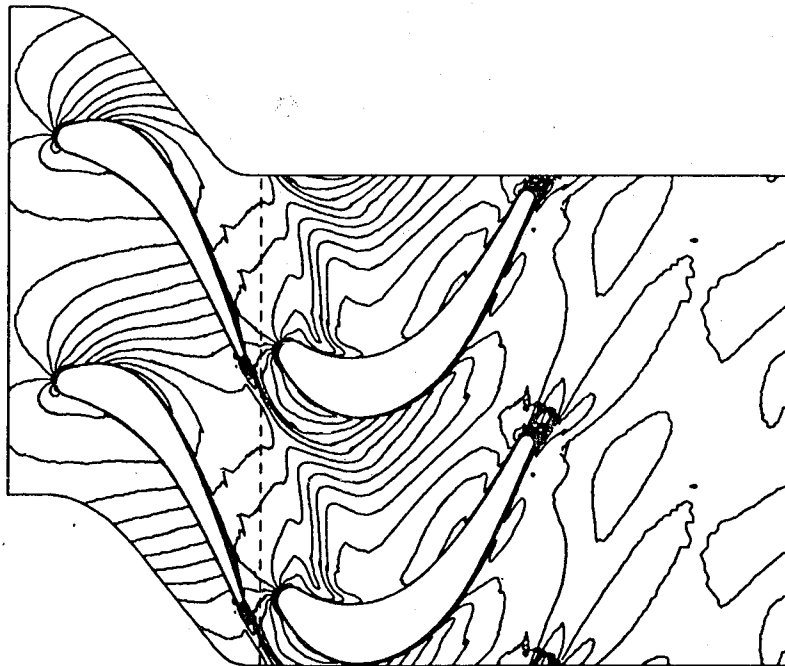


Figure 66.- Mach number contours ($t = 0.50$).

1. Report No. NASA TM 88228		2. Government Accession No.		3. Recipient's Catalog No.	
4. Title and Subtitle PATCHED-GRID CALCULATIONS WITH THE EULER AND NAVIER-STOKES EQUATIONS: THEORY AND APPLICATIONS.				5. Report Date February 1986	
				6. Performing Organization Code	
7. Author(s) M. M. Rai*				8. Performing Organization Report No. 86112	
9. Performing Organization Name and Address Ames Research Center, Moffett Field, CA, 94035 *Informatics General Corp., Palo Alto, CA, 94303				10. Work Unit No.	
				11. Contract or Grant No.	
12. Sponsoring Agency Name and Address National Aeronautics and Space Administration Washington, DC, 20545				13. Type of Report and Period Covered Technical Memorandum	
				14. Sponsoring Agency Code 505-60-01	
15. Supplementary Notes Point of contact: M. M. Rai, Ames Research Center, MS 202A-14, Moffett Field, CA 94035 (415) 694-6742 or FTS 464-6742					
16. Abstract A "patched-grid" approach is one in which the flow region of interest is divided into subregions which are then discretized independently using existing grid generators. The equations of motion are integrated in each subregion in conjunction with patch-boundary schemes which allow proper information transfer across interfaces that separate subregions. The patched-grid approach greatly simplifies the treatment of complex geometries and also the addition of grid points to selected regions of the flow. In this study a conservative patch-boundary condition that can be used with explicit, implicit factored and implicit relaxation schemes is described. Several example calculations that demonstrate the capabilities of the patched-grid scheme are also included.					
17. Key Words (Suggested by Author(s)) Euler equations Patched-grids			18. Distribution Statement Unlimited Subject category: 02		
19. Security Classif. (of this report) Uncl.		20. Security Classif. (of this page) Uncl.		21. No. of Pages 104	
				22. Price* A03	

End of Document